

Progress and Perspectives in Visible-Light-Driven Photocatalysis

Guest Editors: Monica Baia, Krisztina Gajda-Schranz, Shaohua Shen,
and Elias Stathatos





Progress and Perspectives in Visible-Light-Driven Photocatalysis

International Journal of Photoenergy

Progress and Perspectives in Visible-Light-Driven Photocatalysis

Guest Editors: Monica Baia, Krisztina Gajda-Schranz,
Shaohua Shen, and Elias Stathatos



Copyright © 2013 Hindawi Publishing Corporation. All rights reserved.

This is a special issue published in "International Journal of Photoenergy." All articles are open access articles distributed under the Creative Commons Attribution License, which permits unrestricted use, distribution, and reproduction in any medium, provided the original work is properly cited.

Editorial Board

M. Sabry Abdel-Mottaleb, Egypt
Nihal Ahmad, USA
Nicolas Alonso-Vante, France
Wayne A. Anderson, USA
Vincenzo Augugliaro, Italy
Detlef W. Bahnemann, Germany
Mohammad A. Behnajady, Iran
Ignazio Renato Bellobono, Italy
Raghu N. Bhattacharya, USA
Pramod H. Borse, India
Gion Calzaferri, Switzerland
Adriana G. Casas, Argentina
Wonyong Choi, Korea
Věra Cimrova, Czech Republic
Vikram Dalal, USA
Dionysios D. Dionysiou, USA
Mahmoud M. El-Nahass, Egypt
Ahmed Ennaoui, Germany
Chris Ferekides, USA
Beverley Glass, Australia
M. A. Gondal, Saudi Arabia
Shinya Higashimoto, Japan
Yadong Jiang, China

Chun-Sheng Jiang, USA
Shahed Khan, USA
Cooper Harold Langford, Canada
Yuexiang Li, China
Stefan Lis, Poland
Niyaz Mohammad Mahmoodi, Iran
Dionissios Mantzavinos, Greece
Ugo Mazzucato, Italy
Jacek Miller, Poland
Jarugu N. Moorthy, India
Franca Morazzoni, Italy
Fabrice Morlet-Savary, France
Ebinazar B. Namdas, Australia
Maria da Graça P. Neves, Portugal
Leonidas Palilis, Greece
Leonardo Palmisano, Italy
Ravindra K. Pandey, USA
David Lee Phillips, Hong Kong
Pierre Pichat, France
Gianluca Li Puma, UK
Xie Quan, China
Tijana Rajh, USA
Peter Robertson, UK

Avigdor Scherz, Israel
Lukas Schmidt-Mende, Germany
Panagiotis Smirniotis, USA
Zofia Stasicka, Poland
Juliusz Sworakowski, Poland
Nobuyuki Tamaoki, Japan
Gopal N. Tiwari, India
Nikolai V. Tkachenko, Finland
Veronica Vaida, USA
Roel van De Krol, Germany
Mark van Der Auweraer, Belgium
Ezequiel Wolcan, Argentina
Man Shing Wong, Hong Kong
David Worrall, UK
Fahrettin Yakuphanoglu, Turkey
Minjoong Yoon, Korea
Hongtao Yu, USA
Jimmy C. Yu, Hong Kong
Jun-Ho Yum, Switzerland
Klaas Zachariasse, Germany
Lizhi Zhang, China
Jincai Zhao, China

Contents

Progress and Perspectives in Visible-Light-Driven Photocatalysis, Monica Baia, Krisztina Gajda-Schranz, Shaohua Shen, and Elias Stathatos
Volume 2013, Article ID 314187, 3 pages

Preparation of Fe-Doped TiO₂ Nanotubes and Their Photocatalytic Activities under Visible Light, Honghui Teng, Shukun Xu, Dandan Sun, and Ying Zhang
Volume 2013, Article ID 981753, 7 pages

Facile Preparation of Phosphotungstic Acid-Impregnated Yeast Hybrid Microspheres and Their Photocatalytic Performance for Decolorization of Azo Dye, Lan Chen and Bo Bai
Volume 2013, Article ID 406158, 9 pages

Au-TiO₂ Nanocomposites and Efficient Photocatalytic Hydrogen Production under UV-Visible and Visible Light Illuminations: A Comparison of Different Crystalline Forms of TiO₂, Deepa Jose, Christopher M. Sorensen, Sadhana S. Rayalu, Khadga M. Shrestha, and Kenneth J. Klabunde
Volume 2013, Article ID 685614, 10 pages

Bulky Macroporous TiO₂ Photocatalyst with Cellular Structure via Facile Wood-Template Method, Qingfeng Sun, Yun Lu, Jinchun Tu, Dongjiang Yang, Jun Cao, and Jian Li
Volume 2013, Article ID 649540, 6 pages

Preparation of Nanostructured Cu₂SnS₃ Photocatalysts by Solvothermal Method, Qingyun Chen and Di Ma
Volume 2013, Article ID 593420, 5 pages

In Situ Measurement of Local Hydrogen Production Rate by Bubble-Evolved Recording, Xiaowei Hu, Liejin Guo, and Yechun Wang
Volume 2013, Article ID 568206, 6 pages

Facile Growth of Porous Hematite Films for Photoelectrochemical Water Splitting, Shaohua Shen, Jiangang Jiang, Penghui Guo, and Liejin Guo
Volume 2013, Article ID 174982, 8 pages

Structural and Photoelectrochemical Properties of Cu-Doped CdS Thin Films Prepared by Ultrasonic Spray Pyrolysis, Rui Xie, Jinzhan Su, Mingtao Li, and Liejin Guo
Volume 2013, Article ID 620134, 7 pages

TiO₂ and ZnO Nanoparticles in Photocatalytic and Hygienic Coatings, Veronika Jašková, Libuše Hochmannová, and Jarmila Vyřasová
Volume 2013, Article ID 795060, 6 pages

Effect of PdS on Photocatalytic Hydrogen Evolution of Nanostructured CdS under Visible Light Irradiation, Qingyun Chen, Cheng Suo, Shu Zhang, and Yunhai Wang
Volume 2013, Article ID 149586, 5 pages

Editorial

Progress and Perspectives in Visible-Light-Driven Photocatalysis

Monica Baia,¹ Krisztina Gajda-Schranz,² Shaohua Shen,³ and Elias Stathatos⁴

¹ Faculty of Physics and Interdisciplinary Research Institute on Bio-Nano-Sciences, Babes-Bolyai University, 400084 Cluj-Napoca, Romania

² Department of Inorganic and Analytical Chemistry, Environmental Chemistry Research Group, University of Szeged, Dóm tér 7, Szeged 6720, Hungary

³ International Research Center for Renewable Energy, State Key Laboratory of Multiphase Flow in Power Engineering, Xi'an Jiaotong University, Shaanxi 710049, China

⁴ Electrical Engineering Department, Technological-Educational Institute of Western Greece, 26334 Patras, Greece

Correspondence should be addressed to Monica Baia; monica.baia@phys.ubbcluj.ro

Received 23 October 2013; Accepted 23 October 2013

Copyright © 2013 Monica Baia et al. This is an open access article distributed under the Creative Commons Attribution License, which permits unrestricted use, distribution, and reproduction in any medium, provided the original work is properly cited.

The development of nanotechnology for the synthesis of nanomaterials is providing unprecedented opportunities to deal with emerging environmental problems associated with water and air contamination along with worldwide energy-related concerns. Advanced oxidation technologies (AOTs) and nanotechnologies (AONs) have been extensively investigated for the destruction of toxic and recalcitrant organic compounds and inactivation of microorganisms in water and air. Photocatalysis as a part of AOTs is an effective method to completely decompose organic pollutants in air and aqueous solutions/natural waters. However, conventional wide band gap semiconducting materials (TiO₂, ZnO, etc.) usually employed in photocatalytic processes absorb radiation below 400 nm, which is in the UV region, being only 5% of the solar light. In order to effectively utilize solar light as the source of energy, modified materials that can also absorb in the visible spectrum need to be synthesized. Recently, doping TiO₂ with different heteroatoms (metal and/or nonmetal ions) made it possible to shift the absorption towards longer wavelengths and, thus, allow TiO₂ sensitization in the visible region. Due to the visible light absorption abilities, doped TiO₂-based powders and films can also be used for improving the photocatalytic process in the visible region. Several attempts have been directed towards the development of modified TiO₂ with visible light response by dye sensitization, metal (Fe, Co, Ag), and nonmetal (N, F, C, S) doping of the catalyst to reduce TiO₂ band gap energy

requirements for photocatalytic activation. In some metal doping approaches, the resulting visible light photocatalytic activity has some drawbacks including increase in the carrier-recombination centers (electron-hole pair species generated after photoexcitation of the catalyst) and low thermal stability of the modified material. Furthermore, the sensitization of TiO₂ nanoparticles with quantum dots of CdS, CdSe, CdTe, PbS, and PbSe and their combinations could effectively lead to visible-light-activated photocatalysts. Several intrinsic visible-light-active semiconductors, mostly metal sulphides, have been fabricated by nonmetal-mediated band structure engineering. The visible-light sensitization of metal sulphides can be attributed to the S 3p states, which increase the width of the valence band itself and cause the decrease in the band gap energy. Among the available sulphides, CdS with band gap of 2.4 eV is probably the best-studied metal sulphide photocatalyst, although it is unstable and toxic. The aim of this special issue is to present some recent progress in the field of visible-light-activated photocatalysts. The issue contains ten selected papers after invitation. A brief summary of all accepted papers is provided below.

The article entitled “Preparation of Fe-doped TiO₂ nanotubes and their photocatalytic activities under visible light” reported the preparation of Fe-doped TiO₂ nanotubes (Fe-TNTs) by ultrasonic-assisted hydrothermal method. The structure and composition of the as-prepared TiO₂ nanotubes were characterized by transmission electron

microscopy (TEM), X-ray diffraction (XRD), and UV-Vis absorption spectroscopy. Their photocatalytic activities were evaluated by the degradation of methyl orange under visible light. The Fe-TNTs demonstrated good photocatalytic activities and photostability under visible light irradiation, and the optimum molar ratio of Ti : Fe was found to be 100 : 1.

In the paper entitled "*Facile preparation of phosphotungstic acid-impregnated yeast hybrid microspheres and their photocatalytic performance for decolorization of azo dye*" phosphotungstic acid (HPW)-impregnated yeast hybrid microspheres were prepared by impregnation-adsorption technique through tuning pH of the aqueous yeast suspensions. The obtained products were characterized by field emission scanning electron microscopy (FE-SEM), energy dispersive spectrometry (EDS), XRD, thermogravimetry-differential scanning calorimetry (TG-DSC), and UV-Vis spectrophotometry. FE-SEM and EDS ascertained that the HPW has been effectively introduced onto the surface of yeast, and the resulting samples retained ellipsoid shape, with the uniform size (length $4.5 \pm 0.2 \mu\text{m}$, width $3.0 \pm 0.3 \mu\text{m}$) and good monodispersity. XRD pattern indicated that the main crystal structure of as-synthesized HPW@yeast microsphere is Keggin structure. TG-DTA stated that the HPW in composites has better thermal stability than pure HPW. Fourier transform infrared spectroscopy (FT-IR) elucidated that the functional groups or chemical bonds inherited from the pristine yeast cell were critical to the assembling of the composites. UV-Vis spectra analysis showed that the obtained samples have a good response to UV light. The settling ability indicated that the hybrid microspheres possess an excellent suspension performance. It was shown that the HPW@yeast microsphere exhibited a high photocatalytic activity for the decoloration of Methylene blue and Congo red dye aqueous solutions.

The paper entitled "*Au-TiO₂ nanocomposites and efficient photocatalytic hydrogen production under UV-Vis and visible light illuminations: a comparison of different crystalline forms of TiO₂*" reported the preparation of Au-loaded TiO₂ nanocomposites by the solvated metal atom dispersion (SMAD) method. The obtained samples were characterized by diffuse reflectance UV-vis spectroscopy, powder XRD, BET surface analysis measurements, and TEM bright field imaging. The particle size of the embedded Au nanoparticles ranged from 1 to 10 nm. The nanocomposites were used for photocatalytic hydrogen production in the presence of a sacrificial electron donor like ethanol or methanol under UV-vis and visible light illumination. They showed very good photocatalytic activity toward hydrogen production under UV-vis conditions, whereas under visible light illumination, there was considerably less hydrogen produced. Au/P25 gave a hydrogen evolution rate of 1600 $\mu\text{mol/h}$ in the presence of ethanol (5 vol%) under UV-vis illumination. In the case of Au/TiO₂ nanocomposites, the presence of Au nanoparticles serves two purposes: being an electron sink, to gather electrons from the conduction band of TiO₂ and being a reactive site for water/ethanol reduction to generate hydrogen gas. Hydrogen production by water splitting in the absence of a sacrificial electron donor using Au/TiO₂ nanocomposites under UV-vis illumination was also observed.

The paper entitled "*Bulky macroporous TiO₂ photocatalyst with cellular structure via facile wood-template method*" reported the preparation of bulky macroporous TiO₂ particles with cellular structure in the presence of wood slices as template. The prepared samples were characterized by SEM, XRD, EDS, and TEM techniques. XRD pattern confirmed that the crystalline phase of the wood-templated TiO₂ is anatase phase. SEM image analysis revealed that the wood-templated TiO₂ inherited the initial cellular structures of birch lumber (*B. albosinensis* Burk), and numerous macropores were observed in the sample. Meanwhile, the wood-templated TiO₂ presented a superior photocatalytic ability to decompose Rhodamine B (RhB) under ultraviolet irradiation.

In the paper entitled "*Preparation of nanostructured Cu₂SnS₃ photocatalysts by solvothermal method*" nanostructured Cu-Sn-S powder was prepared by a relatively low-cost, simple, and green solvothermal method. Flower-like Cu₂SnS₃ nanostructures were successfully synthesized in 50 vol% ethanol water solution at 200°C for 7.5 h. The structure and photophysical properties of the as-obtained samples were characterized by SEM, TEM, XRD, and UV-Vis diffusion reflectance spectroscopy. Results showed that the cubic and tetragonal Cu₂SnS₃ was obtained by varying the ethanol contents. The band-gap energy of tetragonal Cu₂SnS₃ nanocrystals is near the optimum for photovoltaic solar conversion in a single band-gap device.

In the paper entitled "*In situ measurement of local hydrogen production rate by bubble-evolved recording*" optical microscopy of superfield depth was used for recording the hydrogen bubble growth on Cd_{0.5}Zn_{0.5}S photocatalyst in reaction liquid and illuminated with purple light. By analyzing the change of hydrogen bubble size as a function of time, it was revealed that hydrogen bubble growth experienced two periods. The tendency of hydrogen bubble growth was similar to that of the gas bubble in boiling, while the difference in bubble diameter and growth time magnitude was greater. Meanwhile, the local hydrogen production rate on photocatalyst active site was established by measuring hydrogen bubble growth variation characteristics. This method allowed confirming local actual hydrogen evolution rate quantitatively during photocatalytic water splitting.

In the paper entitled "*Facile growth of porous hematite films for photoelectrochemical water splitting*" a simple fabrication method of porous hematite films with tunable thickness in an aqueous solution containing FeCl₃ as the single precursor was introduced. It was demonstrated that the optimized thickness was necessary for high performance photoelectrochemical water splitting, by balancing photon absorption and charge carrier transport. The highest photocurrent of ca. 0.15 mA cm⁻² at 1.0 V versus Ag/AgCl was achieved on the 300 nm thick porous hematite film as photoanode, with IPCE at 370 nm and 0.65 V versus Ag/AgCl to be 9.0%. This simple method allowed the facile fabrication of hematite films with porous nanostructure for enabling high photon harvesting efficiency and maximized interfacial charge transfer. These porous hematite films could be easily modified by metal

doping for further enhanced photoelectrochemical activity for water splitting.

In the paper entitled “*Structural and photoelectrochemical properties of Cu-doped CdS thin films prepared by ultrasonic spray pyrolysis*” Cu-doped CdS thin films of variable doping levels were deposited on indium tin oxide-coated glass substrate by simple and cost-effective ultrasonic spray pyrolysis. The influences of doping concentration and annealing treatment on the structure and photoelectrochemical properties of the films were investigated. The deposited films were characterized by XRD, SEM, and UV-Vis spectra, and were further investigated by electrochemical and photoelectrochemical measurements with regards to splitting water for solar energy conversion. The results showed that the Cu impurity can cause a structural change and red shift of the absorption edge. It was found that the photocurrent can be improved by the Cu-doping process for the unannealed films under the weak illumination. The unannealed 5 at.% Cu-doped sample obtained the maximum IPCE, which achieved about 45% at 0.3 V versus SCE potential under 420 nm wavelength photoirradiation. In addition, the p-type CdS was formed with a doping of 4 at.% ~10 at.% Cu after 450°C 2 h annealed in vacuum.

In the paper entitled “*TiO₂ and ZnO nanoparticles in photocatalytic and hygienic coatings*” antimicrobial paints based on the aqueous acrylic dispersion and various nanoparticles of zinc oxide and titanium dioxide were obtained. Antimicrobial ability and photoactivity were assumed in these paints. It was found that the coating containing the mixture of the first type of TiO₂ and nano-ZnO showed the best photocatalytic effect despite the fact that the first type of TiO₂ was not better in the photocatalytic test than the other types of TiO₂. The agar dilution method was used to test antimicrobial ability. *Escherichia coli*, *Pseudomonas aeruginosa*, and *Staphylococcus aureus* were chosen as test bacteria and *Penicillium chrysogenum* and *Aspergillus niger* as test molds. The antimicrobial effect of coatings with the mixture of the first type of TiO₂ and nano-ZnO was the best of all the tested samples.

The paper entitled “*Effect of PdS on photocatalytic hydrogen evolution of nanostructured CdS under visible light irradiation*” reported the preparation of nanostructured PdS/CdS by an *in situ* coprecipitation and hydrothermal method, respectively, in order to investigate the effect of PdS as a cocatalyst for photocatalytic hydrogen evolution. The as-prepared photocatalysts were characterized by TEM, XRD, UV-vis absorption spectroscopy, and photoluminescence. With PdS highly dispersed in CdS nanostructures, the photoactivity was evaluated by hydrogen evolution from aqueous solution containing Na₂S/Na₂SO₃ as sacrificial reagents under visible light irradiation. When the concentration of PdS was 1% by weight, PdS/CdS, prepared by the *in situ* coprecipitation, showed the highest photocatalytic activity, while that prepared by hydrothermal method showed the highest stability for hydrogen evolution. The effect of highly dispersed PdS on the photoactivity was discussed.

Acknowledgments

We would like to express our thanks to all authors who made this special issue possible. We hope the readers of this issue will find interesting information on the materials and visible light activated photocatalytic processes.

Monica Baia
Krisztina Gajda-Schranz
Shaohua Shen
Elias Stathatos

Methodology Report

Preparation of Fe-Doped TiO₂ Nanotubes and Their Photocatalytic Activities under Visible Light

Honghui Teng,^{1,2} Shukun Xu,¹ Dandan Sun,² and Ying Zhang²

¹ Department of Chemistry, Northeastern University, Shenyang 110004, China

² College of Environmental Science and Engineering, Jilin Normal University, Siping 136000, China

Correspondence should be addressed to Honghui Teng; tenghonghui@jlnu.edu.cn and Shukun Xu; xushukun46@126.com

Received 18 January 2013; Revised 8 April 2013; Accepted 8 May 2013

Academic Editor: Monica Baia

Copyright © 2013 Honghui Teng et al. This is an open access article distributed under the Creative Commons Attribution License, which permits unrestricted use, distribution, and reproduction in any medium, provided the original work is properly cited.

Fe-doped TiO₂ nanotubes (Fe-TNTs) have been prepared by ultrasonic-assisted hydrothermal method. The structure and composition of the as-prepared TiO₂ nanotubes were characterized by transmission electron microscopy, X-ray diffraction, and UV-Visible absorption spectroscopy. Their photocatalytic activities were evaluated by the degradation of MO under visible light. The UV-visible absorption spectra of the Fe-TNT showed a red shift and an enhancement of the absorption in the visible region compared to the pure TNT. The Fe-TNTs were provided with good photocatalytic activities and photostability and under visible light irradiation, and the optimum molar ratio of Ti : Fe was found to be 100 : 1 in our experiments.

1. Introduction

Photocatalysis is a “green” technology with promising applications in a wide assortment of chemical and environmental technologies [1]. Since the photocatalytic splitting of water on TiO₂ electrodes was discovered by Fujishima and Honda in 1972, TiO₂ photocatalysis has been extensively investigated in the field of environmental protection owing to its potential in environmental problems such as air purification and wastewater treatment [2–6]. However, the TiO₂ photocatalysts were in powder form in most studies, which shows some disadvantages for practical use including the difficulties in separation or recovery from the treated water. Recently, titania nanotubes (TNTs) as photocatalyst have gained importance in wastewater treatment, they have several advantages, such as no waste solids disposal problems and utilization of sunlight or near UV light for irradiation [7], and can overcome the separation problem [8].

For improvement of photocatalytic activity of TNT and efficient utilization of solar energy, a series of metal and nonmetal doping, such as iron, nickel, platinum, chromium, carbon, nitrogen, and iodine, have been investigated for modifications of TNT [9–16]. Among of them, Fe is the most

frequently investigated, and many studies have shown that the Fe-doped TNT exhibits effective photocatalytic activity for degradation of organic pollutant under visible light irradiation [8, 17–19]. Moreover, among all reported available candidates, Fe is one of the most suitable for industrial applications considering its low cost and easy preparation [20]. Doping TiO₂ with Fe³⁺ is an effective approach to reduce electron-hole recombination rate and increase photocatalytic efficiency in terms of its semifull electronic configuration and ion radius close to Ti⁴⁺ [20]. Xu and Yu [21] reported Fe-modified TNTs by integrating a dip-coating procedure and annealing posttreatment. The resulting Fe₂O₃-TNTs displayed a higher photoelectrocatalytic activity under visible light irradiation than pure TNTs. Fe₂O₃/TiO₂ nanorod-nanotube arrays prepared by pulsed electrodeposition technique exhibited strong absorption in the range of 200–600 nm [21]. Wu and coworkers [20] prepared Fe incorporated TiO₂NTs by an ultrasound-assisted impregnating-calcination method. Fe-incorporation induced the redshift of the absorption edge of TiO₂NTs into the visible light range. An and coworkers [21–23] reported iron-coated TiO₂ nanotubes by treating hydrogen titanate nanotubes with Fe(OH)₃ sol. Iron-coated nanotubes exhibit better photocatalytic performance under visible light irradiation than their precursors. Tu and

coworkers [8] produced Fe-doped TiO₂ nanotube arrays by the template-based LPD method with the commercial AAO membrane as the template. The resulting Fe-TNTs exhibited good photocatalytic activities under visible light irradiation.

In this paper, we report Fe-doped titanate nanotubes by ultrasonic-assisted hydrothermal method with Fe(NO₃)₃ aqueous solution. It is a very simple process and does not require any special treatment that other methods need. The resulting Fe-doped TNT showed good photocatalytic activities under visible light irradiation. This work would be valuable for the practical application of TiO₂ in the field of photocatalysis under visible light irradiation.

2. Experimental Sections

2.1. Preparation of Samples. Fe-doped TNT was fabricated by using the ultrasonic-assisted hydrothermal method [24]. The anatase TiO₂ powders (40–60 nm) were employed as the Ti source, and Fe(NO₃)₃ aqueous solutions were used as the Fe source. In a typical procedure, 1.0 g TiO₂ powders suspensions were dispersed in 50 mL 10 M NaOH aqueous solution, 1 mL different concentrations of Fe(NO₃)₃ aqueous solutions (0.013, 0.063, 0.125, 0.375, and 0.625 mol/L) were separately dropped into the above alkaline solution under moderate stirring, and then 9.8 mol/L of alkaline solutions were sonicated for 12 h at temperature of 343 K to form a homogeneous solution; five different molar ratios were Ti : Fe = 100 : 5, 100 : 3, 100 : 1, 100 : 0.5, and 100 : 0.1 to produce five Fe-TNT samples, namely, Fe-TNT-5, Fe-TNT-3, Fe-TNT-1, Fe-TNT-0.5, and Fe-TNT-0.1. The resulting mixture was transferred into a stainless steel autoclave with a teflon liner, which was then sealed and maintained at 180°C for 12 h. TiO₂ suspension solution has been transformed into colloidal state by sonication, which is the precondition of synthesis of ultralong nanotube and experiment showed that it cannot form colloidal state in less than 12 h. After the hydrothermal treatment, the slurry was discharged into plastic beaker, diluted with 1 L of distilled water, and then filtrated by Buchner funnel under vacuum. The filter cake was washed with distilled water repeatedly until the pH value of the washing solution is less than 7 and then dried through vacuum freeze for 12 h. After the prepared materials were calcined at 773 K for 2 h, Fe-doped TNTs were obtained. All the chemicals were of analytical grade and used without further purification as received from Sinopharm Chemical Reagent Co., Ltd.

2.2. Samples Characterization. The morphologies of as-prepared samples were analyzed by transmission electron microscopy (TEM) (JEOL JEM-100CX II, accelerating voltage 100 kV). About 0.5 g sample was pressed in quartz glass groove, and the X-ray diffraction (XRD) patterns of the samples were measured at room temperature using Rigaku D/MAX 2500 X-ray diffractometer (CuKαλ = 0.154 nm) radiation under 40 kV and 100 mA. The UV-Vis absorbance spectra of the samples were recorded with Beijing Purkinje General TU-1810UV-vis spectrophotometer.

2.3. Measurement of Photocatalytic Activity. The photocatalytic activities of the samples were evaluated by the degradation of methylorange (MO) in a cylindrical quartz vessel in response to visible light at room temperature. A type experiment was performed as follows: in a 100 mL vessel, 50 mg of the samples was dispersed in 50 mL of 20 mg/L MO aqueous solution. Before illumination, the mixtures were magnetically stirred in the dark to ensure the establishment of adsorption/desorption equilibrium of MO on the sample surfaces. Subsequently, the mixtures were irradiated with 40W tungsten lamp which is used as visible light source. The distance between the lamp and the suspension was kept at 8 cm. At given intervals, 3 mL of the suspension was sampled and subsequently centrifuged at a rate of 8000 rpm for 15 min to remove the particles of catalyst. The concentration of MO was determined by measuring the absorbance at 575 nm using a Beijing Purkinje General TU-1810 UV-vis spectrophotometer. The degradation efficiency (η) was described by the equation $\eta = (c_0 - c)/c_0 \times 100\% = (A_0 - A)/A_0 \times 100\%$ (c_0 and c were the concentrations of MO at the beginning and after the photocatalytic reaction for certain time, while A_0 and A were the absorption intensities at the beginning and after photocatalytic reaction for certain time).

3. Results and Discussion

3.1. Morphology and Structure. Figure 1 shows the TEM images of samples. Many previous papers have reported that the TNT are broken and agglomerate after calcinations at above 673 K [7]. Figure 1(a) is the TEM image of pure TNT, which shows collapse of nanotubular structure after calcination at 773 K. Compared with pure TNT, the Fe-doped TNT samples (Figures 1(b), 1(c), 1(d), 1(e), and 1(f)) still keep their nanotubular structure, and the length of the nanotubes is up to several hundreds of nanometres. Furthermore, the thickness of the wall of nanotubes increases with the increase of the doped amount of Fe, which is caused by the Fe₂O₃ particles. Similar results have been reported by An and coworkers [23]. They regarded that the insertion of Fe₂O₃ particles into the interlayer space makes the thickness of the wall of nanotubes become larger, and these particles support the nanotubular structure and make the Fe-doped TNT own thermal stability higher.

The XRD patterns of the as-prepared titanate nanotubes are shown in Figure 2. Clearly, all the curves reveal similar diffractions, and the peak positions with 2θ at 9.59°, 25.02°, 31.17°, and 48.32° are well consistent with the values of titanate nanotubes [17], which correspond with the (020), (110), (130), and (200) crystal planes, respectively. The peak positions of the pure titanate nanotubes and the Fe-doped titanate nanotubes are almost the same. No characteristic reflections of the Fe₂O₃ phases are detected with the increase of iron-doped dosage. It means that Fe³⁺ are indeed doped into the structure of titanate nanotubes, respectively, and the doping of ions Fe³⁺ does not change the structure of nanotubes obviously. Similar results have been reported in the literature on the Fe₂O₃-TiO₂ system [25, 26]. They regarded the lack of separate iron oxide phase as the incorporation of Fe³⁺ in

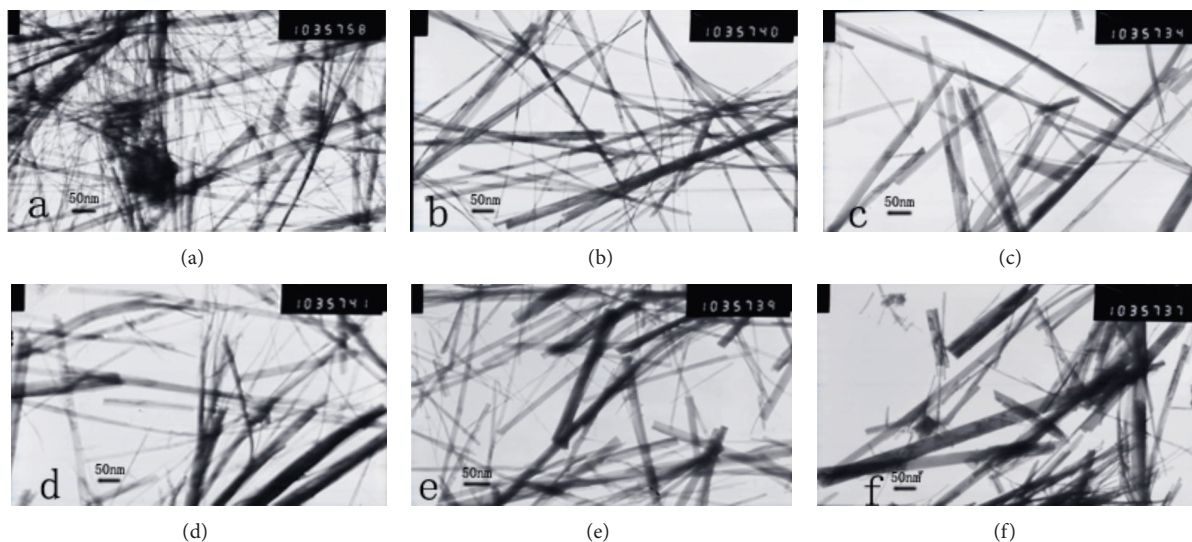


FIGURE 1: The TEM images of as-synthesized samples: (a) pure TNT, (b) Fe-TNT-0.1, (c) Fe-TNT-0.5, (d) Fe-TNT-1, (e) Fe-TNT-3, and (f) Fe-TNT-5.

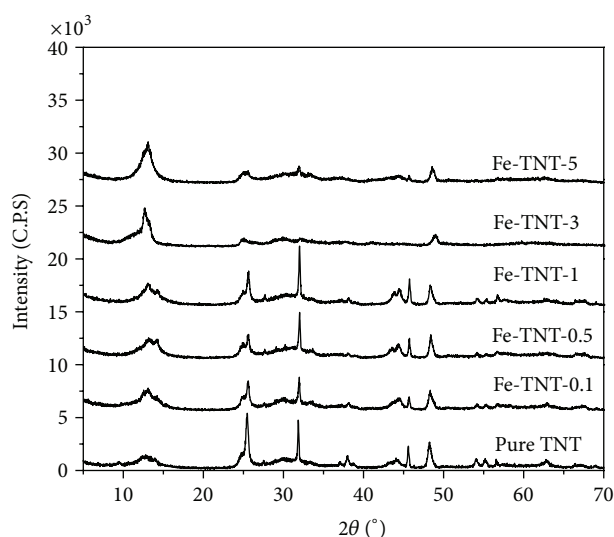


FIGURE 2: The XRD images of as-synthesized samples (pure TNT, Fe-TNT-0.1, Fe-TNT-0.5, Fe-TNT-1, Fe-TNT-3, and Fe-TNT-5).

the anatase crystal structure substituting Ti^{4+} or very fine and highly dispersed in the TiO_2 nanotubes and cannot be detected by XRD.

Figure 3 shows the UV-vis diffuse reflectance spectra of as-prepared Fe-doped TNT samples and pure TNT and Fe-doped TNTs exhibit an evident red-shift and extend their absorption to the visible light region. Increasing the doped amount of Fe, the intensities between 410 and 440 nm are raised up. The red-shift can be attributed to the formation of a new dopant energy level below the conduction band for the titanate [27]. The UV-vis data reveals that the Fe-doped TNT has an E_g value which is smaller than that of pure TNT. The narrower band gap will extend the optical response to the visible region and facilitate excitation of an electron from the

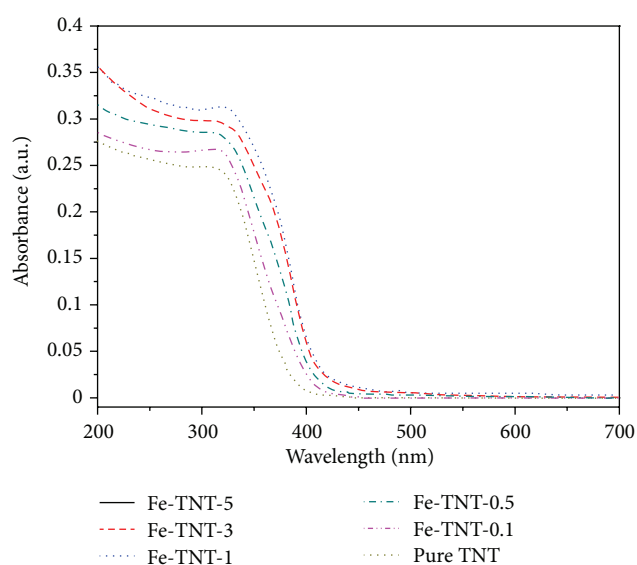


FIGURE 3: The UV-vis diffuse reflectance spectra of the as-synthesized samples (pure TNT, Fe-TNT-0.1, Fe-TNT-0.5, Fe-TNT-1, Fe-TNT-3, and Fe-TNT-5).

valence band to the conduction band, which is beneficial for the photocatalytic activity.

3.2. Photocatalytic Activity. In order to evaluate accuracy of the photocatalytic activity of the Fe-doped TNTs and to avoid affection of adsorption, adsorption/desorption equilibrium of MO on the sample surfaces was studied, and the results were shown in Figure 4. After being magnetically stirred for 10 min in the dark, the adsorption/desorption equilibrium was achieved regardless of pure TNT and Fe-doped TNTs (Figure 4(a)), or different initial pH value (2.1–7.5) of MO solution (Figure 4(b)). So, the mixtures were magnetically

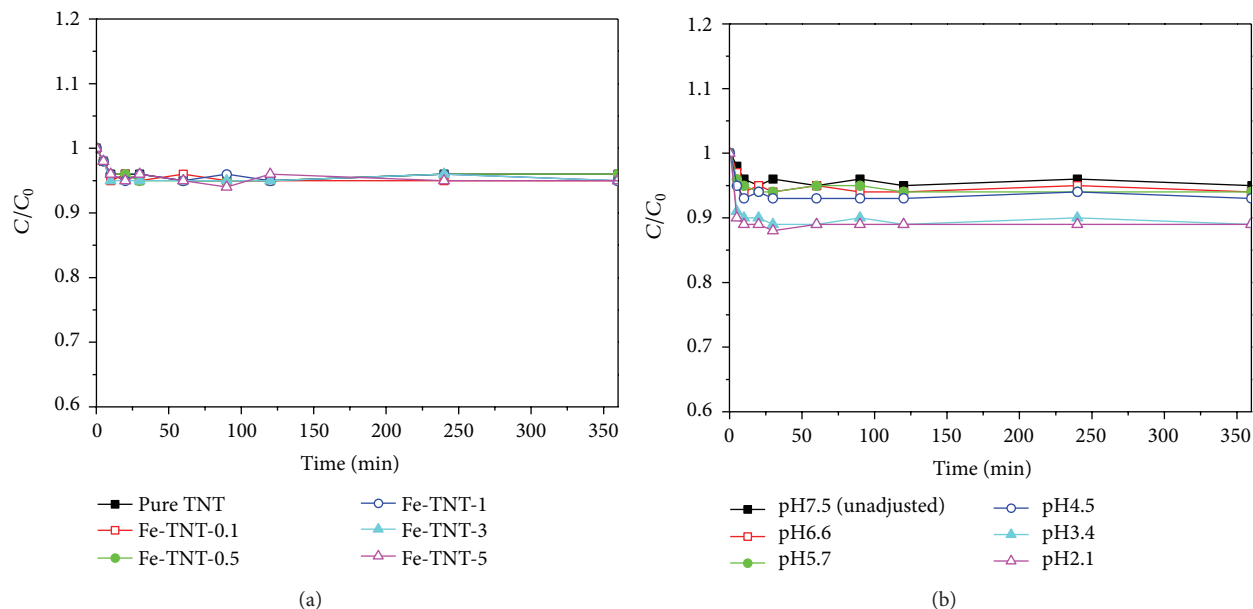


FIGURE 4: Adsorption/desorption equilibrium of MO on the sample surfaces ((a), different catalysts; (b), different pH) at different magnetically stirred time in the dark.

stirred for 10 min in the dark before illumination at the following experiments.

Figure 5 shows the photodegradation curves of methyl orange for Fe-doped TNTs as a function of Fe doping concentration. About 14, 28, 32, 45, 51, and 59% of the methyl orange is degraded after 1 h irradiation in the presence of pure TNT, Fe-TNT-5, Fe-TNT-3, Fe-TNT-0.1, Fe-TNT-0.5, and Fe-TNT-1, respectively. The activities of Fe-doped TNTs increase firstly with the molar ratios of Ti:Fe from 100:0 to 100:1 and then decrease when the molar ratios of Ti:Fe are further increased to 100:5. As the molar ratios of Ti:Fe are 100:1 (Fe-TNT-1), they arrive at the largest k value. All the Fe-doped samples display higher photocatalytic activity compared to the undoped sample, and the optimum molar ratios of Ti:Fe are found to be 100:1. The results reveal that the photocatalytic performance of TNT can be improved by the doping of iron ions. This may be due to the fact that a small amount of Fe^{3+} ions can act as a photo-generated hole and a photo-generated electron trap and inhibit the hole-electron recombination [22, 23]. However, when the dopant amount of Fe is too high, the photocatalytic activity decreases, despite the fact that there is still an increase in the absorbance of the visible light. This may be ascribed to three factors. One is the decreased crystallinity [8], one is the increased Fe^{3+} as a recombination center [17, 22], and the other is the decreasing separation distance of the charge carrier with the increase of Fe^{3+} content [22, 23].

It is well known that photocatalytic performance is related to the pH value of the solution [10, 28–30]. In order to obtain the optimal pH value of solution for photodegradation, we test the photocatalytic activities of Fe-TNT-1 and pure TNT in solutions of different pH values (pH = 2.1, 3.4, 4.5, 5.7, 6.6, and 7.5). The concentrations of the photocatalyst were kept at 1 g/L. All of the curves are shown in Figure 6. The

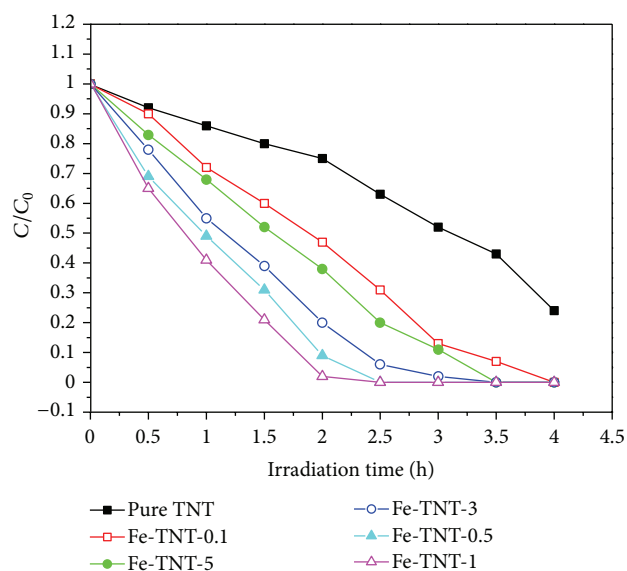


FIGURE 5: The photocatalytic activity of as-synthesized samples with different molar ratios of Ti:Fe under visible light irradiation.

overall activity and reaction rate constant decrease with the increase of pH. After irradiation for 0.5 h, about 73% of MO is degraded by Fe-TNT-1 when pH value was 2.1, while about 35% of MO when pH value was 7.5 in Figure 6(a). Evidently, the photodegradation was better in the acidic solution. Pure TNT revealed the similar variation trend in Figure 6(b), and others also reported similar results [31–35]. They believed that the role of pH was to tune the surface charge and band edge position of catalyst or change other physicochemical properties of the system [23, 36]. Since MO has an anionic configuration, the adsorption of MO on the Fe-doped TNT

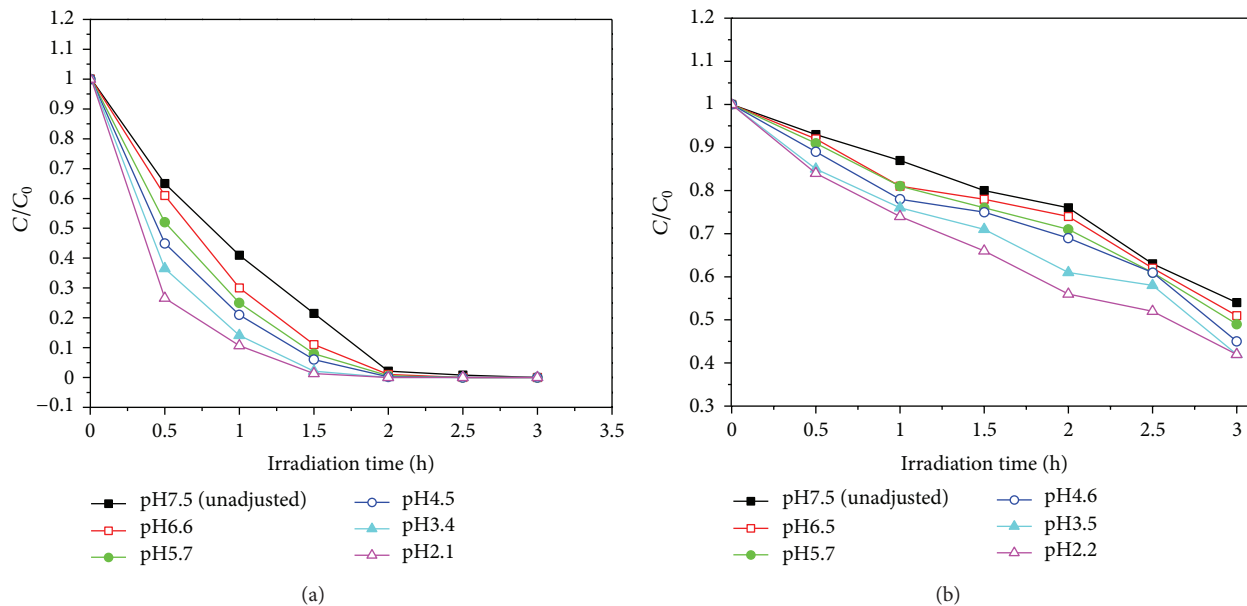


FIGURE 6: The photocatalytic activity of Fe-TNT-1 (a) and pure TNT (b) with different pH under visible light irradiation.

surface is favored in acidic solution. On the other hand, in the catalytic process, H^+ can enhance the surface acidity of Fe-doped TNT and promote MO molecules to interact with Fe-doped TNT. The optimum pH of solution is about 2.1 in this test.

The investigation of Fe-TNT-1 concentrations on the degradation of MO was conducted, which is shown in Figure 7. The initial pH values of MO solution are kept at 2.1. The degradation efficiency of MO increased with the increase of the concentration of Fe-TNT-1. However, the degradation efficiency changed a little when the concentration of Fe-doped TNT was more than 1.0 g/L. This can be explained on the basis that optimum photocatalyst loading is dependent on initial solute concentration. If the concentration of photocatalyst was increased, the total active surface would increase correspondingly, and as a result, the enhanced photocatalytic performance was obtained. However, the increased concentration of photocatalyst would have no effect on promoting the degradation efficiency after a maximum photocatalyst concentration was imposed. This may be ascribed to the increased aggregation of photocatalyst at high concentration [30, 36].

3.3. Photocatalyst Stability. Titanium dioxide has the features of resistance to photocorrosion, which is one of the reasons of titanium dioxide as photocatalyst. If that photocorrosion of Fe-doped TNT happens, is probably the depositional Fe corrosion by dissolutions of Fe^{2+} and Fe^{3+} in solution. Therefore, we researched the dissolutions of Fe with MO degradation with atomic absorption spectrometry. After 72 h of continuous illumination experiments, not checking out the iron ions in the solution, it is shown that Fe-doped TNT has the features of resistance to photocorrosion. In order to further investigate stability of Fe-doped TNT, separation and

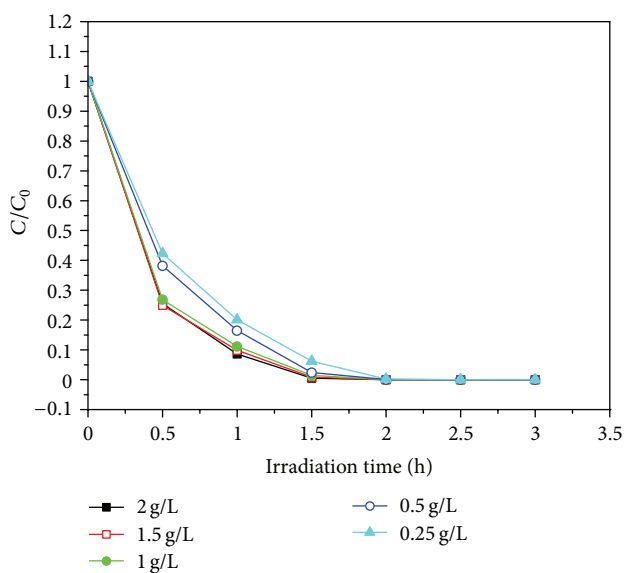


FIGURE 7: The photocatalytic activity of Fe-TNT-1 with different dosages under visible light irradiation.

recycling of Fe-doped TNT have been repeated for dealing with MO solution. The results were shown in Figure 8. A catalytic effect is basically unchanged after being used for 20 times repeatedly. The catalyst showed stable performance.

4. Conclusions

Fe-doped titanate nanotubes are prepared by the sonication-hydrothermal treatment. The investigation shows that the incorporation of Fe into the TiO_2 lattice accelerates decreases the crystallinity. The length of nanotubes is more than

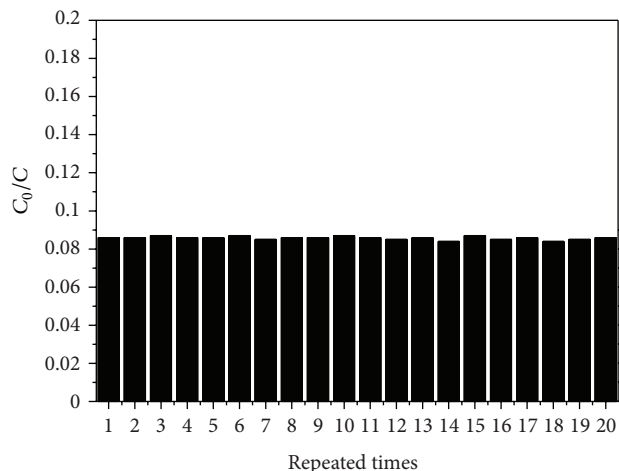


FIGURE 8: The reusability of the catalyst (20 mg/L of MO aqueous solution, initial pH = 2.1, 1.0 g/L of Fe-TNT-1, illumination 1 hour).

hundreds of nanometers. Most of the nanotubes keep their tubular texture after the calcination process. Increasing the amount of Fe also results in a decrease in the energy band gap and an enhanced absorption in the visible region. Doping an appropriate amount of Fe, the TiO₂ nanotube shows improved photocatalytic activity under visible light. The prepared Fe-doped TNT may be promising for practical application in the field of visible light photocatalysis. The catalyst has also the advantages of easy recovery, can maintain a higher activity after a plurality of repeated uses, and has higher industrial application value.

Acknowledgments

The authors greatly acknowledge the financial support obtained from the National Natural Science Foundation of China (no. 21077041) and the Science Foundation of Jilin Province of China (no. 201205076).

References

- [1] J. C. Colmenares, R. Luque, J. M. Campelo, F. Colmenares, Z. Karpinski, and A. A. Romero, "Nanostructured photocatalysts and their applications in the photocatalytic transformation of lignocellulosic biomass: an overview," *Materials*, vol. 2, no. 4, pp. 2228–2258, 2009.
- [2] J. M. Peralta-Hernández, J. Manríquez, Y. Meas-Vong et al., "Photocatalytic properties of nano-structured TiO₂-carbon films obtained by means of electrophoretic deposition," *Journal of Hazardous Materials*, vol. 147, no. 1-2, pp. 588–593, 2007.
- [3] D. M. Metzler, M. Li, A. Erdem, and C. P. Huang, "Responses of algae to photocatalytic nano-TiO₂ particles with an emphasis on the effect of particle size," *Chemical Engineering Journal*, vol. 170, no. 2-3, pp. 538–546, 2011.
- [4] S.-Y. Lu, D. Wu, Q.-L. Wang, J. Yan, A. G. Buekens, and K.-F. Cen, "Photocatalytic decomposition on nano-TiO₂: destruction of chloroaromatic compounds," *Chemosphere*, vol. 82, no. 9, pp. 1215–1224, 2011.
- [5] M. Y. Ghaly, T. S. Jamil, I. E. El-Seesy, E. R. Souaya, and R. A. Nasr, "Treatment of highly polluted paper mill wastewater by solar photocatalytic oxidation with synthesized nano TiO₂," *Chemical Engineering Journal*, vol. 168, no. 1, pp. 446–454, 2011.
- [6] J. Gao, X. Tan, Y. Miao, and R. Xin, "Modification of rutile nano-TiO₂ powders with visible light photocatalytic activity in hydrogen or nitrogen atmosphere," *Integrated Ferroelectrics*, vol. 129, no. 1, pp. 169–175, 2011.
- [7] C. L. Wong, Y. N. Tan, and A. R. Mohamed, "A review on the formation of titania nanotube photocatalysts by hydrothermal treatment," *Journal of Environmental Management*, vol. 92, no. 7, pp. 1669–1680, 2011.
- [8] Y.-F. Tu, S.-Y. Huang, J.-P. Sang, and X.-W. Zou, "Preparation of Fe-doped TiO₂ nanotube arrays and their photocatalytic activities under visible light," *Materials Research Bulletin*, vol. 45, no. 2, pp. 224–229, 2010.
- [9] C.-C. Hu, T.-C. Hsu, and L.-H. Kao, "One-step cohydrothermal synthesis of nitrogen-doped titanium oxide nanotubes with enhanced visible light photocatalytic activity," *International Journal of Photoenergy*, vol. 2012, Article ID 391958, 9 pages, 2012.
- [10] X. Zhou, F. Peng, H. Wang, H. Yu, and J. Yang, "Preparation of B, N-codoped nanotube arrays and their enhanced visible light photoelectrochemical performances," *Electrochemistry Communications*, vol. 13, no. 2, pp. 121–124, 2011.
- [11] X. Zhang, L. Lei, J. Zhang, Q. Chen, J. Bao, and B. Fang, "A novel CdS/S-TiO₂ nanotubes photocatalyst with high visible light activity," *Separation and Purification Technology*, vol. 66, no. 2, pp. 417–421, 2009.
- [12] M. Alam Khan, M. Shaheer Akhtar, S. I. Woo, and O.-B. Yang, "Enhanced photoresponse under visible light in Pt ionized TiO₂ nanotube for the photocatalytic splitting of water," *Catalysis Communications*, vol. 10, no. 1, pp. 1–5, 2008.
- [13] G. An, W. Ma, Z. Sun et al., "Preparation of titania/carbon nanotube composites using supercritical ethanol and their photocatalytic activity for phenol degradation under visible light irradiation," *Carbon*, vol. 45, no. 9, pp. 1795–1801, 2007.
- [14] C. Feng, J. Zhang, R. Lang, Z. Jin, Z. Wu, and Z. Zhang, "Unusual photo-induced adsorption-desorption behavior of propylene on Ag/TiO₂ nanotube under visible light irradiation," *Applied Surface Science*, vol. 257, no. 6, pp. 1864–1870, 2011.
- [15] M. A. Khan and O.-B. Yang, "Photocatalytic water splitting for hydrogen production under visible light on Ir and Co ionized titania nanotube," *Catalysis Today*, vol. 146, no. 1-2, pp. 177–182, 2009.
- [16] Y.-K. Lai, J.-Y. Huang, H.-F. Zhang et al., "Nitrogen-doped TiO₂ nanotube array films with enhanced photocatalytic activity under various light sources," *Journal of Hazardous Materials*, vol. 184, no. 1–3, pp. 855–863, 2010.
- [17] L. Deng, S. Wang, D. Liu et al., "Synthesis, characterization of Fe-doped TiO₂ nanotubes with high photocatalytic activity," *Catalysis Letters*, vol. 129, no. 3-4, pp. 513–518, 2009.
- [18] Z. Zhang, M. F. Hossain, and T. Takahashi, "Self-assembled hematite (α -Fe₂O₃) nanotube arrays for photoelectrocatalytic degradation of azo dye under simulated solar light irradiation," *Applied Catalysis B*, vol. 95, no. 3-4, pp. 423–429, 2010.
- [19] L. Sun, J. Li, C. L. Wang, S. F. Li, H. B. Chen, and C. J. Lin, "An electrochemical strategy of doping Fe³⁺ into TiO₂ nanotube array films for enhancement in photocatalytic activity," *Solar Energy Materials and Solar Cells*, vol. 93, no. 10, pp. 1875–1880, 2009.

- [20] Q. Wu, J. Ouyang, K. Xie, L. Sun, M. Wang, and C. Lin, "Ultra-sound-assisted synthesis and visible-light-driven photocatalytic activity of Fe-incorporated TiO₂ nanotube array photocatalysts," *Journal of Hazardous Materials*, vol. 199-200, pp. 410–417, 2012.
- [21] Z. Xu and J. Yu, "Visible-light-induced photoelectrochemical behaviors of Fe-modified TiO₂ nanotube arrays," *Nanoscale*, vol. 3, no. 8, pp. 3138–3144, 2011.
- [22] S. K. Mohapatra, S. Banerjee, and M. Misra, "Synthesis of Fe₂O₃/TiO₂ nanorod-nanotube arrays by filling TiO₂ nanotubes with Fe," *Nanotechnology*, vol. 19, no. 31, Article ID 315601, 2008.
- [23] H. An, J. Li, J. Zhou, K. Li, B. Zhu, and W. Huang, "Iron-coated TiO₂ nanotubes and their photocatalytic performance," *Journal of Materials Chemistry*, vol. 20, no. 3, pp. 603–610, 2010.
- [24] Y. Ma, Y. Lin, X. Xiao, X. Zhou, and X. Li, "Sonication-hydrothermal combination technique for the synthesis of titanate nanotubes from commercially available precursors," *Materials Research Bulletin*, vol. 41, no. 2, pp. 237–243, 2006.
- [25] Z. Ambrus, N. Balázs, T. Alapi et al., "Synthesis, structure and photocatalytic properties of Fe(III)-doped TiO₂ prepared from TiCl₃," *Applied Catalysis B*, vol. 81, no. 1-2, pp. 27–37, 2008.
- [26] W.-C. Hung, S.-H. Fu, J.-J. Tseng, H. Chu, and T.-H. Ko, "Study on photocatalytic degradation of gaseous dichloromethane using pure and iron ion-doped TiO₂ prepared by the sol-gel method," *Chemosphere*, vol. 66, no. 11, pp. 2142–2151, 2007.
- [27] X. Liu, M. K. Devaraju, S. Yin et al., "The preparation and characterization of tabular, pearlescent Fe-doped potassium lithium titanate," *Dyes and Pigments*, vol. 84, no. 3, pp. 237–241, 2010.
- [28] W.-Y. Zhou, S.-Q. Tang, Z.-B. Wei, Y.-H. Xu, and Q.-M. Lu, "Effects of heat treatment and atmosphere on the visible light photocatalytic activity of nano-TiO₂," *Journal of Inorganic Materials*, vol. 23, no. 1, pp. 61–65, 2008.
- [29] Y. Zhao, X. Zhang, J. Zhai et al., "Enhanced photocatalytic activity of hierarchically micro-/nano-porous TiO₂ films," *Applied Catalysis B*, vol. 83, no. 1-2, pp. 24–29, 2008.
- [30] X. Zhao, L. Zhu, Y. Zhang et al., "Removing organic contaminants with bifunctional iron modified rectorite as efficient adsorbent and visible light photo-Fenton catalyst," *Journal of Hazardous Materials*, vol. 215-216, pp. 57–64, 2012.
- [31] R. Vargas and O. Núñez, "The photocatalytic oxidation of dibenzothiophene (DBT)," *Journal of Molecular Catalysis A*, vol. 294, no. 1-2, pp. 74–81, 2008.
- [32] C. Karunakaran and R. Dhanalakshmi, "Semiconductor-catalyzed degradation of phenols with sunlight," *Solar Energy Materials and Solar Cells*, vol. 92, no. 11, pp. 1315–1321, 2008.
- [33] E. Grabowska, J. W. Sobczak, M. Gazda, and A. Zaleska, "Surface properties and visible light activity of W-TiO₂ photocatalysts prepared by surface impregnation and sol-gel method," *Applied Catalysis B*, vol. 117-118, pp. 351–359, 2012.
- [34] K. L. Schulte, P. A. DeSario, and K. A. Gray, "Effect of crystal phase composition on the reductive and oxidative abilities of TiO₂ nanotubes under UV and visible light," *Applied Catalysis B*, vol. 97, no. 3-4, pp. 354–360, 2010.
- [35] N. Wang, L. Zhu, K. Deng, Y. She, Y. Yu, and H. Tang, "Visible light photocatalytic reduction of Cr(VI) on TiO₂ in situ modified with small molecular weight organic acids," *Applied Catalysis B*, vol. 95, no. 3-4, pp. 400–407, 2010.
- [36] Y. Chen, Y. Zhang, C. Liu, A. Lu, and W. Zhang, "Photodegradation of malachite green by nanostructured Bi₂WO₆ visible light-induced photocatalyst," *International Journal of Photoenergy*, vol. 2012, Article ID 510158, 6 pages, 2012.

Research Article

Facile Preparation of Phosphotungstic Acid-Impregnated Yeast Hybrid Microspheres and Their Photocatalytic Performance for Decolorization of Azo Dye

Lan Chen and Bo Bai

College of Environmental Science and Engineering, Chang'an University, Xi'an 710054, China

Correspondence should be addressed to Bo Bai; baibo@chd.edu.cn

Received 16 January 2013; Revised 9 April 2013; Accepted 9 April 2013

Academic Editor: Elias Stathatos

Copyright © 2013 L. Chen and B. Bai. This is an open access article distributed under the Creative Commons Attribution License, which permits unrestricted use, distribution, and reproduction in any medium, provided the original work is properly cited.

Phosphotungstic acid (HPW)-impregnated yeast hybrid microspheres were prepared by impregnation-adsorption technique through tuning pH of the aqueous yeast suspensions. The obtained products were characterized by field emission scanning electron microscopy (FE-SEM), energy dispersive spectrometry (EDS), X-ray diffraction (XRD), thermogravimetry-differential scanning calorimetry (TG-DSC), and ultraviolet-visible spectrophotometry (UV-Vis), respectively. FE-SEM and EDS ascertain that the HPW has been effectively introduced onto the surface of yeast, and the resulting samples retain ellipsoid shape, with the uniform size (length $4.5 \pm 0.2 \mu\text{m}$, width $3.0 \pm 0.3 \mu\text{m}$) and good monodispersion. XRD pattern indicates that the main crystal structure of as-synthesized HPW@yeast microsphere is Keggin structure. TG-DTA states that the HPW in composites has better thermal stability than pure HPW. Fourier transform infrared spectroscopy (FT-IR) elucidates that the functional groups or chemical bonds inherited from the pristine yeast cell were critical to the assembling of the composites. UV-Vis shows that the obtained samples have a good responding to UV light. The settling ability indicates that the hybrid microspheres possess an excellent suspension performance. In the test of catalytic activity, the HPW@yeast microsphere exhibits a high photocatalytic activity for the decoloration of Methylene blue and Congo red dye aqueous solutions, and there are a few activity losses after four cycles of uses.

1. Introduction

Solid heteropoly acids (HPAs), a kind of environmental-friendly catalysts, could replace liquid acids to minimize the pollution damage to the environment [1–3]. Among various HPAs structural classes, Keggin-type HPAs, especially Keggin phosphotungstic acid ($\text{H}_3\text{PW}_{12}\text{O}_{40}$, HPW), have strong acidity and high conductivity [4]. By this means, a few of previous research studies have focused on the application of HPW for the photodecomposition of various kinds of environmental problems through fully making use of its strong Brønsted acidity character, redox properties, and the quasiliquid properties [5–9]. Till now, utilizing homogeneous HPA as photocatalysts in the polluted aqueous solution is very common [10, 11]. However, from a practical point of view, it may not be possible to employ this HPW as homogeneous reaction in photoreactor because of its easy solubility in polar solvent, which inevitably leads to an expensive and time-consuming

separation and recovery of photocatalysts from solvent [12]. In addition, the low specific surface area or low thermostability of HPA particles makes it difficult to improve its catalytic activity effectively [13]. To solve these problems, a few alternative strategies have been proposed to support HPW catalysts on the surface of adsorbent substance. For instance, Gao et al. [14] obtained carbonized resin-12-phosphotungstic acid (HPW) catalyst by employing carbonized resin as support. Wen et al. [15] fabricated HPW/SiO₂ successfully by using a series of SiO₂ as supports and further demonstrated that the catalytic performance of HPW/SiO₂ in alkylation reactions remarkably depended on the properties of the silica support. Obalı and Dogu [16] described the fabrication of activated carbon-tungstophosphoric acid catalysts via utilization of activated carbon as supports and the composites catalysts have a better catalytic activity than pure HPW for the synthesis of *tert*-amyl ethyl ether (TAEE). Yang et al. [17] prepared $\text{H}_3\text{PW}_{12}\text{O}_{40}$ /MCM-48 composite photocatalyst by

loading phosphotungstic acid on the mesoporous MCM-48 and the test of catalytic activity shows that the degradation of methyl orange aqueous solution could reach 84.53%.

Recently, yeasts as biotemplates or supports to synthesize catalysts have attracted considerable attention. For example, He et al. [18] synthesized Cu₂O hollow spheres by employing yeasts as biotemplates. Weinziel et al. [19] prepared SiO₂ hollow particles using yeasts as biotemplates. Our groups [20] obtained the raspberry-like TiO₂@yeast composite photocatalysts successfully by exploiting yeasts as supports. To sum up, a serial of excellent merits have been brought along for the obtained composite catalysts [21]. Typical benefits include the following. (1) The tunable and uniform shape of supports can be easily achieved from the abundant microbial cells resources in nature. (2) Additional surface modification can be left out due to the preexistence of functional groups inherited from the hydrophilic cell wall of microbial cells. (3) The composites using yeasts as supports have integrated properties originating from their hybrid components, which represent a new style of economical and environmental-friendly catalysts [20].

Thus, in the present work, the phosphotungstic acid (HPW)-impregnated yeast (HPW@yeast) hybrid microspheres were prepared by impregnation-adsorption technique through tuning pH of the aqueous yeast suspensions firstly. Then the obtained hybrid microspheres were characterized by SEM, EDS, XRD, FT-IR, and UV-Vis, respectively. A possible mechanism for the formation of the composite microspheres was proposed. Moreover, the photocatalytic activities of HPW@yeasts microspheres were evaluated by examining the decolorization of Methylene blue and Congo red. The reusability of HPW@yeast as catalyst was estimated further.

2. Experimental

2.1. Materials. Yeast powder was purchased from Angel Yeast Co. Analytical grade phosphotungstic acid (HPW) sulphuric acid (H₂SO₄) was provided by Xi'an Chemical Agent Corp. and used without further purification. Double distilled water and absolute ethanol were used throughout the experimental procedures.

2.2. Synthesis of HPW@yeast Hybrid Microsphere. In a typical synthesis procedure, 1.000 g yeast powder was washed with distilled water and ethanol for three times, respectively. The washed yeast was dispersed in 50 mL of distilled water. The pH was adjusted to approximately 2-3 by adding dropwise sulphuric acid. The suspension was magnetically stirred for 30 min to facilitate the dispersion of the yeast particles. 300 mg HPW dissolved in 40 mL ethanol was added to the previously mentioned suspensions with constant stirring. The mixture was continuously magnetically stirred for 1.0 h at room temperature and then left for 3 h without further stirring or shaking to ensure the formation of HPW@yeast heterocoagulated particles. Then, the mixture was collected by centrifugation, followed by three cycles of

distilled water and ethanol rinsing, to get filtrate precipitation, and finally dried in drying oven at 60~80°C for 40 min. After that, the HPW@yeast composite microspheres were obtained.

2.3. Characterization of Samples. X-ray diffraction (XRD) patterns of the samples were carried out on a Regaku D/MAX-3C diffractometer operated at a voltage of 40 kV and a current of 20 mA at a 0.02° scan rate with Cu K α radiation. Field-emission scanning electromicroscope (FE-SEM) images were taken on a JEOL-6300F field-emission scanning electromicroscope with an accelerating voltage of 15 kV. Fourier-transform infrared (FT-IR) spectroscopy measurements were recorded with a Bruker TENSOR 27 FT-IR spectrometer. Thermal gravimetric analysis (TG) and differential scanning calorimetry (DSC) were performed on a HCT-2 apparatus at a heating rate of 10°C/min.

2.4. The Setting Performance. 0.050 g HPW@yeast microspheres were dispersed into 50 mL of distilled water in a vertical cylindrical burette at room temperature. At regular intervals, the falling height was determined. The sedimentation ratio (R) was measured by

$$R = \frac{a}{a+b} \times 100\%, \quad (1)$$

where a is the length of the clear fluid and b is the length of the turbid fluid, respectively.

2.5. Catalytic Activity. The photocatalytic activity of the prepared samples was evaluated by the photocatalytic decolorization of anion dye Congo Red and cationic dyes Methylene Blue (MB) at room temperature. The experimental procedure was as follows: 100 mg of the prepared powders was dispersed in 100 mL of MB aqueous solution with a concentration of 12 mg/L in a beaker (with a capacity of 150 mL), and the suspensions were magnetically stirred in the dark for 30 min, prior to irradiation with UV light. The UV-light lamp placed 7 cm above the beaker was used as a light source. The concentration of MB aqueous solution was determined by a UV-visible spectrophotometer (TU-4100). Before and after irradiation, samples (6 mL) were collected at regular intervals. Each sample was centrifuged to separate the catalyst from the liquid and the supernatant was analyzed. The samples were returned into the reactor immediately after each analysis.

In order to evaluate the reusability of the obtained microspheres in the photocatalytic processes, the measurement of the lifetime of the HPW@yeast was assessed. The experimental procedure was the same as the photocatalytic activity test aforementioned. The only difference is that the experiment was operated four times. In each experiment, the catalysts were centrifuged and recovered from the photocatalytic system without other treatments that would be as catalyst for the other photodegradation experiments.

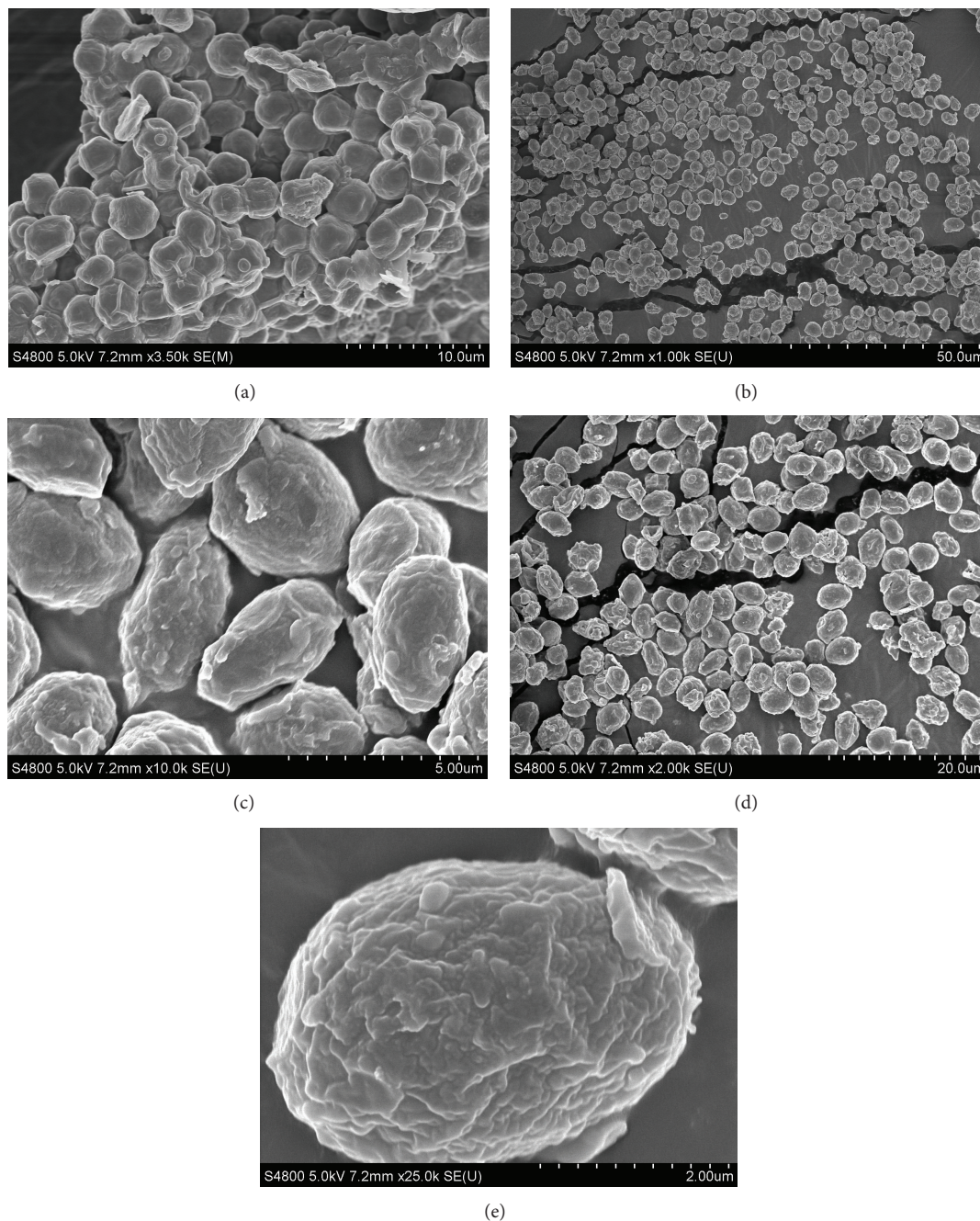


FIGURE 1: FE-SEM images of (a) yeast and (b, c, d, and e) HPW@yeast microspheres observed under different magnifications.

3. Results and Discussion

3.1. FE-SEM and EDS. The morphologies of yeast and HPW@yeast particles under the different magnifications are shown in Figure 1. Figure 1(a) displays that the morphology of the naked yeast washed with distilled water and ethanol is approximately spherical with the diameter ranging from $3.1\ \mu\text{m}$ to $4.1\ \mu\text{m}$. In Figures 1(b) and 1(c), the HPW@yeast microspheres maintain shape of the primitive yeast with relatively good monodispersity. From the high-magnification images in Figure 1(d), it is clearly seen

that each of microspheres has ordered elliptic shapes of uniform size with the length of $4.5 \pm 0.2\ \mu\text{m}$ and width of $3.0 \pm 0.2\ \mu\text{m}$. Compared with the naked yeast, the diameter of the HPW@yeast microspheres has increased only by a small amount, which arises from the attachment of HPW particles onto the surface of yeast core. The higher resolution picture of a single HPW@yeast microsphere (Figure 1(e)) indicates that the surface of species has smooth and continuous textural taints, although part of areas on the surface of the species still remains rough and unsmooth.

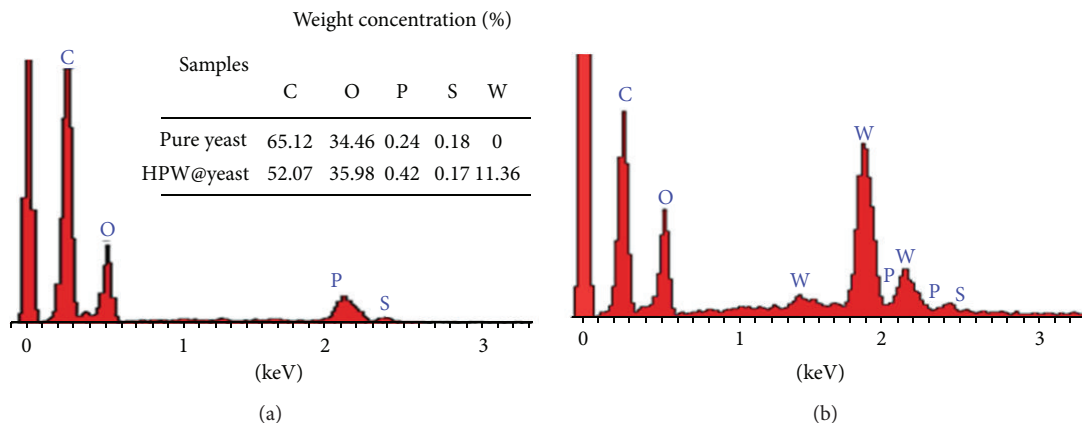


FIGURE 2: EDS spectra of (a) bare yeast and (b) HPW@yeast samples.

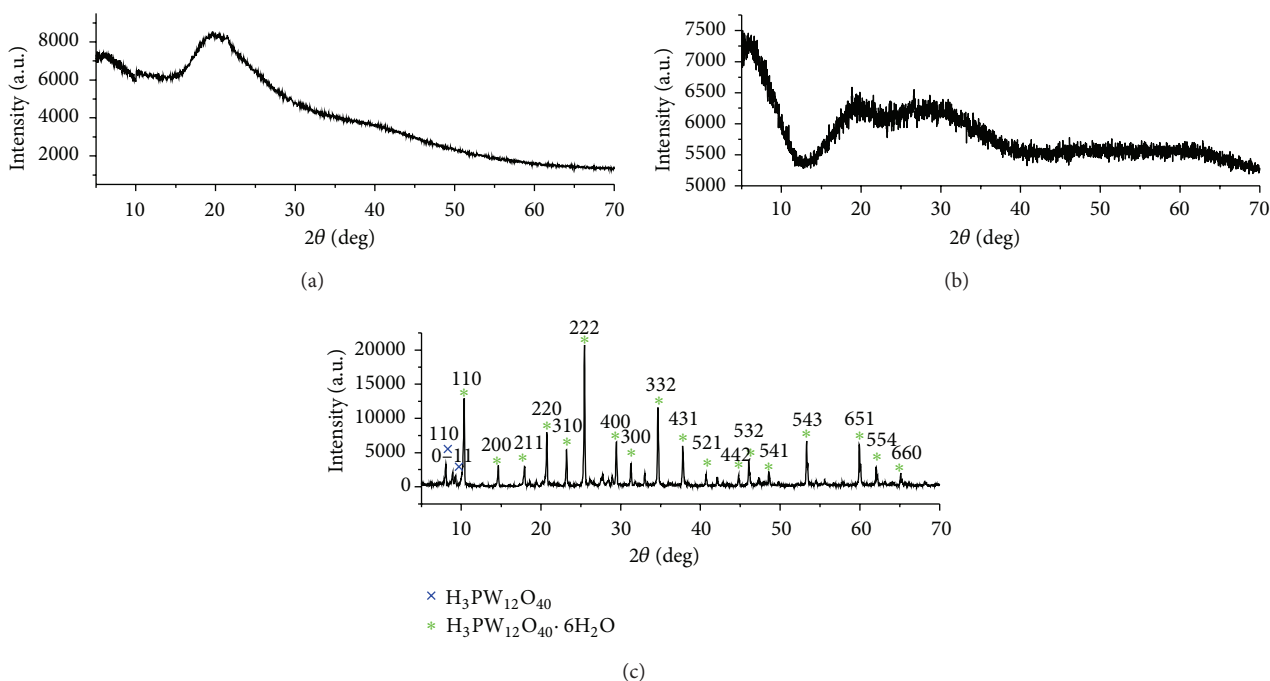


FIGURE 3: XRD patterns of (a) yeast, (b) HPW@yeast, and (c) HPW.

In order to ascertain the detailed structures of HPW@yeast composites, EDS was used to characterize the change of elemental concentration on the yeast cores and final HPW@yeast composites, respectively. The results are shown in Figure 2. For the yeast core, the peaks corresponding to C, O, P, and S are observed in Figure 2(a). After the coverage of HPW on the yeast surface, new peaks attributed to W elements (from HPW molecular) begin to appear in Figure 2(b). A decline of the C signal intensity is observed in comparison with pure yeast cores. Also, these changes have been further ascertained by quantitative evaluation of the surface atom concentration of the primitive yeast and the HPW@yeast composites. From the inset table in Figure 2, we can see that the W element on the surface of HPW@yeast microspheres is 11.36%. Compared with bare yeast core, a decrease in the atomic concentration of the C

and S elements and an increase in the P and O elements are detected due to the coverage of HPW onto surface of the yeast. The previously mentioned results provide assertive evidence that our synthesis method is effective in embedding HPW uniformly onto the yeast surface without disordering the structure of yeast cells.

3.2. XRD. XRD patterns of yeast, HPW and HPW@yeast composite, are recorded in Figure 3. The typical XRD pattern of yeast is recorded in Figure 3(a). The broad peak around $2\theta = 20^\circ$ indicates that the yeast supports can be assigned to amorphous species. In Figure 3(c) the positions of the sharp peaks below $2\theta = 10^\circ$ could be ascribed to cubic phase $\text{H}_3\text{PW}_{12}\text{O}_{40}\cdot 6\text{H}_2\text{O}$ (Hydrogen Tungsten Phosphate Hydrate) and were indexed to the reported data (JCPDS

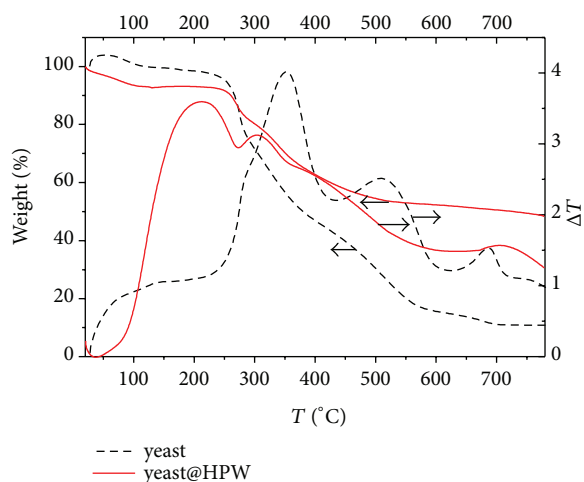


FIGURE 4: TG and DTA curves of yeast and HPW@yeast samples.

50-0304). The other remaining diffraction peaks match well with the standard diffraction data (JCPDS 50-0657) of the cubic structure $H_3PW_{12}O_{40}$ (12-tungstophosphoric acid). The XRD analysis coincides with the Keggin structure of HPW. In Figure 3(b), the HPW@yeast samples show that an obvious diffraction peak around $2\theta = 20^\circ$ arose from the amorphous structure of yeast, and some inconspicuous peaks of HPW crystal suggest that the attached HPW molecule has monolayer dispersion on the surface of yeast core.

3.3. TG-DTA. TG/DTA curves of yeast and HPW@yeast samples are recorded in Figure 4. It is noted that the weight loss of as-obtained HPW@yeast particles can be divided into three stages in the TG curve. The weight loss of ca 6% was observed below 100°C because of the release of less stable physically absorbed water in HPW and the evaporation of adsorbed moisture remaining in the yeast cells, which is accompanied by a broad endothermic peak. The rapid weight loss of about 40% at the temperature range of $250\text{--}500^\circ\text{C}$ may contribute to the desorption of crystal water in HPW and the thermal decomposition of yeast biomass, which is accompanied by two exothermic peaks below 500°C . A little reduction in weight was observed above 500°C , which could be associated with the loss of frame water in HPW and the destruction of its structure. This result was supported by the DTA curve which shows an exothermic peak at about 704°C . Furthermore, compared with the related literature of the temperature of complete decomposition [22], the attachments of HPW onto the surface of yeast have evidently enhanced the thermal stability of the HPW molecule.

3.4. FT-IR. In order to confirm the chemical structure of the HPW@yeast composites, FT-IR spectra of yeast cells, pure HPW, and HPW@yeast composites and their intermediate in the synthesis stages are recorded, respectively. The results are shown in Figure 5. The characteristic adsorption peaks of bare yeast in Figure 5(a) at 3423.61 , 2927.91 , 1641.40 , and 1076.26 cm^{-1} are ascribed to the O–H stretching vibration,

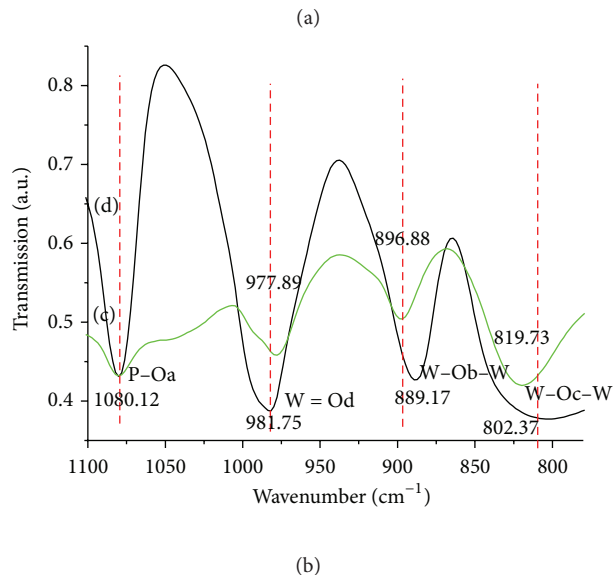
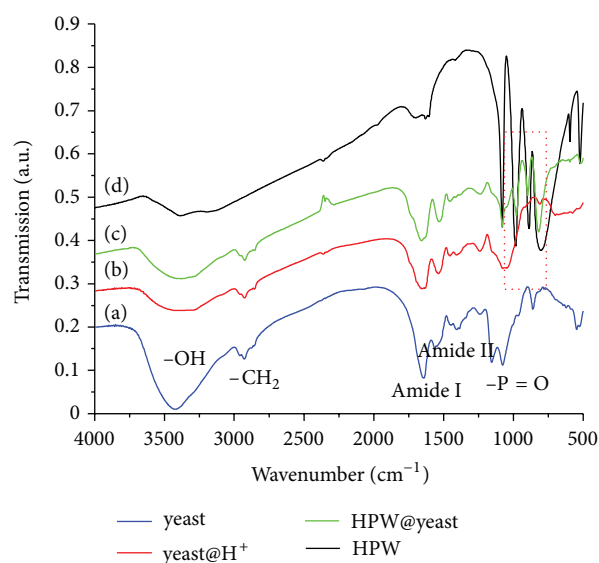
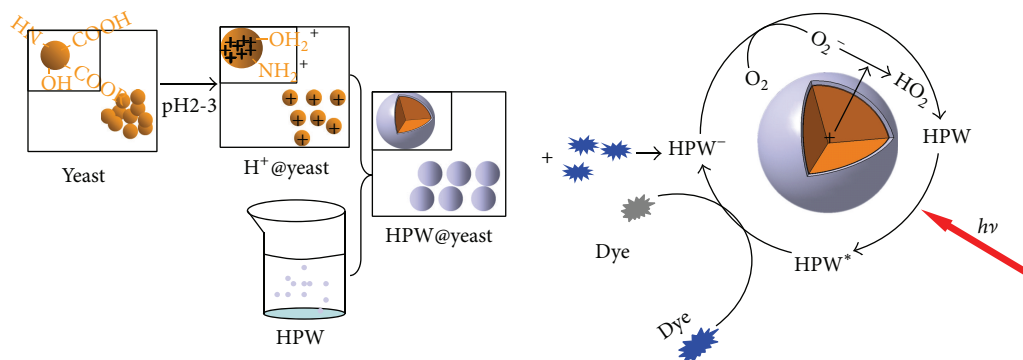


FIGURE 5: FT-IR spectra of (a) pristine yeast, (b) yeast treated by H_2SO_4 solution, (c) HPW@yeast microspheres, and (d) HPW.

CH_2 asymmetric stretching vibration, amide group, and C–O stretching vibration, separately [23–27]. In the case of pure HPW in Figure 5(d), the presences of the finger print bands below 1100 cm^{-1} are characteristic of the $PW_{12}O_{40}^{3-}$ ion with the Keggin structures. The $PW_{12}O_{40}^{3-}$ Keggin anion structure consists of a PO_4 tetrahedron surrounded by four W_3O_9 groups formed by edge-sharing octahedral. These groups are connected to each other by corner-sharing oxygen [28, 29]. This structure generates different types of oxygen atoms, which are responsible for the signature of FT-IR bands for the Keggin anions below 1100 cm^{-1} [30, 31]. The main adsorption peak at 1080.12 cm^{-1} is ascribed to P–Oa stretching and the peak at 981.75 cm^{-1} derives from W=Od stretching. The other peaks at 889.17 cm^{-1} and 802.37 cm^{-1} are due to the W–Ob–W and W–Oc–W bridges, respectively [32–34].



SCHEME 1: The formation mechanism of the HPW@yeast composite particles and their synergistic effect on the decoloration of azo dye aqueous solution.

From Figure 5(c), the simultaneous existence of typical infrared bands of Keggin unit and yeast cells implies that the HPW has been loaded on the surface of yeast cells and the Keggin structure has been preserved. Moreover, it can be found that the W=Od mode shifts from 981.75 cm^{-1} to 977.89 cm^{-1} , the W-Ob-W mode moves from 889.17 cm^{-1} to 896.18 cm^{-1} , and the absorption band of W-Oc-W shifts from 802.37 cm^{-1} to 819.73 cm^{-1} . All the characteristic bands of O-H, CH₂, amide group, and C-O in HPW@yeast shift at different degrees in comparison with pure yeast. These concurrent shifts can be attributed to the interaction between the Keggin anions in HPW and the functional groups on the surface of yeast cells, such as carboxyls, hydroxyls, and amide. The possible mechanism for the formation of HPW@yeast is illustrated in Scheme 1.

3.5. UV-Vis. UV-visible diffuse reflectance spectra (DRS) of yeast, HPW, and HPW@yeast are showed in Figure 6. In Figure 6(a), the HPW shows an adsorption peak at 267 nm, which is attributed to the charge transfer transition of W-O-W bridge bond in Keggin anions [35]. From Figure 6(b), the absorption wavelength of HPW@yeast at around 300 nm can be assigned to HPW molecules embedded on the surface of yeast. Because of the interaction between HPW and yeast, the UV absorption of two peaks is shifted from 267 nm and 300 nm to 268 nm and 305 nm, respectively. Additionally, the band edge of the HPW@yeast UV-Vis DRS is also red shifted (460 nm). The red shift mentioned-above made HPW@yeast possible for photochemical catalysis through a visible light excitation. A similar observation was made by Yuan et al. [36]. These results indicate that the primary Keggin structure has been introduced on the surface of yeast. This is also in agreement with the FT-IR analysis. Moreover, the photographs of HPW@yeast microspheres and pure yeasts are taken, respectively, in the insert images of Figure 6. We can see the color of the obtained HPW@yeast species exhibiting a slighter grey than the pure yeast, which was in accordance with its absorption spectrum.

3.6. The Settling Tests. In principle, using yeast as support in HPW@yeast products can encourage the composite microspheres exhibiting unique suspension ability. The

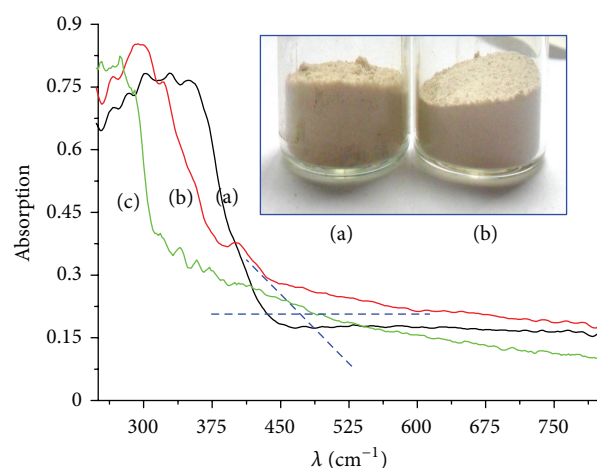


FIGURE 6: UV-Vis DRS spectra of (a) HPW, (b) HPW@yeast, and (c) pure yeast samples.

sedimentation performance of HPW@yeast microspheres in aqueous solutions is showed in Figure 7. In each experiment all the particles were dispersed in water without any additional additive. It is clearly observed that the HPW@yeast species have excellent suspension ability as that of the yeast. To be more specific, the setting ratios of pure yeast and the HPW@yeast samples only went down about 10.0% and 20.0% separately after 280 min. The scattered capacity of HPW@yeast is a bit worse than that of yeast due to the attachment of HPW onto the surface of yeast. The realistic sedimentation photographs at different time are recorded as the insert images in Figure 7. The outstanding suspension stability of HPW@yeast samples is ascribed to the apparent density of composite. As a kind of aquatic microorganisms, the wet density of yeast ($1.09 \pm 0.008\text{ g}\cdot\text{cm}^{-3}$) is almost equal to that of water. According to Stokes equation (2), lower apparent density of HPW@yeast particles will cause low sedimentation velocity [37]:

$$V_0 = \frac{2 \cdot (\rho - \sigma) \cdot g \cdot r^2}{9 \cdot \eta} \quad (2)$$

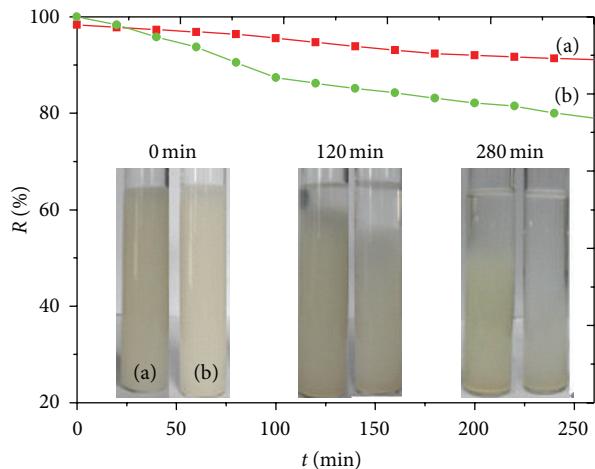
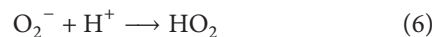


FIGURE 7: The settling curves of (a) pure yeast and (b) HPW@yeast microspheres.

In (2), V_0 is sedimentation velocity of the particles in carrier fluid; r and ρ are the radius and apparent density of the particles, respectively; σ and η are the density and viscosity of the carrier fluid, respectively; and g is the gravitational constant. In the slurry reactor, it is well known that the good suspension ability of HPW@yeast microspheres could ensure that the catalysts maintain dispersed state for a long time in aqueous solution. That is not only beneficial to the adsorption of dye molecules but also made it possible for HPW to get the utmost out of light source to realize oxidizing organic pollutants by photocatalytic degradation. In addition, owing to the micrometer size of the yeast support, the HPW@yeast composite microspheres could recover and recycle from the reaction system rapidly, accomplished by common filtration.

3.7. Catalytic Performance. In order to examine the application taints of HPW@yeast microspheres for the removal of water contaminants, the aqueous solutions of cationic dyes Methylene Blue were taken as an example. The decolorization by H^+ @yeast (the yeast was treated with H_2SO_4) and HPW@yeast microsphere was carried out, respectively. From Figure 8(a) it is shown that the MB aqueous solution is barely photolyzed by UV irradiation only. From Figure 8(c), it can be seen that only 8.9% decolorization of MB dye can be achieved by combination of yeast and UV irradiation during the 150 min reaction time. The causes of decolorization of MB dye aqueous solution can be attributed to the absorption capacity of yeast. For the HPW@yeast composite catalyst, 98.1% of the MB was decomposed after 150 min of irradiation and the gradual fading of aqueous MB solution was observed. It is obvious that the decolorization function of HPW@yeast was effective. By contrast, it can also be concluded that the Keggin structure of HPW plays a key role in the decolorization of the MB. The reaction mechanism for the decolorization of aqueous MB by the yeast@HPW is proposed as follows [38, 39]:



When a photon of UV light shines on the HPW surface, the $O(2p) \rightarrow W(5d)$ charge transfer in the Keggin structure leads to the formation of excited-state species $(HPW)^*$ (3). The excited-state species $(HPW)^*$ have higher oxidation capacity through forming electron-hole pairs. In liquid-phase reaction, the photoholes react with the water molecules, and $\bullet OH$ radicals are generated (4). $\bullet OH$ radicals are strong and unselective oxidant species in favor of totally oxidative degradation and mineralization for organic substrates. The active $\bullet OH$ radicals lead to the degradation of the MB. Alternatively, in the presence of dioxygen, the reduced catalyst (HPW^-) undergoes an easy reoxidation through the transfer of electron from reduced species to dioxygen (5). Thus the activated oxygen species HO_2 radical formed (6). However, it is documented that surface-bound and solvated $\bullet OH$ radicals are a main oxidant to attack dye [38, 39]. During the regeneration of catalysis, the positive charged surface of yeast could be an efficient electron acceptor to make HPW keep the photocatalytic cycle persisting. As we all know, there are diverse functional groups which are contained in chemical substances in the yeast cell wall, such as carboxyl, amine, hydroxyl, and phosphoryl. These functional groups could make yeast have different zeta potential, the surface charges of the particles in the same solvent at diverse acid-base intense. The isoelectric point of yeast is around pH 3.3 [40, 41]. When the pH of the solution is under 3.3, the zeta potential of yeast is above zero, displaying surface positive charge (Scheme 1). The surface positive charge catalyzes the oxidation of O_2^- into the activated oxygen species HO_2 , which accelerates the catalytic reaction rates of HPW@yeast as the result. In order to prove our conjecture of the yeast's role in catalysis, the decolorization of anionic dye Cong Red was also tested. It could be seen from Figure 6 that the degradation rate for Cong red decreases much than that of MB at the same initial mole concentration. One reason for decrease of the reaction rate would be assigned to the decrease of the concentration of the positive charge of yeast because Cong Red as an anionic dye neutralizes the positive charge on the surface of yeast. It is just another proof of our thought that the positive charge in the surface of yeast can speed up the discoloration rate of dye. The further details mechanism is currently under investigation.

One of the advantages of using heterogeneous catalysts is the possibility of their reusability [42]. The lifetime of the HPW@yeast composite catalyst has been studied by running the reaction successively with the same catalyst which was separated by simple centrifugation without other treatment. From Figure 9, it can be seen that the catalytic activity of HPW@yeast had no significant decrease after four runs. It once again demonstrated that the HPW@yeast composites could simply recycle and recover from the reaction system. The excellent reusability of the HPW@yeast catalyst indicates that product has better stability and negligible loss of the Keggin units.

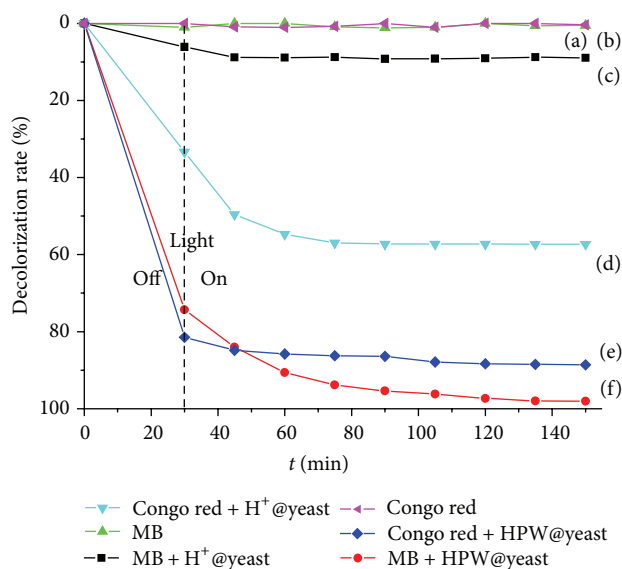


FIGURE 8: Discolorations reaction of MB and Congo red.

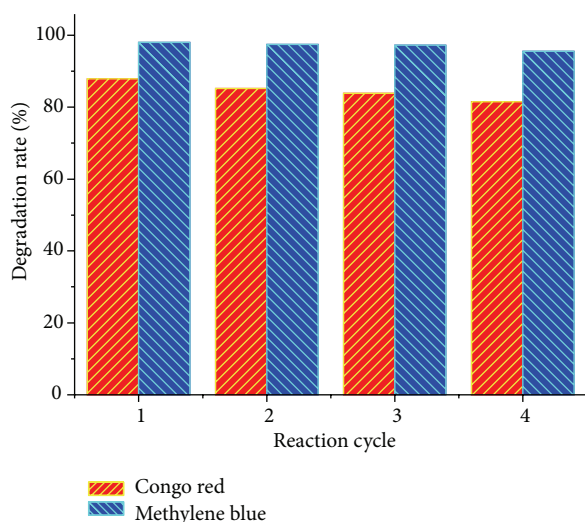


FIGURE 9: The recycle use of HPW@yeast in decoloring of MB and Congo red.

4. Conclusion

In summary, we have successfully prepared the HPW@yeast composite microspheres through impregnation-adsorption technique by tuning pH of the aqueous yeast suspensions. Physical-chemical characterization results suggest that HPW is monodisperse on the surface of yeast and the main structure belongs to Keggin unit. The composites have uniform size and good thermal stability. The obtained samples have outstanding suspension property and are easy to be separated under the conventional centrifugation. The catalytic performance indicates that the HPW@yeast microspheres have potential applications for the removal of a range of anionic and cationic dyes from wastewater. More importantly,

the composite catalysts can be used repeatedly without significant decrease of activity. It seems that the yeast support plays an important role in regeneration of catalyst. The present method can be extended to the synthesis of other hybrid microsphere of different sizes and shapes by preselecting suitable biosupport.

Acknowledgments

This work was financially supported by China Postdoctoral Science Special Foundation, National Natural Science Foundation of China (Grant no. 21176031), and Natural Science Foundation of Shaanxi Province (no. 2011JM2011).

References

- [1] N. Mizuno and M. Misono, "Heterogeneous catalysis," *Chemical Reviews*, vol. 98, no. 1, pp. 199–217, 1998.
- [2] Y. H. Guo, C. W. Hu, X. L. Wang et al., "Microporous decatungstates: synthesis and photochemical behavior," *Chemistry of Materials*, vol. 13, no. 11, pp. 4058–4064, 2001.
- [3] L. Li, Q. Y. Wu, Y. H. Guo, and C. W. Hu, "Effect of thermal treatment on surface and bulk properties of Fe/ZSM-5 zeolites prepared by different methods," *Microporous and Mesoporous Materials*, vol. 87, no. 2, pp. 93–102, 2005.
- [4] M. M. Heravi, F. Derikvand, and F. F. Bamoharram, "Highly efficient, four-component one-pot synthesis of tetrasubstituted imidazoles using Keggin-type heteropolyacids as green and reusable catalysts," *Journal of Molecular Catalysis A*, vol. 263, no. 1-2, pp. 112–114, 2007.
- [5] A. Heydaria, S. Khaksara, M. Sheykhan, and M. Tajbakhsh, " $H_3PMo_{12}O_{40}$ as a new and reusable catalyst for Mukaiyama and Mannich reactions in heterogeneous media," *Journal of Molecular Catalysis A*, vol. 287, no. 1-2, pp. 5–8, 2008.
- [6] A. Kumar, P. Singh, S. Kumar, R. Chandra, and S. Mozumdar, "A facile one-pot synthesis of thioethers using heteropoly acids," *Journal of Molecular Catalysis A*, vol. 276, no. 1-2, pp. 95–101, 2007.
- [7] X. M. Yan, J. H. Lei, D. Liu, Y. C. Wu, and W. Liu, "Synthesis and catalytic properties of mesoporous phosphotungstic acid/SiO₂ in a self-generated acidic environment by evaporation-induced self-assembly," *Materials Research Bulletin*, vol. 42, no. 11, pp. 1905–1913, 2007.
- [8] S. T. Li, C. D. Wu, Y. S. Yan, X. M. Lü, and P. W. Huo, "Photodegradation of organic contaminant by heteropoly acid," *Progress in Chemistry*, vol. 20, no. 5, pp. 690–697, 2008.
- [9] P. Kormali, D. Dimoticali, D. Tsipi, A. Hiskia, and E. Papaconstantinou, "Photolytic and photocatalytic decomposition of fenitrothion by $PW_{12}O_{40}^{3-}$ and TiO_2 : a comparative study," *Applied Catalysis B*, vol. 48, no. 3, pp. 175–183, 2004.
- [10] H. Hori, E. Hayakawa, K. Koike, H. Einaga, and T. Ibusuki, "Decomposition of nonafluoropentanoic acid by heteropoly-acid photocatalyst $H_3PW_{12}O_{40}$ in aqueous solution," *Journal of Molecular Catalysis A*, vol. 211, no. 1-2, pp. 35–41, 2004.
- [11] X. Yang, G. Yu, L. R. Kong, and L. S. Wang, "Kinetic Study on Photodegradation of Acid Red 3B Catalyzed by Heteropoly Acid," *Environmental Science*, vol. 23, no. 3, pp. 40–43, 2002.
- [12] K. Su, Z. Li, B. Cheng, L. Zhang, M. Zhang, and J. Ming, "The studies on the Friedel-Crafts acylation of toluene with acetic anhydride over HPW/TiO₂," *Fuel Processing Technology*, vol. 92, no. 10, pp. 2011–2015, 2011.

- [13] Y. J. Zeng, H. J. Yu, and L. Shi, "Structure and Catalytic Activity of Phosphotungstic Acid Supported on Y-Zeolite," *Chemical Reaction Engineering and Technology*, vol. 23, no. 6, pp. 542–547, 2007.
- [14] F. Gao, J. W. Sun, and S. H. Zhong, "Synthesis and characterization of heteropoly acid catalyst supported on carbonized resin," *Chinese Journal of Catalysis*, vol. 19, no. 2, pp. 187–190, 1999.
- [15] L. Y. Wen, S. K. Shen, and E. Z. Min, "Physicochemical and Catalytic Properties of 12-Phosphotungstic Acid Supported on Different Silica," *Chinese Journal of Catalysis*, vol. 21, no. 6, pp. 524–528, 2000.
- [16] Z. Obalı and T. Dogu, "Activated carbon-tungstophosphoric acid catalysts for the synthesis of tert-amyl ethyl ether (TAAE)," *Chemical Engineering Journal*, vol. 138, no. 1–3, pp. 548–555, 2008.
- [17] S. J. Yang, Y. J. Zhang, and H. L. Zhang, "Degradation of Methyl Orange Solution over $H_3PW_{12}O_{40}/MCM-48$," *Chemical Reaction Engineering and Technology*, vol. 27, no. 6, pp. 562–566, 2011.
- [18] W. He, X. Tian, Y. Du et al., "Biologically formed hollow cuprous oxide microspheres," *Materials Science and Engineering C*, vol. 30, no. 5, pp. 758–762, 2010.
- [19] D. Weinzierl, A. Lind, and W. Kunz, "Hollow SiO_2 microspheres produced by coating yeast cells," *Crystal Growth and Design*, vol. 9, no. 5, pp. 2318–2323, 2009.
- [20] B. Bai, N. Quici, Z. Y. Li, and G. L. Puma, "Novel one step fabrication of raspberry-like $TiO_2@yeast$ hybrid microspheres via electrostatic-interaction-driven self-assembled heterocoagulation for environmental applications," *Chemical Engineering Journal*, vol. 170, no. 2–3, pp. 451–456, 2001.
- [21] B. Bai, W. S. Guan, Z. Y. Li, and G. L. Puma, "Bio-template route for facile fabrication of $Cd(OH)_2@yeast$ hybrid microspheres and their subsequent conversion to mesoporous CdO hollow microspheres," *Materials Research Bulletin*, vol. 46, no. 1, pp. 26–31, 2011.
- [22] B. S. Li, Z. X. Liu, C. Y. Han, W. Ma, and S. J. Zhao, "In situ synthesis, characterization, and catalytic performance of tungstophosphoric acid encapsulated into the framework of mesoporous silica pillared clay," *Journal of Colloid and Interface Science*, vol. 377, no. 1, pp. 334–341, 2012.
- [23] S. J. Joris and C. H. Amberg, "Nature of deficiency in non-stoichiometric hydroxyapatites. II. Spectroscopic studies of calcium and strontium hydroxyapatites," *The Journal of Physical Chemistry*, vol. 75, no. 20, pp. 3172–3178, 1971.
- [24] M. Beekes, P. Lasch, and D. Naumann, "Analytical applications of Fourier transform-infrared (FT-IR) spectroscopy in microbiology and prion research," *Veterinary Microbiology*, vol. 123, no. 4, pp. 305–319, 2007.
- [25] K. C. Blakeslee and R. A. Condrate, "Vibrational spectra of hydrothermally prepared hydroxyapatites," *Journal of the American Ceramic Society*, vol. 54, no. 11, pp. 559–563, 1971.
- [26] K. J. Rothschild and N. A. Clark, "Anomalous amide I infrared absorption of purple membrane," *Science*, vol. 204, no. 4390, pp. 311–312, 1979.
- [27] R. A. Nyquist and R. O. Kagel, *Infrared Spectra of Inorganic Compounds*, Academic Press, New York, NY, USA, 1971.
- [28] J. Yang, M. J. Janik, D. Ma et al., "Location, acid strength, and mobility of the acidic protons in Keggin $12-H_3PW_{12}O_{40}$: a combined solid-state NMR spectroscopy and DFT quantum chemical calculation study," *Journal of the American Chemical Society*, vol. 127, no. 51, pp. 18274–18280, 2005.
- [29] A. E. R. S. Khdera, H. M. A. Hassana, and M. S. El-Shall, "Acid catalyzed organic transformations by heteropoly tungstophosphoric acid supported on MCM-41," *Applied Catalysis A*, vol. 411–412, pp. 77–86, 2012.
- [30] Y. S. Kim, F. Wang, M. Hickner, T. A. Zawodzinski, and J. E. McGrath, "Fabrication and characterization of heteropolyacid ($H_3PW_{12}O_{40}$)/directly polymerized sulfonated poly(arylene ether sulfone) copolymer composite membranes for higher temperature fuel cell applications," *Journal of Membrane Science*, vol. 212, no. 1–2, pp. 263–282, 2003.
- [31] L. Zhang, H. Q. He, R. Kamal S/O Abdul Rasheed et al., "Fabrication of novel phosphotungstic acid functionalized mesoporous silica composite membrane by alternative gel-casting technique," *Journal of Power Sources*, vol. 221, pp. 318–327, 2013.
- [32] L. Zhang, Q. Jin, L. Shan, Y. Liu, X. Wang, and J. Huang, " $H_3PW_{12}O_{40}$ immobilized on silylated palygorskite and catalytic activity in esterification reactions," *Applied Clay Science*, vol. 47, no. 3–4, pp. 229–234, 2010.
- [33] P. Staiti, S. Freni, and S. Hocevar, "Synthesis and characterization of proton-conducting materials containing dodecatungstophosphoric and dodecatungstosilic acid supported on silica," *Journal of Power Sources*, vol. 79, no. 2, pp. 250–255, 1999.
- [34] X. L. Sheng, Y. M. Zhou, Y. W. Zhang, M. W. Xue, and Y. Z. Duan, "Immobilization of 12-tungstophosphoric acid on LaSBA-15 and its catalytic activity for alkylation of o-xylene with styrene," *Chemical Engineering Journal*, vol. 179, pp. 295–301, 2012.
- [35] P. M. Rao, A. Wolfson, S. Kababya, S. Vega, and M. V. Landau, "Immobilization of molecular $H_3PW_{12}O_{40}$ heteropolyacid catalyst in alumina-grafted silica-gel and mesostructured SBA-15 silica matrices," *Journal of Catalysis*, vol. 232, no. 1, pp. 210–225, 2005.
- [36] J. Yuan, P. Yue, and L. Wang, "A study on the magnetically supported heteropolyacid nanophase catalysts," *Powder Technology*, vol. 202, no. 1–3, pp. 190–193, 2010.
- [37] H. T. Pu, F. J. Jiang, and Z. L. Yang, "Preparation and properties of soft magnetic particles based on Fe_3O_4 and hollow polystyrene microsphere composite," *Materials Chemistry and Physics*, vol. 100, no. 1, pp. 10–14, 2006.
- [38] Y. H. Guo, Y. H. Wang, C. W. Hu et al., "Microporous polyoxometalates/poms/ SiO_2 : synthesis and photocatalytic degradation of aqueous organochlorine pesticides," *Chemistry of Materials*, vol. 12, no. 11, pp. 3501–3508, 2000.
- [39] Y. Bin, Y. Zhou, Y. X. Jing et al., "Photocatalytic degradation of aqueous 4-chlorophenol by silica-immobilized polyoxometalates," *Environmental Science & Technology*, vol. 36, no. 6, pp. 1325–1329, 2002.
- [40] M. Mercier-Bonin, K. Ouazzani, P. Schmitz, and S. Lorthois, "Study of bioadhesion on a flat plate with a yeast/glass model system," *Journal of Colloid and Interface Science*, vol. 271, no. 2, pp. 342–350, 2004.
- [41] A. Bingol, H. Uzun, Y. K. Bayhan, A. Karagunduz, A. Cakici, and B. Keskinler, "Removal of chromate anions from aqueous stream by a cationic surfactant-modified yeast," *Bioresource Technology*, vol. 94, no. 3, pp. 245–249, 2004.
- [42] E. Rafiee and S. Shahebrahimi, "Nano silica with high surface area from rice husk as a support for 12-tungstophosphoric acid: an efficient nano catalyst in some organic reactions," *Chinese Journal of Catalysis*, vol. 33, no. 8, pp. 1326–1333, 2012.

Research Article

Au-TiO₂ Nanocomposites and Efficient Photocatalytic Hydrogen Production under UV-Visible and Visible Light Illuminations: A Comparison of Different Crystalline Forms of TiO₂

Deepa Jose,¹ Christopher M. Sorensen,² Sadhana S. Rayalu,^{1,3}
Khadga M. Shrestha,¹ and Kenneth J. Klabunde¹

¹ Department of Chemistry, Kansas State University, Manhattan, KS 66506, USA

² Department of Physics, Kansas State University, Manhattan, KS 66506, USA

³ Environmental Materials Division, National Environmental Engineering Research Institute (CSIR-NEERI), Nehru Marg, Nagpur, Maharashtra 440020, India

Correspondence should be addressed to Kenneth J. Klabunde; kenjk@ksu.edu

Received 14 January 2013; Revised 5 March 2013; Accepted 11 March 2013

Academic Editor: Elias Stathatos

Copyright © 2013 Deepa Jose et al. This is an open access article distributed under the Creative Commons Attribution License, which permits unrestricted use, distribution, and reproduction in any medium, provided the original work is properly cited.

Au_{(~1 wt%)/TiO₂(anatase or rutile or P25)} nanocomposites were prepared by the solvated metal atom dispersion (SMAD) method, and the as-prepared samples were characterized by diffuse reflectance UV-visible spectroscopy, powder XRD, BET surface analysis measurements, and transmission electron microscopy bright field imaging. The particle size of the embedded Au nanoparticles ranged from 1 to 10 nm. These Au/TiO₂ nanocomposites were used for photocatalytic hydrogen production in the presence of a sacrificial electron donor like ethanol or methanol under UV-visible and visible light illumination. These nanocomposites showed very good photocatalytic activity toward hydrogen production under UV-visible conditions, whereas under visible light illumination, there was considerably less hydrogen produced. Au/P25 gave a hydrogen evolution rate of 1600 μmol/h in the presence of ethanol (5 volume %) under UV-visible illumination. In the case of Au/TiO₂ prepared by the SMAD method, the presence of Au nanoparticles serves two purposes: as an electron sink gathering electrons from the conduction band (CB) of TiO₂ and as a reactive site for water/ethanol reduction to generate hydrogen gas. We also observed hydrogen production by water splitting in the absence of a sacrificial electron donor using Au/TiO₂ nanocomposites under UV-visible illumination.

1. Introduction

Ever since the first report of water splitting using a TiO₂ photoanode by Fujishima and Honda, researchers all over the world have been trying to develop efficient solar energy harvesting semiconductor materials for water splitting and thereby producing clean hydrogen energy [1]. Several strategies like band gap engineering of semiconductor materials, cocatalyst loading, two-step photoexcitation (Z scheme), and so forth have been developed to achieve efficient overall water splitting to produce hydrogen and oxygen [2–5]. Recently, people have been trying to exploit the UV and visible absorption of metal nanoparticles like Au, Ag, and Cu by embedding them on a semiconductor material [6, 7]. Among the various semiconductor catalysts, TiO₂ is one of the most promising

due to its high chemical stability, nontoxicity, and low cost [8]. The only limitation of TiO₂ as a photocatalyst is its poor efficiency in the visible region of the solar spectrum due to its wide band gap (3.2 eV for anatase). However, TiO₂ can show some visible photocatalytic activity due to the presence of some rutile form of TiO₂ and/or by doping it with metal or nonmetallic elements [9–11] or by deposition of noble metal nanoparticles on TiO₂ [12–15]. Metal nanoparticle loaded TiO₂ showed enhanced photocatalytic activity under UV or visible light illumination. The improved UV activity of these photocatalysts is attributed to the better charge separation by electron transfer from the conduction band (CB) of TiO₂ to Au nanoparticles [16–18], whereas the observed visible activity is explained as photoexcitation of Au nanoparticles (due to surface plasmon resonance effect) and charge separation

by the transfer of photoexcited electrons from Au to the CB of TiO₂ [16, 19–25]. There are some other reports explaining the enhanced visible activity of Au/TiO₂ due to local electric field enhancement near the TiO₂ surface by the Au surface plasmon resonance [26–29].

There are several methods reported in the literature for the synthesis of TiO₂ supported gold nanoparticles such as adsorption of preformed Au colloids [30], photodeposition [31, 32], deposition precipitation [33], impregnation [33], and chemical reduction [34]. We used a different approach for the synthesis of these Au loaded TiO₂ nanocomposites: the solvated metal atom dispersion (SMAD) method. The SMAD technique has been used extensively in our laboratories for the gram scale synthesis of nanoparticles of metals like Au, Ag, Cu, metal chalcogenides, [35–38]. The advantages of this method over other routes reported in the literature are that no byproducts are formed, reproducibility and scalability. We used different types of TiO₂: anatase (UV active), rutile (visible active), and P25 (a mixture of 75% anatase and 25% rutile) for Au loading. These Au (~1 wt%) loaded TiO₂ nanocomposites, prepared by the SMAD method were used as photocatalysts toward photocatalytic hydrogen production, in the presence or absence of a sacrificial electron donor ethanol (5 volume%) under UV-visible and visible conditions. This paper will discuss our findings regarding the role of Au nanoparticles and the role of different crystalline forms of TiO₂.

2. Materials and Methods

2.1. Materials. The different phases of TiO₂ used were anatase (Alfa Aesar, 99.9% and anatase prepared by aerogel method in our laboratories), rutile (Sigma Aldrich, 99.99%), and P25 (Degussa). Sodium sulfite (98.3%) was purchased from Fischer Scientific. Butanone (Sigma Aldrich, 99.7%) was distilled and freeze pump thaw processed for five cycles prior to use in SMAD experiments. Ethanol (200 Proof) from Decon Labs was used for photochemical reactions.

2.2. Instrumentation. Diffuse reflectance UV-visible spectra (DRS UV) were recorded using a Cary 500 scan UV-Vis-NIR spectrophotometer operating in air at room temperature over the range from 200 to 800 nm. Brunauer-Emmet-Teller (BET) measurements of surface area and pore size distribution of TiO₂ and Au/TiO₂ nanocomposites were determined using a Quantachrome NOVA 1200 N₂ gas adsorption/desorption analyzer at liquid nitrogen temperature. Powder XRD analysis of these samples was carried out using a Scintag-XDS-2000 spectrometer with Cu K α radiation with applied voltage of 40 kV and current of 40 mA. TEM bright field images were taken using a Phillips CM100 electron microscope operating at 100 kV. Bulk elemental analysis was carried out using Perkin Elmer Optima 4300DV spectrometer (ICP-OES) at Galbraith laboratories Inc.

2.3. Preparation of Au/TiO₂ Nanocomposites. Au loaded TiO₂ nanocomposites were prepared by the SMAD method. The details of the SMAD technique are given elsewhere [39].

In a typical experiment, the crucible was loaded with Au shot (~60 mg) and TiO₂ (P25, anatase commercial, anatase aerogel, or rutile) (~2960 mg) was placed in the bottom of the reactor. Liquid nitrogen cooling and vacuum were applied to the reactor and the crucible was heated resistively under vacuum in such a manner that there was cocondensation of Au atoms with solvent molecules (butanone) on the walls of the reactor. The reactor was brought up to room temperature under Ar atmosphere once the metal evaporation was complete. Upon matrix (Au-butanone) melt down, the Au-butanone colloid comes into contact with TiO₂ at the bottom of the reactor. The Au-butanone/TiO₂ mixture was stirred vigorously under Ar atmosphere for 2 h. The color of the slurry changed from dark blue to purple during the stirring process. Butanone was removed from the mixture by applying vacuum, and the dried powder was used for further studies. In addition to the vacuum drying, Au/TiO₂ samples for control experiments were calcined in air at 200°C for 2 h (heating rate, 5°C/min) to make sure that there was no butanone remaining. The catalysts prepared by the SMAD method are shown in Figure S1 (see Supplementary Material available online at doi: <http://dx.doi.org/10.1155/2013/685614>), and their color varied from lavender to purple.

2.4. Photocatalytic Water Splitting Experiments Using a 450 W Mercury Lamp. The photocatalytic water splitting experiments were carried out in a glass enclosed reaction chamber with a quartz inner radiation reaction vessel. The glass chamber was connected to a gas circulation evacuation and water cooling system. In a typical experiment, 255 mg catalyst (as prepared Au/TiO₂ or Au/TiO₂ calcined at 200°C for 2 h), 322 mL distilled water, and 18 mL ethanol (or 18 mL methanol or 20 mM sodium sulfite) as sacrificial electron donor was taken in the glass reactor with a magnetic stir bar. The reaction mixture was evacuated and filled with Ar five times to remove all the dissolved gases. This was followed by irradiation using a 450 W high pressure Hg lamp via a quartz tube. Water at 20°C was circulated continuously through the outer walls of the reactor and the quartz vessel to make sure that the temperature of the reaction mixture did not exceed 35°C [40]. The activity of these catalysts for hydrogen production was investigated during the first 5 h irradiation period, using a fresh catalyst each time. 2 M NaNO₂ solution was used as a filter to cut off UV radiation in our visible studies (UV-visible absorption spectrum of 2 M NaNO₂ is given in the supporting information). H₂ production was monitored using an online GC system (GOW-MAC 580 model) employing an All Tech molecular 80/100 sieve 5 A column with Ar as the carrier gas and a thermal conductivity detector.

3. Results and Discussions

3.1. Au/TiO₂ Nanocomposites Characterization. Au nanoparticles (~1 wt%) loaded on to a variety of anatase, rutile, and a mixture of anatase and rutile (P25) TiO₂ were prepared by the SMAD method. The as-prepared samples were characterized by diffuse reflectance UV-visible spectroscopy, BET surface area analysis, transmission electron microscopy, and

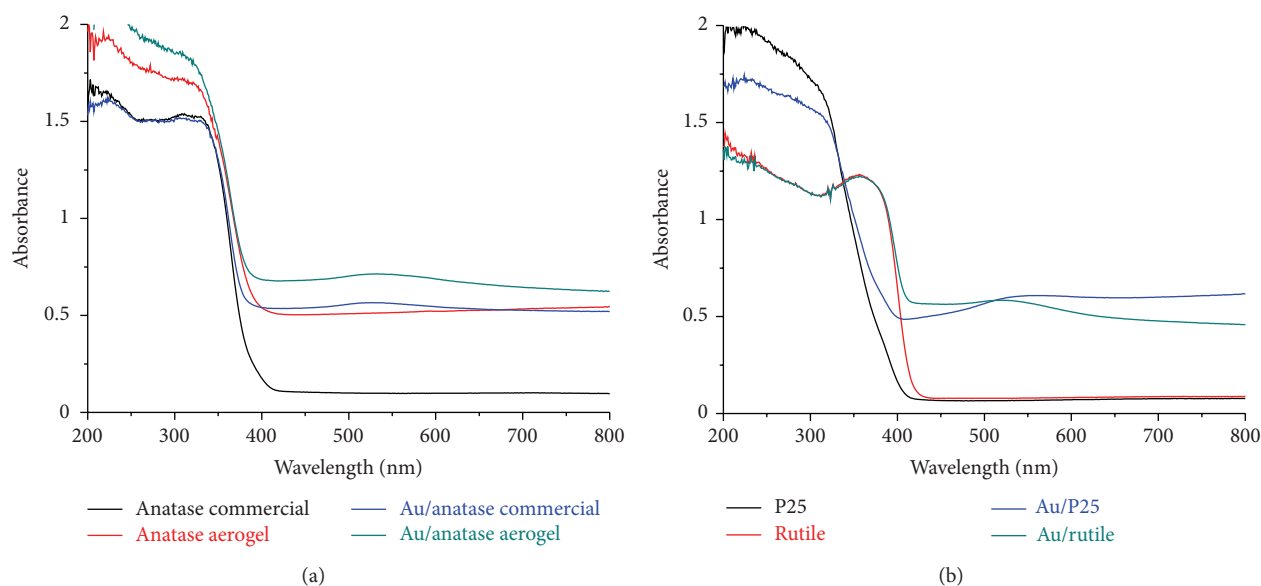


FIGURE 1: Diffuse reflectance UV-visible spectra of Au/TiO₂ photocatalysts prepared by the SMAD method.

powder XRD. The diffuse reflectance spectra of Au/TiO₂ nanocomposites showed 2 sets of peaks (Figure 1): band gap transition band of TiO₂ with a maximum in the UV region and surface plasmon resonance band in the visible region (Au/anatase commercial with a maxima at 526 nm, Au/anatase aerogel with a maxima at 535 nm, Au/rutile with a maxima at 525 nm, and Au/P25 with a maxima at 560 nm). The position and shape of the surface plasmon resonance band depends on particle size, shape, and dielectric constant of the medium [41]. The red shift of the surface plasmon band maxima in these nanocomposites can be attributed to the refractive index of the TiO₂ matrix. The band gap values of the respective phases of TiO₂ remained unchanged even after Au loading as per the DRS UV data (anatase = 3.2 eV, rutile = 3.0 eV, and P25 = 3.1 eV).

The presence of loaded Au nanoparticles on the TiO₂ matrix was confirmed by TEM bright field imaging. The TEM bright field images of different phases of TiO₂ before and after Au loading are given in Figures 2 and 3. Commercial anatase has micron sized particles (0.1-0.2 μm , Figure 2(a)) with a surface area 13 m²/g, whereas anatase prepared by the aerogel method consists of small nanometer sized particles (10–15 nm, Figure 2(b)) with a high surface area of 102 m²/g (Figure S1 and Table S1). TEM bright field images of these anatase particles showed embedded Au nanoparticles of size ranging from 1 to 9 nm (Figures 2(c) and 2(d)) with an average particle diameter of 2.4 nm and 4.3 nm (Figure 4) for aerogel and commercial anatase, respectively. The surface areas of these Au/anatase nanocomposites were less than the respective TiO₂ matrix used (Table S1). The rutile phase of TiO₂ used in our studies showed micron sized particles (0.2–0.6 μm , Figure 3(c)). The surface area of rutile was found to be very low (Table S1). The TEM bright field image (Figure 3(d)) showed embedded Au nanoparticles on the semiconductor with a size ranging from 3 to 8 nm with an average particle diameter of 4.7 nm (Figure 4). In the case of P25, the particles

size ranged from 15 to 20 nm (Figure 3(a)) with a surface area of about 48 m²/g (Table S1). TEM bright field images exhibited Au nanoparticles of size ranging from 3 to 10 nm (Figure 3(b)) with an average particle diameter of 6.7 nm (Figure 4). The powder XRD pattern (Figure S3) of these Au/TiO₂ nanocomposites did not show any Au reflections due to the low concentration (Table S2) of Au in these samples.

A conclusion from these characterization studies is that the final gold particle size depends a great deal on the surface area of the TiO₂ support. Therefore, as the Au-butanone colloid encountered the cold TiO₂, gold nanoparticle growth is limited/controlled by the TiO₂ surface available.

3.2. Photocatalytic Activity of Au/TiO₂ Nanocomposites under UV-Visible Conditions. All Au/TiO₂ photocatalysts prepared by our SMAD method showed UV-visible activity to generate hydrogen in the presence of a sacrificial electron donor, irrespective of the TiO₂ phase present in the system (Table 1). Among the different catalysts used, Au/P25 showed the highest activity with a hydrogen production rate of 1600 $\mu\text{mol/h}$ in the presence of ethanol. In addition to ethanol as a sacrificial agent, we used methanol and sodium sulfite as an electron scavenger in Au/P25 system. The rate of hydrogen evolution was lower compared to ethanol when methanol was used as the sacrificial agent with a photocatalytic hydrogen production of 816 $\mu\text{mol/h}$. The photocatalytic hydrogen production was very low when 20 mM sodium sulfite solution was used as a sacrificial agent (20 $\mu\text{mol/h}$). These results clearly indicate that during sacrificial electron donor mediated hydrogen production, there is a considerable contribution toward hydrogen generation from the sacrificial agent in addition to the hydrogen generation.

Au/TiO₂ photocatalysts were found to be much more active compared to their samples without gold. The higher activity could be attributed to the better charge separation

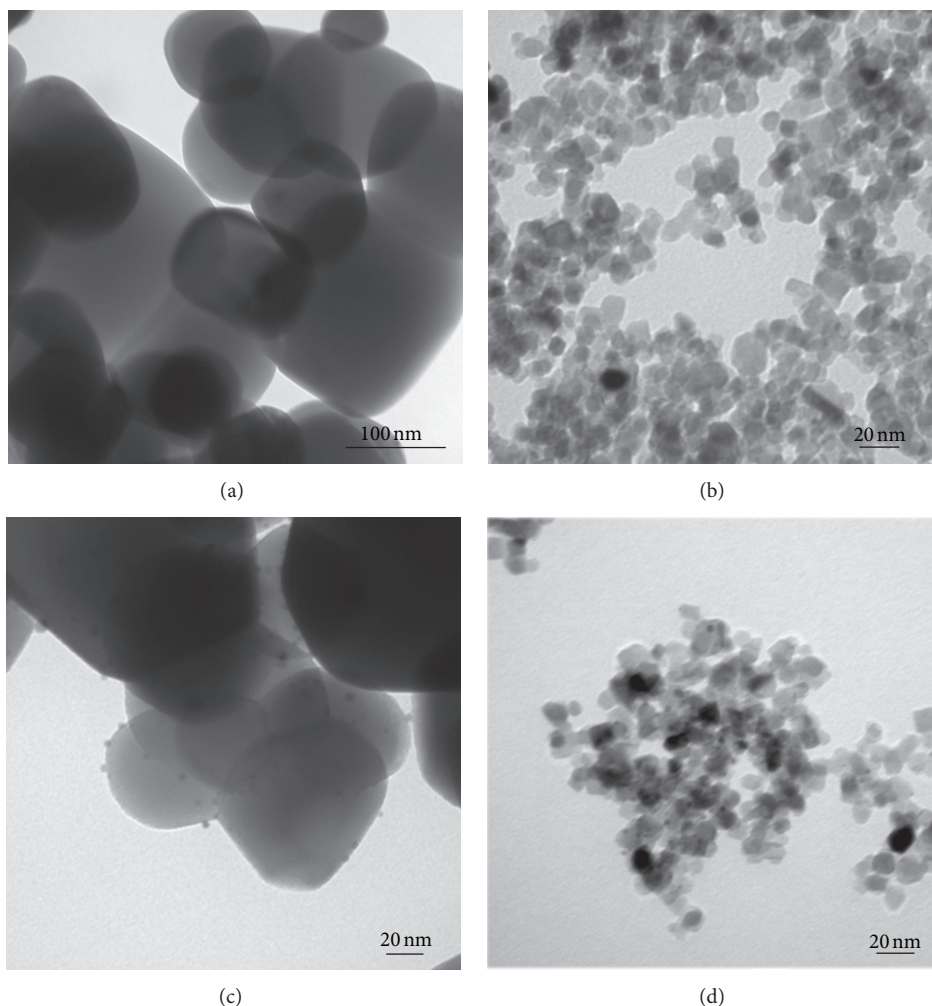


FIGURE 2: TEM bright field images of anatase phase of TiO_2 before and after Au loading (a) anatase commercial, (b) anatase aerogel, Au/ TiO_2 (c) Au/anatase commercial, and (d) Au/anatase aerogel.

TABLE 1: Amount of hydrogen evolved using Au/ TiO_2 nanocomposites under dark, visible, and UV-visible photocatalytic runs for 5 h in the presence of ethanol (5 volume%) using a 450 W Mercury lamp.

Catalyst	Rate ($\mu\text{mol/h}$)		
	Dark	Visible	UV-visible
No catalyst	0.0	0.0	2.2
P25	0.0	1.9	90
Au/P25	0.0	6.9	1600
Anatase commercial	0.0	0.0	1.7
Au/anatase commercial	0.0	0.0	300
Anatase aerogel	0.0	0.0	18
Au/anatase aerogel	0.0	0.0	1200
Rutile	0.0	3.3	6.3
Au/rutile	0.0	5.6	530

achieved in these catalysts where Au particles are good electron scavengers as well as catalyst surfaces for hydrogen formation. The subsequent holes in photoexcited TiO_2 are quenched by the sacrificial electron donor ethanol. The Fermi level of Au nanoparticles ($E_F = +0.45$ V versus NHE at pH 7 for bulk Au) is more positive than the bottom of the

conduction band of TiO_2 ($E_{CB} = -0.5$ V versus NHE at pH 7) which favors the electron transfer from photoexcited TiO_2 to Au. However, the reduction potential of water is -0.41 V (NHE at pH 7), and the transferred electrons cannot reduce water until the Fermi level of Au is raised to negative potentials. There are several reports in the literature regarding metal nanoparticle storing electrons in its Fermi level and shifting the Fermi level to more negative potentials when they come into contact with a photoexcited semiconductor nanoparticle like TiO_2 [17, 18, 42–46]. This kind of electron transfer from semiconductor to metal continues until Fermi level equilibration takes place. Choi et al. showed that under UV irradiation, Au@ TiO_2 core-shell nanoparticles exhibit a blue shift in the surface plasmon resonance band maxima due to the transfer of electrons from TiO_2 to Au core and the Fermi level shift to negative potentials [47]. Au cannot undergo this kind of the Fermi level shift without taking electrons from a semiconductor [47].

3.3. *Photocatalytic Activity of TiO_2 and Au/ TiO_2 Nanocomposites under Visible Conditions.* We used 2 M NaNO_2 solution as a filter to cut off the UV radiations under our

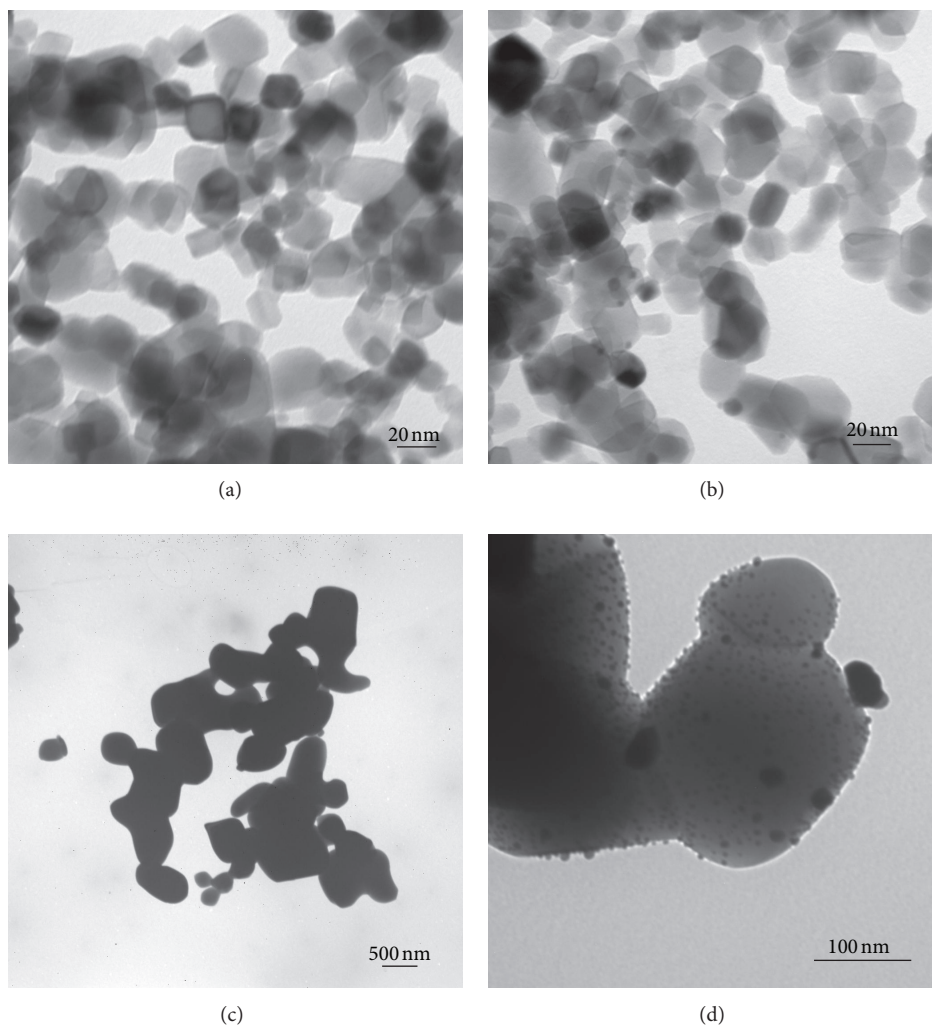


FIGURE 3: TEM bright field images of (a) P25, (b) Au/P25, (c) rutile, and (d) Au/rutile.

visible light illumination photocatalytic experiments. From the UV-visible spectrum of NaNO_2 (Figure S4) it is clear that this chemical filter cuts off radiation only up to 400 nm. Since rutile does absorb in the 400–410 nm range, some charge transfer from TiO_2 to Au could take place. As expected, the rutile phase of TiO_2 is visible light active, whereas the anatase phase is visible light inactive due to its slightly large band gap. Au loading improved the visible light activity of TiO_2 nanoparticles containing the rutile phase. Thus, the enhanced visible activity of these rutile-containing photocatalysts could be due to better charge separation in the presence of Au nanoparticles by transferring electrons from the CB of TiO_2 to the Au Fermi level [16–18].

In addition to the charge transfer from TiO_2 to Au, there are several reports where Au imparts visible activity to wide band gap visible light inactive semiconductor nanoparticles like TiO_2 , SrTiO_3 , and CeO_2 [19–25, 48–51]. García and coworkers prepared visible active Au loaded P25 or CeO_2 nanocomposites for hydrogen or oxygen production by water splitting in the presence of a sacrificial electron donor (methanol or EDTA) or acceptor [16, 48]. According to these reports, Au nanoparticles absorb visible light by the

surface plasmon resonance effect; charge separation at the Au nanoparticle takes place by the transfer of excited electrons from Au to the CB of TiO_2 ; subsequent holes are quenched by the sacrificial electron donor. Kimura et al. showed that the rutile form of TiO_2 more favors this kind of interfacial electron transfer from Au to TiO_2 [19]. Essentially, in these reported systems, Au nanoparticle acts as a sensitizer as in the case of dye-sensitized solar cells [49].

However, this kind of electron transfer from Au to the CB of TiO_2 is not energetically favored [26]. On the other hand, Tian and Tatsuma showed that this kind of electron transfer is possible due to the formation of a Schottky barrier at Au/ TiO_2 junctions [20, 50]. In the case of $\text{Pt}_{(0.5\text{ wt}\%)}/\text{SrTiO}_3$, the Pt metal decreases the band gap energy of SrTiO_3 by the formation of a Schottky barrier at the Pt/ SrTiO_3 interface [51]. Thus, there is still controversy regarding electron flow to or from metal particles with TiO_2 .

To get a better overall understanding about how Au nanoparticles impart visible activity to TiO_2 semiconductor, we examined the visible activity of Au/anatase nanocomposites. Two different types of anatase were used: a commercial one with micron sized particles and anatase prepared by an

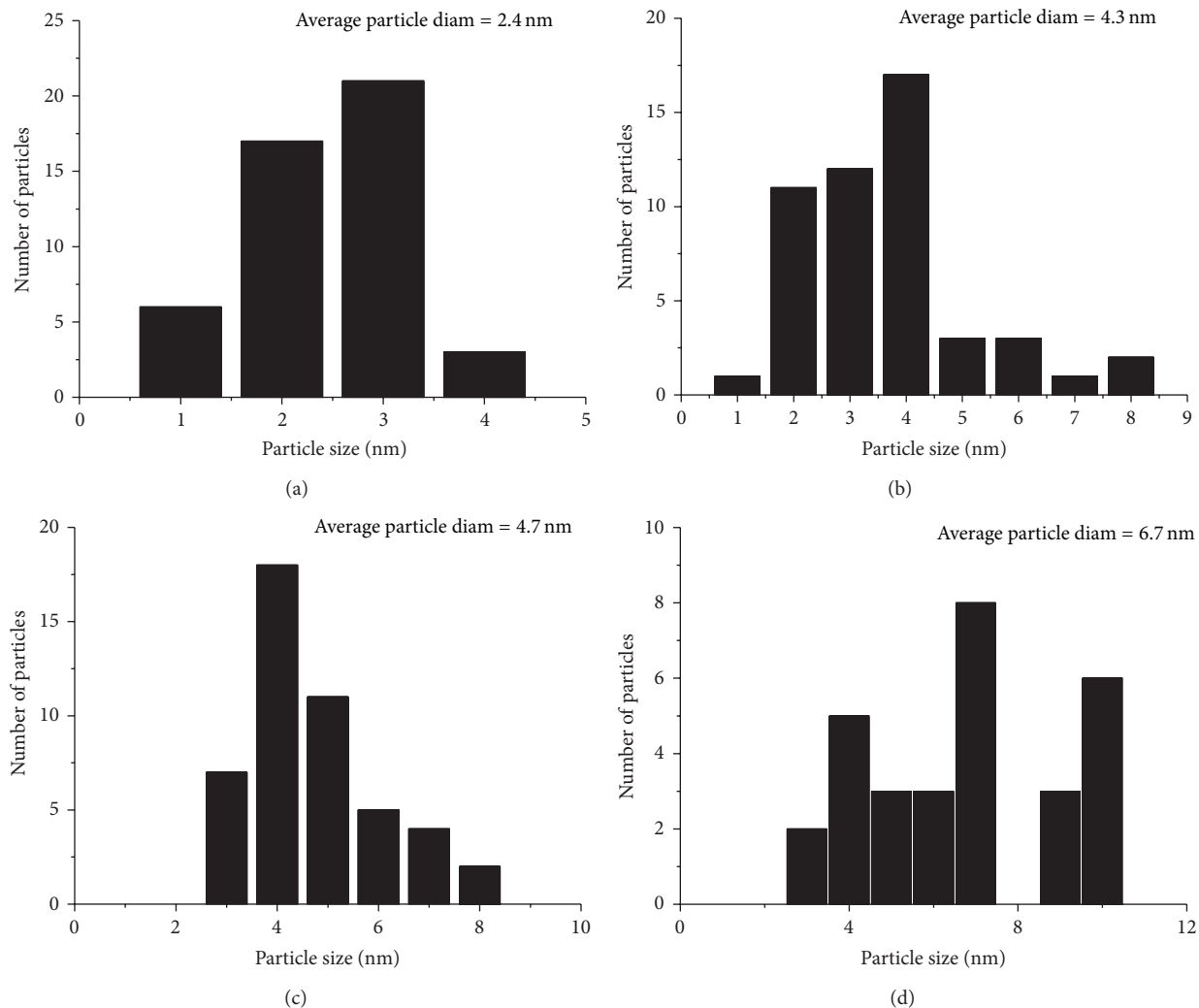
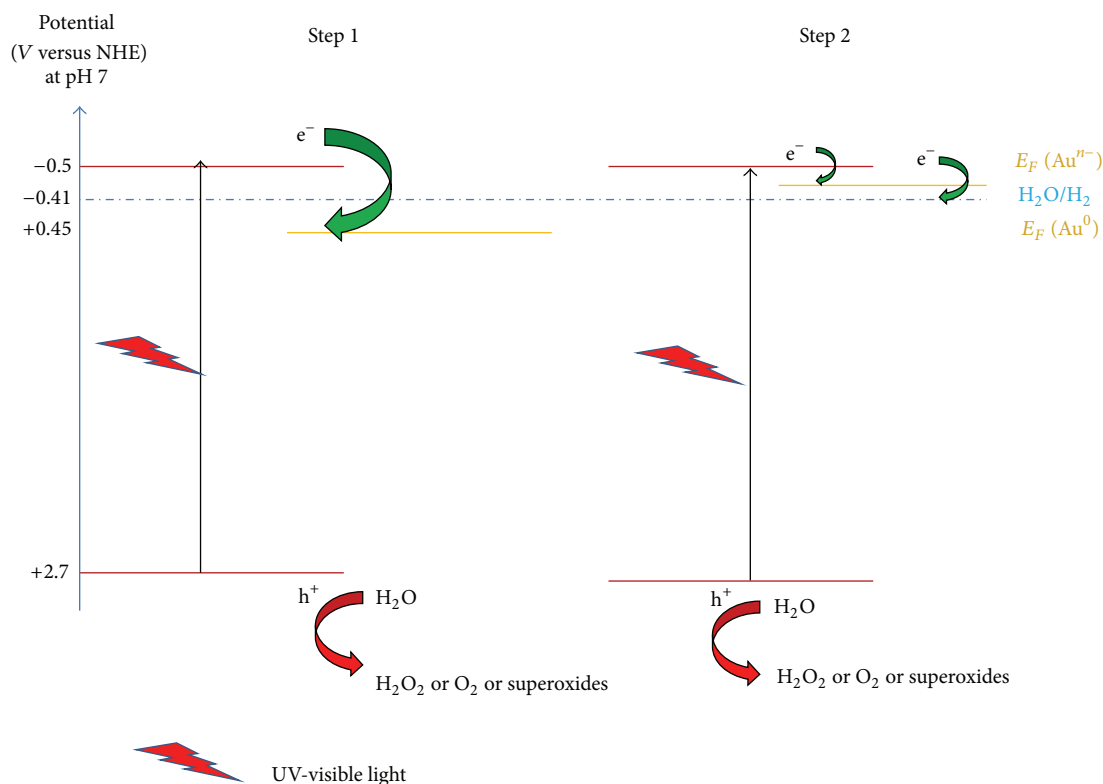


FIGURE 4: Histogram showing particle size distribution of Au nanoparticles loaded onto different phases of TiO_2 nanoparticles (a) Au/Anatase aerogel, (b) Au/anatase commercial, (c) Au/rutile, and (d) Au/P25.

aerogel method with nanometer sized particles. Regardless of the anatase used for Au loading, we did not see any visible light activity for the first five hours in the presence of water ethanol mixture. However, there was a very small amount of hydrogen evolution sixth-hour onwards. The mechanism of formation of small amount of hydrogen after five hours of visible light illumination is not clear to us, which could be either due to the reduction of water or due to the thermal decomposition of ethanol, aided by small nanoparticles undergoing nonradiative decay forming localized hot spots [52, 53].

It has also been reported that Au nanoparticles can also impart visible activity to a plasmonic-metal/semiconductor nanocomposite by surface plasmon mediated local electric field enhancement [26–29]. Interaction of a semiconductor nanoparticle with this kind of localized electric field could allow the formation of electron/hole pairs in the near surface region which can migrate to the surface without undergoing electron/hole pair recombination. For example, electromagnetic simulations showed that the increased photocatalytic

water splitting under visible illumination of anodic TiO_2 with Au nanoparticles is due to the local electric field enhancement near the TiO_2 surface instead of electron transfer from Au to the CB of TiO_2 [26]. Awazu et al. called this kind of surface plasmon-induced localized electric field enhancement and improved photocatalytic activity as “plasmonic photocatalysis” [54]. Christopher et al. explained the enhanced visible activity of Ag/TiO_2 as due to the higher concentration of charge carriers in the semiconductor by plasmon mediated radiative transfer of energy from Ag nanoparticles to TiO_2 , no electron flow from Ag to TiO_2 was observed [55]. Recently, Seh et al. showed enhanced visible light activity for the Janus shaped anatase $\text{Au}-\text{TiO}_2$ nanocomposites as due to the strong localization of plasmonic near fields close to the $\text{Au}-\text{TiO}_2$ interface and the coupling of plasmonic near fields to optical transitions involving localized electronic states in amorphous TiO_2 [29]. In our case, this kind of localized electric field created by Au nanoparticles could not generate electron/hole pairs in the near surface region of the semiconductor as the surface plasmon absorbance of Au



SCHEME 1: Elementary steps showing photocatalytic water splitting under UV-visible illumination using Au/TiO₂ nanocomposites: step 1 is electron transfer from the CB of photoexcited TiO₂ to the Au Fermi level, and step 2 is the Au Fermi level shift to negative potential by gathering photoexcited electrons from TiO₂ and water reduction.

nanoparticle does not overlap with the TiO₂ absorption spectrum. Linc and Ingram observed enhanced visible activity with Ag loaded N-TiO₂, whereas Au loaded N-TiO₂ did not show any significant enhancement in the photocurrent due to the red shift in the position of surface plasmon absorption band of Au nanoparticles compared to that of Ag [56].

3.4. Au Nanoparticles in Au/TiO₂ Nanocomposites Act as an Electron Sink for Better Charge Separation and Total Water Splitting. Our results indicate that there is a transfer of electrons from TiO₂ to Au and Au nanoparticle acts as a sink for photogenerated electrons. If this is true, Au nanoparticles could aid charge separation without using a sacrificial electron donor. We strengthened this hypothesis by doing photocatalytic water splitting under UV-visible conditions using Au/P25 nanocomposites in the absence of a sacrificial electron donor. There was an evolution of hydrogen (Figure 5) which again supports the proposed mechanism of charge separation achieved by Au nanoparticles (acts as a sink for photogenerated electrons and the Fermi level equilibration) and water molecules (quench the holes in the valence band of TiO₂). In order to prove that the hydrogen evolution is not caused by some organic impurities like butanone incorporated into the Au/P25 photocatalyst during sample preparation, we used calcined Au/P25 (at 200°C for 2 h). This sample showed photocatalytic activity for several cycles (Figure 5). We also did control experiments, wherein we used Degussa P25 and tried photocatalytic water splitting

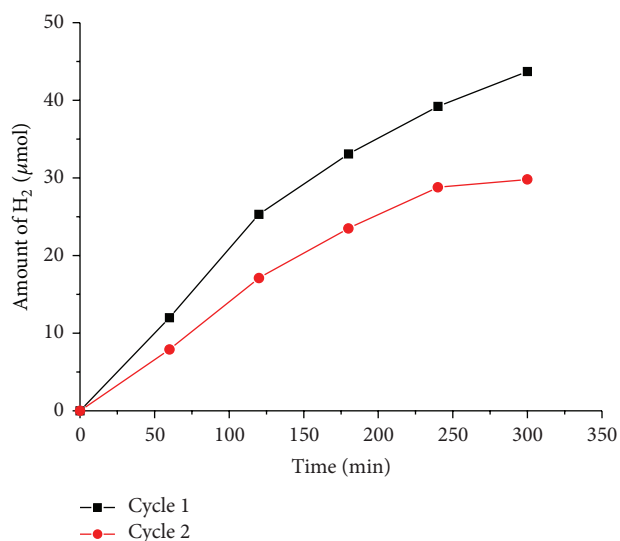


FIGURE 5: Hydrogen evolution by photocatalytic water splitting in the absence of sacrificial electron donor using Au/P25 (calcined sample) under UV-visible conditions.

in the absence of ethanol; there was no hydrogen evolution. These results imply a mechanism shown in Scheme 1.

The rate of hydrogen evolution was low for Au/P25 in the absence of ethanol. P25 produced no hydrogen in the absence of ethanol; however, in the presence of ethanol, there

was hydrogen evolution. This implies two things: (1) charge separation in pure TiO₂ takes place only in the presence of a sacrificial electron donor; (2) charge separation takes place in TiO₂ nanoparticles which are in good interfacial contact with Au nanoparticles even in the absence of a sacrificial electron donor. In the absence of ethanol, initially, charge separation takes place only on those TiO₂ particles which are in good interfacial contact with Au nanoparticles by transferring photoelectrons from the CB of TiO₂ to the Au Fermi level; holes are being quenched by water molecules to produce H₂O₂ or O₂. Thus, charge separation takes place in the case of photoexcited TiO₂ nanoparticles which are in good interfacial contact with TiO₂, and the Au/TiO₂ Fermi level equilibration takes place. Subsequent water reduction and hydrogen evolution are observed. The amount of hydrogen evolved in the absence of ethanol is low compared to the hydrogen evolved in the presence of ethanol. This could be due to the low concentration (1 wt%) of Au (which causes the charge separation) in these catalysts. We could not see any oxygen evolution during these experiments. This could be due to several reasons: (1) the reaction mixture was deaerated before photoillumination, and evolved small amount of oxygen could dissolve in water due to the high solubility of oxygen in water compared to hydrogen [57], (2) evolved oxygen can accept photoexcited electron from TiO₂ to form O₂^{•-} [58, 59]. The rate of the hydrogen evolution decreases with time as the evolved oxygen acts as a better electron acceptor to form superoxide.

4. Conclusions

These Au/TiO₂ photocatalysts were found to be resilient photocatalysts for the generation of hydrogen under UV-visible conditions. The photocatalytic hydrogen evolution rate was found to be 1600 μmol/h which is higher than Au/TiO₂ nanocomposites prepared by the photodeposition method (in our hands). Comparisons of different TiO₂ crystalline forms with different surface areas suggest that, in our case, the best explanation of any visible light activity is that the rutile form can absorb some energetic visible light, and then electrons are scavenged by the Au nanoparticles. This is the same mechanism as with more energetic UV light, where the process is much more efficient.

When ethanol scavenger is present, these photocatalysts are long lived. In the absence of ethanol, catalyst degradation takes place slowly (over days); this process of degradation is not understood, and hydrogen generation is much slower.

Further work comparing different metal nanoparticles is underway.

Conflict of Interests

The authors declare no financial conflict of interests.

Acknowledgments

The authors are grateful to the Department of Energy (Basic Energy Sciences, DE-SC 0005159) for funding. They thank Dr. Dan Boyle for assistance with TEM measurements.

References

- [1] A. Fujishima and K. Honda, "Electrochemical photolysis of water at a semiconductor electrode," *Nature*, vol. 238, no. 5358, pp. 37–38, 1972.
- [2] K. Maeda, "Photocatalytic water splitting using semiconductor particles: history and recent developments," *Journal of Photochemistry and Photobiology C*, vol. 12, no. 4, pp. 237–268, 2011.
- [3] K. Maeda and K. Domen, "Photocatalytic water splitting: recent progress and future challenges," *Journal of Physical Chemistry Letters*, vol. 1, no. 18, pp. 2655–2661, 2010.
- [4] R. Abe, "Recent progress on photocatalytic and photoelectrochemical water splitting under visible light irradiation," *Journal of Photochemistry and Photobiology C*, vol. 11, no. 4, pp. 179–209, 2010.
- [5] A. Kubacka, M. Fernández-García, and G. Colón, "Advanced nanoarchitectures for solar photocatalytic applications," *Chemical Society Reviews*, vol. 112, no. 3, pp. 1555–1614, 2012.
- [6] S. Linic, P. Christopher, and D. B. Ingram, "Plasmonic-metal nanostructures for efficient conversion of solar to chemical energy," *Nature Materials*, vol. 10, pp. 911–921, 2011.
- [7] S. C. Warren and E. Thimsen, "Plasmonic solar water splitting," *Energy Environmental Science*, vol. 5, pp. 5133–5146, 2012.
- [8] O. Carp, C. L. Huisman, and A. Reller, "Photoinduced reactivity of titanium dioxide," *Progress in Solid State Chemistry*, vol. 32, no. 1–2, pp. 33–177, 2004.
- [9] V. Brezová, A. Blažková, L. Karpinský et al., "Phenol decomposition using M^{III}/TiO₂ photocatalysts supported by the sol-gel technique on glass fibres," *Journal of Photochemistry and Photobiology A*, vol. 109, no. 2, pp. 177–183, 1997.
- [10] X. Wang, M. Blackford, K. Prince, and R. A. Caruso, "Preparation of boron-doped porous titania networks containing gold nanoparticles with enhanced visible-light photocatalytic activity," *ACS Applied Materials and Interfaces*, vol. 4, no. 1, pp. 476–482, 2012.
- [11] D. B. Hamal and K. J. Klabunde, "Synthesis, characterization, and visible light activity of new nanoparticle photocatalysts based on silver, carbon, and sulfur-doped TiO₂," *Journal of Colloid and Interface Science*, vol. 311, no. 2, pp. 514–522, 2007.
- [12] A. Primo, A. Corma, and H. García, "Titania supported gold nanoparticles as photocatalyst," *Physical Chemistry Chemical Physics*, vol. 13, no. 3, pp. 886–910, 2011.
- [13] X. Wang and R. A. Caruso, "Enhancing photocatalytic activity of titania materials by using porous structures and the addition of gold nanoparticles," *Journal of Materials Chemistry*, vol. 21, no. 1, pp. 20–28, 2011.
- [14] H. Tada, T. Kiyonaga, and S. I. Naya, "Rational design and applications of highly efficient reaction systems photocatalyzed by noble metal nanoparticle-loaded titanium(IV) dioxide," *Chemical Society Reviews*, vol. 38, no. 7, pp. 1849–1858, 2009.
- [15] V. Subramanian, E. Wolf, and P. V. Kamat, "Semiconductor-metal composite nanostructures. To what extent do metal nanoparticles improve the photocatalytic activity of TiO₂ films?" *Journal of Physical Chemistry B*, vol. 105, no. 46, pp. 11439–11446, 2001.
- [16] C. G. Silva, R. Juárez, T. Marino, R. Molinari, and H. García, "Influence of excitation wavelength (UV or visible light) on the photocatalytic activity of titania containing gold nanoparticles for the generation of hydrogen or oxygen from water," *Journal of the American Chemical Society*, vol. 133, no. 3, pp. 595–602, 2011.

- [17] V. Subramanian, E. E. Wolf, and P. V. Kamat, "Catalysis with TiO₂/Gold nanocomposites. Effect of metal particle size on the fermi level equilibration," *Journal of the American Chemical Society*, vol. 126, no. 15, pp. 4943–4950, 2004.
- [18] M. Jakob, H. Levanon, and P. V. Kamat, "Charge distribution between UV-irradiated TiO₂ and gold nanoparticles: determination of shift in the Fermi level," *Nano Letters*, vol. 3, no. 3, pp. 353–358, 2003.
- [19] K. Kimura, S. I. Naya, Y. Jin-nouchi, and H. Tada, "TiO₂ crystal form-dependence of the Au/TiO₂ plasmon photocatalyst's activity," *Journal of Physical Chemistry C*, vol. 116, no. 12, pp. 7111–7117, 2012.
- [20] Y. Tian and T. Tatsuma, "Mechanisms and applications of plasmon-induced charge separation at TiO₂ films loaded with gold nanoparticles," *Journal of the American Chemical Society*, vol. 127, no. 20, pp. 7632–7637, 2005.
- [21] D. Tsukamoto, Y. Shiraiishi, Y. Sugano, S. Ichikawa, S. Tanaka, and T. Hirai, "Gold nanoparticles located at the interface of anatase/rutile TiO₂ particles as active plasmonic photocatalysts for aerobic oxidation," *Journal of American Chemical Society*, vol. 134, no. 14, pp. 6309–6315, 2012.
- [22] A. Furube, L. Du, K. Hara, R. Katoh, and M. Tachiya, "Ultrafast plasmon-induced electron transfer from gold nanodots into TiO₂ nanoparticles," *Journal of the American Chemical Society*, vol. 129, no. 48, pp. 14852–14853, 2007.
- [23] Y. Nishijima, K. Ueno, Y. Kotake, K. Murakoshi, H. Inoue, and H. Misawa, "Near-infrared plasmon-assisted water oxidation," *Journal of Physical Chemistry Letters*, vol. 3, no. 10, pp. 1248–1252, 2012.
- [24] Y. Nishijima, K. Ueno, Y. Yokota, K. Murakoshi, and H. Misawa, "Plasmon-assisted photocurrent generation from visible to near-infrared wavelength using a Au-nanorods/TiO₂ electrode," *Journal of Physical Chemistry Letters*, vol. 1, no. 13, pp. 2031–2036, 2010.
- [25] E. Kowalska, O. O. P. Mahaney, R. Abe, and B. Ohtani, "Visible-light-induced photocatalysis through surface plasmon excitation of gold on titania surfaces," *Physical Chemistry Chemical Physics*, vol. 12, no. 10, pp. 2344–2355, 2010.
- [26] Z. Liu, W. Hou, P. Pavaskar, M. Aykol, and S. B. Cronin, "Plasmon resonant enhancement of photocatalytic water splitting under visible illumination," *Nano Letters*, vol. 11, pp. 1111–1116, 2011.
- [27] H. Wang, T. You, W. Shi, J. Li, and L. Guo, "Au/TiO₂/Au as a plasmonic coupling photocatalyst," *Journal of Physical Chemistry C*, vol. 116, no. 10, pp. 6490–6494, 2012.
- [28] Y. Lu, H. Yu, S. Chen, X. Quan, and H. Zhao, "Integrating plasmonic nanoparticles with TiO₂ photonic crystal for enhancement of visible-light-driven photocatalysis," *Energy Environmental Science*, vol. 46, pp. 1724–1730, 2012.
- [29] Z. W. Seh, S. Liu, M. Low et al., "Janus Au-TiO₂ photocatalysts with strong localization of plasmonic near-fields for efficient visible-light hydrogen generation," *Advanced Materials*, vol. 24, no. 17, pp. 2310–2314, 2012.
- [30] J. Li and H. C. Zeng, "Preparation of monodisperse Au/TiO₂ nanocatalysts via self-assembly," *Chemistry of Materials*, vol. 18, no. 18, pp. 4270–4277, 2006.
- [31] T. Soejima, H. Tada, T. Kawahara, and S. Ito, "Formation of au nanoclusters on TiO₂ surfaces by a two-step method consisting of Au(III)-complex chemisorption and its photoreduction," *Langmuir*, vol. 18, no. 11, pp. 4191–4194, 2002.
- [32] C. Yogi, K. Kojima, T. Takai, and N. Wada, "Photocatalytic degradation of methylene blue by Au-deposited TiO₂ film under UV irradiation," *Journal of Materials Science*, vol. 44, no. 3, pp. 821–827, 2009.
- [33] W.-C. Li, M. Comotti, and F. Schüth, "Highly reproducible syntheses of active Au/TiO₂ catalysts for CO oxidation by deposition-precipitation or impregnation," *Journal of Catalysis*, vol. 237, no. 1, pp. 190–196, 2006.
- [34] M. C. Hidalgo, M. Maicu, J. A. Navío, and G. Colón, "Effect of sulfate pretreatment on gold-modified TiO₂ for photocatalytic applications," *Journal of Physical Chemistry C*, vol. 113, no. 29, pp. 12840–12847, 2009.
- [35] S. Stoeva, K. J. Klabunde, C. M. Sorensen, and I. Dragieva, "Gram-scale synthesis of monodisperse gold colloids by the solvated metal atom dispersion method and digestive ripening and their organization into two- and three-dimensional structures," *Journal of the American Chemical Society*, vol. 124, no. 10, pp. 2305–2311, 2002.
- [36] A. B. Smetana, K. J. Klabunde, and C. M. Sorensen, "Synthesis of spherical silver nanoparticles by digestive ripening, stabilization with various agents, and their 3-D and 2-D superlattice formation," *Journal of Colloid and Interface Science*, vol. 284, no. 2, pp. 521–526, 2005.
- [37] A. A. Ponce and K. J. Klabunde, "Chemical and catalytic activity of copper nanoparticles prepared via metal vapor synthesis," *Journal of Molecular Catalysis A*, vol. 225, no. 1, pp. 1–6, 2005.
- [38] S. Cingarapu, Z. Yang, C. M. Sorensen, and K. J. Klabunde, "Synthesis of CdSe quantum dots by evaporation of bulk CdSe using SMAD and digestive ripening processes," *Chemistry of Materials*, vol. 21, no. 7, pp. 1248–1252, 2009.
- [39] K. J. Klabunde, P. L. Timms, P. S. Skell, and S. Ittel, "Introduction to metal vapor synthesis," *Inorganic Synthesis*, vol. 19, pp. 59–86, 1979.
- [40] Y. Kuo, C. D. Frye, M. Ikenberry, and K. J. Klabunde, "Titanium-indium oxy(nitride) with and without RuO₂ loading as photocatalysts for hydrogen production under visible light from water," *Catalysis Today*, vol. 199, pp. 15–23, 2013.
- [41] K. L. Kelly, E. Coronado, L. L. Zhao, and G. C. Schatz, "The optical properties of metal nanoparticles: the influence of size, shape, and dielectric environment," *Journal of Physical Chemistry B*, vol. 107, no. 3, pp. 668–677, 2003.
- [42] P. V. Kamat, "Manipulation of charge transfer across semiconductor interface. A criterion that cannot be ignored in photocatalyst design," *Journal of Physical Chemistry Letters*, vol. 3, no. 5, pp. 663–672, 2012.
- [43] A. Takai and P. V. Kamat, "Capture, store and discharge. Shuttling photogenerated electrons across TiO₂-silver interface," *ACS Nano*, vol. 5, no. 9, pp. 7369–7376, 2011.
- [44] V. Subramanian, E. E. Wolf, and P. V. Kamat, "Green emission to probe photoinduced charging events in ZnO-Au nanoparticles. Charge distribution and Fermi-level equilibration," *Journal of Physical Chemistry B*, vol. 107, no. 30, pp. 7479–7485, 2003.
- [45] T. Hirakawa and P. V. Kamat, "Photoinduced electron storage and surface plasmon modulation in Ag TiO₂ clusters," *Langmuir*, vol. 20, no. 14, pp. 5645–5647, 2004.
- [46] A. Wood, M. Giersig, and P. Mulvaney, "Fermi level equilibration in quantum dot-metal nanojunctions," *Journal of Physical Chemistry B*, vol. 105, no. 37, pp. 8810–8815, 2001.
- [47] H. Choi, W. T. Chen, and P. V. Kamat, "Know thy metal neighbor. Plasmonic versus electron charging effects of gold nanoparticles in dye sensitized solar cells," *ACS Nano*, vol. 6, no. 5, pp. 4418–4427, 2012.

- [48] A. Primo, T. Marino, A. Corma, R. Molinari, and H. García, "Efficient visible-light photocatalytic water splitting by minute amounts of gold supported on nanoparticulate CeO_2 obtained by a biopolymer templating method," *Journal of the American Chemical Society*, vol. 133, no. 18, pp. 6930–6933, 2011.
- [49] B. O'Regan and M. Grätzel, "A low-cost, high-efficiency solar cell based on dye-sensitized colloidal TiO_2 films," *Nature*, vol. 353, no. 6346, pp. 737–740, 1991.
- [50] J. Tang, M. White, G. D. Stucky, and E. W. McFarland, "Electrochemical fabrication of large-area Au/TiO_2 junctions," *Electrochemistry Communications*, vol. 5, no. 6, pp. 497–501, 2003.
- [51] T. Puangpetch, T. Sreethawong, S. Yoshikawa, and S. Chavadej, "Hydrogen production from photocatalytic water splitting over mesoporous-assembled SrTiO_3 nanocrystal-based photocatalysts," *Journal of Molecular Catalysis A*, vol. 312, no. 1-2, pp. 97–106, 2009.
- [52] C.-W. Yen and M. A. El-Sayed, "Plasmonic field effect on the hexacyanoferrate (III)-thiosulfate electron transfer catalytic reaction on gold nanoparticles: electromagnetic or thermal?" *Journal of Physical Chemistry C*, vol. 113, no. 45, pp. 19585–19590, 2009.
- [53] J. R. Adleman, D. A. Boyd, D. G. Goodwin, and D. Psaltis, "Heterogenous catalysis mediated by plasmon heating," *Nano Letters*, vol. 9, no. 12, pp. 4417–4423, 2009.
- [54] K. Awazu, M. Fujimaki, C. Rockstuhl et al., "A plasmonic photocatalyst consisting of silver nanoparticles embedded in titanium dioxide," *Journal of the American Chemical Society*, vol. 130, no. 5, pp. 1676–1680, 2008.
- [55] P. Christopher, D. B. Ingram, and S. Linic, "Enhancing photochemical activity of semiconductor nanoparticles with optically active Ag nanostructures: photochemistry mediated by Ag surface plasmons," *Journal of Physical Chemistry C*, vol. 114, no. 19, pp. 9173–9177, 2010.
- [56] D. B. Ingram and S. Linic, "Water splitting on composite plasmonic-metal/semiconductor photoelectrodes: evidence for selective plasmon-induced formation of charge carriers near the semiconductor surface," *Journal of the American Chemical Society*, vol. 133, no. 14, pp. 5202–5205, 2011.
- [57] http://www.engineeringtoolbox.com/gases-solubility-water-d_1148.html.
- [58] J. Kiwi and M. Grätzel, "Optimization of conditions for photochemical water cleavage. Aqueous Pt/TiO_2 (anatase) dispersions under ultraviolet light," *Journal of Physical Chemistry*, vol. 88, no. 7, pp. 1302–1307, 1984.
- [59] M. V. Rao, K. Rajeshwar, V. R. Pal Verneker, and J. DuBow, "Photosynthetic production of H_2 and H_2O_2 on semiconducting oxide grains in aqueous solutions," *Journal of Physical Chemistry*, vol. 84, no. 15, pp. 1987–1991, 1980.

Research Article

Bulky Macroporous TiO₂ Photocatalyst with Cellular Structure via Facile Wood-Template Method

Qingfeng Sun,^{1,2} Yun Lu,¹ Jinchun Tu,³ Dongjiang Yang,⁴ Jun Cao,² and Jian Li¹

¹ Material Science and Engineering College, Northeast Forestry University, Harbin 150040, China

² College of Mechanical and Electrical Engineering, Northeast Forestry University, Harbin 150040, China

³ Key Laboratory of Tropical Biological Resources of Ministry of Education, College of Materials and Chemical Engineering, Hainan University, Haikou 570228, China

⁴ College of Chemistry, Chemical and Environmental Engineering, Qingdao University, Qingdao 266071, China

Correspondence should be addressed to Jun Cao; zdhcj@126.com and Jian Li; jianli@nefu.edu.cn

Received 20 January 2013; Revised 14 March 2013; Accepted 15 March 2013

Academic Editor: Elias Stathatos

Copyright © 2013 Qingfeng Sun et al. This is an open access article distributed under the Creative Commons Attribution License, which permits unrestricted use, distribution, and reproduction in any medium, provided the original work is properly cited.

We report a bulky macroporous TiO₂ particles with cellular structure prepared in the presence of wood slices as template. Firstly, TiO₂ sol was coated onto the wood slices by repeated dip-coating process. Then, after calcinations at 550°C, the wood template could be removed, and the bulky TiO₂ structure was obtained. The prepared samples were characterized by scanning electron microscopy (SEM), X-ray diffraction (XRD), energy dispersive spectroscopy (EDS), and transmission electron microscope (TEM) techniques. XRD pattern confirmed the crystalline phase of the wood-templated TiO₂ is anatase phase. And interestingly, from the observation of SEM image, the wood-templated TiO₂ inherited the initial cellular structures of birch lumber (*B. albosinensis* Burk), and numerous macropores were observed in the sample. Meanwhile, the wood-templated TiO₂ presented a superior photocatalytic ability to decompose Rhodamine B (RhB) under ultraviolet irradiation.

1. Introduction

Template-directed synthesis is currently one of the most widely used methods for fabricating inorganic materials on account of its facility and versatility [1–4]. In addition to some artificial templates like latex particles [5], polymer foams [6], ion-exchange resins [7], and carbon fibers [8], many natural templates have been attracted to much attention for constructing a number of inorganic materials. The natural species utilized as templates for the formation of inorganic materials are available from bacterial superstructures [9], insect wings [10], wool and cotton/cloth textile [11], diatoms [12], dog and human hair [13], living cells [14], mushroom gills [13], plant leaves [10], paper [15], pollen grains [16], shell membrane [17], silk fiber [13], skeletal plates [18], spider silk [8, 10], and wood [19–24]. These materials from nature combine many inspiring properties, such as sophistication, miniaturization, hierarchical organizations, hybridization, resistance, and adaptability, after billions of years of stringent selection processes [4]. From the research results, using

natural species as template for building inorganic materials is an effective strategy to obtain morphology controllable materials with structural specialty, complexity, and related unique properties.

Among these natural templates, wood is a naturally grown composite material possessing complex hierarchical cellular and pit structures that are comprised principally of biopolymers, mainly cellulose, hemicellulose, and lignin [25, 26]. The wood vessels and fibers are hollow tubes, and the arrangement of these vessels and fibers varies considerably different with different wood species. The cellular structural hierarchy of wood ranges from the millimeter scale of the growth ring and longitudinal tracheid, the micrometer scale of the cell wall and diameter, to the nanometer scale of the molecular fiber and membrane structure of the cell wall. The open porosity is accessible for liquid or gaseous infiltration [3, 20]. These features of wood make it a perfect candidate as a template for generating porous inorganic materials with both structural and morphological complexities. Previously some efforts have been made

toward transforming wood cellular structures into inorganic SiC [27, 28], TiC [29], and macroporous zeolites [20]. By impregnating the wood templates with metal alkoxide solutions and applying standard sol-gel chemistry, various metal oxide porous materials, such as TiO₂ [30], Al₂O₃ [31], Fe₂O₃ [21], and Cr₂O₃ [32], have been produced using this approach.

In these inorganic materials, TiO₂ is one of the most promising functional materials and extensively used in photocatalysis [33, 34], solar cells [35], and paints [36] because of its superior chemical stability and nontoxicity [37, 38]. TiO₂ exists mainly in four polymorphs in nature, anatase (tetragonal, space group *I4₁/amd*), rutile (tetragonal, space group *P4₂/mnm*), brookite (orthorhombic, space group *Pbca*), and TiO₂(B) (monoclinic, space group *C2/m*) [39–42]. In photocatalytic study, anatase TiO₂ is generally considered to be more active than rutile crystalline [43]. Moreover, anatase TiO₂ with higher crystallinity is preferred for photocatalysis, since higher crystallinity means fewer defects for the recombination of photogenerated electrons and holes [36]. In the current research, different kinds of TiO₂ nanomaterials like nanoparticles, nanosheet, nanotube, or nanofiber have been fabricated using different method. However, TiO₂ with wood structures has been seldom reported.

To this purpose, we developed an efficient pathway to synthesize wood-templated TiO₂. The morphology, chemical compositions, and crystalline phase of the prepared TiO₂ were characterized by SEM, EDS, HRTEM, and XRD, respectively. Furthermore, the photocatalytic activity of the wood-templated TiO₂ was measured under UV irradiation.

2. Materials and Method

2.1. Raw Materials. All the chemicals were supplied by Shanghai Boyle Chemical Co. Ltd. and used as received. The air-dried birch lumber (*B. albosinensis* Burk) was cut into slices with a size of 20 mm (tangential) × 20 mm (radial) × 2 mm (longitudinal). The wood slices were pretreated in a Soxhlet apparatus with 95% ethanol at 80°C for 6 h under reflux to remove the extracts like the fats and fatty acids in the wood. Then these slices were rinsed with deionized water. Finally, the treated wood slices were vacuumly dried at 60°C for over 24 hours.

2.2. Preparation of TiO₂ Sol. Tetrabutylorthotitanate (TBOT), diethanolamine (DEA), and absolute ethanol were used as starting materials. The 34 mL of TBOT and 11 mL of DEA were dissolved in 100 mL ethanol to prepare the precursor solution. After stirring for 2 h at room temperature, a mixed solution of 55 mL water and 9 mL ethanol was dropwise added following stirred another 3 h. Then TiO₂ sol was obtained.

2.3. Fabrication of Wood-Templated TiO₂. Firstly, wood slices were coated by TiO₂ sol through a repeated dip-coating process. The pretreated wood slices were immersed into the as-prepared TiO₂ sol for 5 min. After that, these slices were

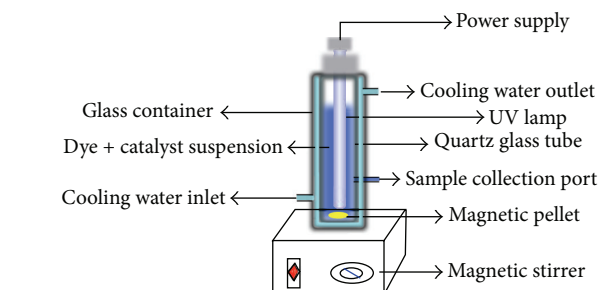


FIGURE 1: The schematic diagram of the photocatalytic reactor.

dried at 80°C for 3 h. This process was repeated for 5 times to ensure TiO₂ sol densely and evenly covered onto the wood slices. Then, calcination process was employed to remove the wood template. To get wood-templated TiO₂, wood coated by TiO₂ sol was calcined in a muffle furnace at the temperature of 550°C for 3 h in air atmosphere and air cooled to room temperature. Finally, the calcined samples were taken out from the muffle furnace, and the wood-templated TiO₂ was obtained.

2.4. Characterizations. The morphology of the samples was observed by scanning electron microscopy (SEM, FEI, Quanta 200) and transmission electron microscopy (TEM, FEI Tecnai F20). The chemical compositions of the untreated and treated wood were measured by energy dispersive spectroscopy (EDS, attached to the SEM). The crystalline structures were identified by X-ray diffraction (XRD, Rigaku, D/MAX 2200) operating with Cu K α radiation ($\lambda = 1.5418 \text{ \AA}$) at a scan rate (2θ) of 4°/min with an accelerating voltage of 40 kV and an applied current of 30 mA ranging from 10° to 70°.

2.5. Evaluation of Photocatalytic Activity. The photocatalytic activity of the samples was estimated through the decomposition of Rhodamine B (RhB) in a reactor with a volume of 100 mL. The irradiation source was an ultraviolet 100 W lamp (Shanghai Rongbo Co., China) with a wavelength of 254 nm. The photocatalytic activities of the prepared products were judged by measuring the loss of RhB in aqueous solution. A suspension involving 100 mg of catalyst and 100 mL RhB solution with an original concentration of 50 mg/L was magnetically stirred on the dark for 1 h without interrupting before irradiation. The change of solution concentration in every 30 min was measured to judge the absorbability of catalysts in the dark. At every interval during the process of 3 h, a certain sample of the mixture was collected, centrifuged, and then measured. The degradation rate for denoting the degradation efficiency of RhB was obtained by measuring the change in absorbance on a UV-Vis spectrophotometer (TU-190, Beijing Purkinje, China), and its maximum absorption wavelength of RhB was 554.5 nm. The schematic diagram of the photocatalytic reactor was represented in Figure 1.

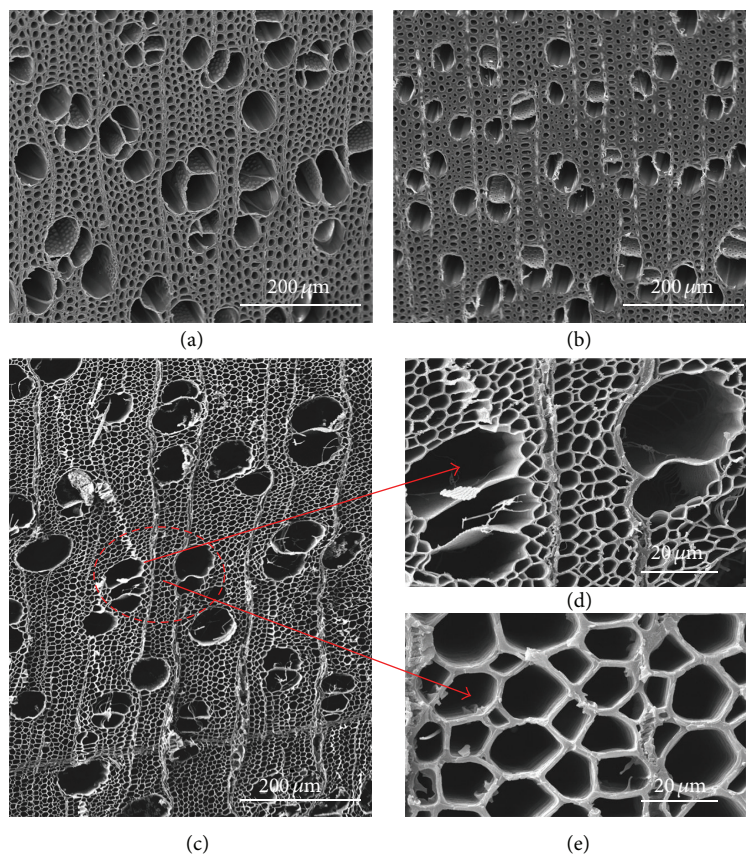


FIGURE 2: SEM images of the cross-section of (a) the original wood, (b) the wood coated by TiO_2 sol, (c) wood-templated TiO_2 , (d) the magnified calcined wood vessels, and (e) the magnified calcined wood fibers, respectively.

3. Results and Discussion

Figure 2 showed the morphologies of the cross-section of the original wood, wood coated by TiO_2 sol, and wood-templated TiO_2 , respectively. As shown in Figure 2(a), the cellular structures of the original wood could be clearly observed. The wood vessels with the diameter of about $20\sim 50\ \mu\text{m}$ are irregular circular. The wood fibers with the diameter of about $5\sim 20\ \mu\text{m}$ are uniformly arranged among the wood vessels. In Figure 2(b), the wood structure has not obviously changed after the dip-coating process by TiO_2 sol. It can be clearly seen from the Figure 2(c) that the structures of the original wood were commendably remained after the calcined process. In the magnified SEM image (Figure 2(d)), calcined wood vessels with a little collapse could be obviously observed with the diameter of about $35\ \mu\text{m}$. Simultaneously, the calcined wood fibers shown in Figure 2(e) with a thinner cellular wall compared to the original wood were well arranged without any collapse. The diameters of these fibers are about $15\ \mu\text{m}$. In a word, TiO_2 with the wood cellular structure was successfully prepared by dip-coating and calcination process. The microscopic structures of the original wood could not be destroyed with the previous process.

EDS spectra were also recorded for the original wood, wood coated by TiO_2 sol, and wood-templated TiO_2 , respectively. As shown in Figure 3(a), the carbon, oxygen, and

gold elements could be detected from the EDS spectrum of the original wood. The elements of carbon and oxygen are originated from the wood substrate, and the element of gold is from the coating layer used for SEM observation. Besides the signal of carbon and oxygen elements, titanium and nitrogen elements were displayed in the spectrum of TiO_2 sol-coated wood slices (Figure 3(b)). The elements of titanium and nitrogen are stemmed from TBOT and DEA in the TiO_2 sol, respectively. After calcination at 550°C , only oxygen and titanium elements could be probed from the EDS spectrum (Figure 3(c)), and no other elements were detected which confirmed that the components of the original wood and the TiO_2 precursor were completely removed during the calcination process.

XRD patterns of the original wood, the wood coated by TiO_2 sol, and wood-templated TiO_2 were presented in Figure 4. Figure 4(a) revealed a typical XRD pattern of the original wood. The diffraction peaks at 16° and 22.6° were believed to represent the crystalline region of the cellulose in wood [25]. In Figure 4(b), no other new diffraction peaks were founded except for the diffractive characteristics of the initial wood, which might be due to that the crystal phase of TiO_2 sol is consisted of amorphous TiO_2 before the calcination. Apparently, in Figure 4(c), the diffraction peaks at 16° and 22.6° belonging to the original wood sample disappeared. New strong diffraction peaks were observed

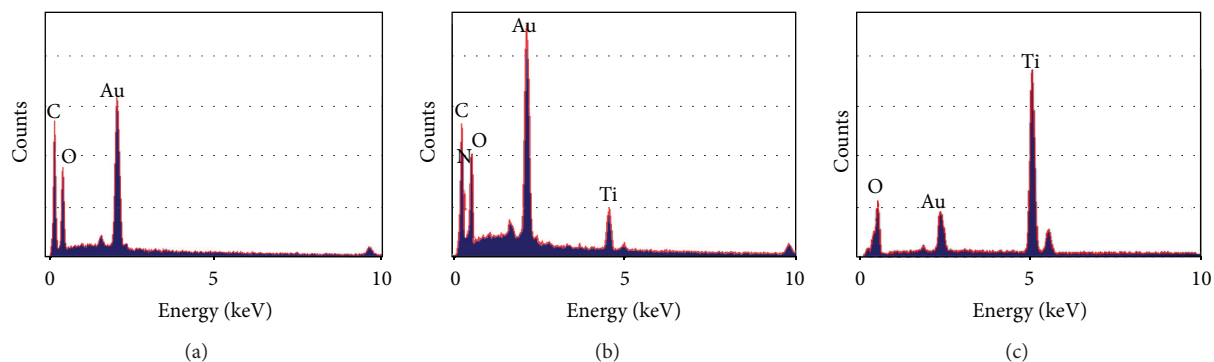


FIGURE 3: EDS spectra of (a) the original wood, (b) wood coated by TiO_2 sol, and (c) wood-templated TiO_2 .

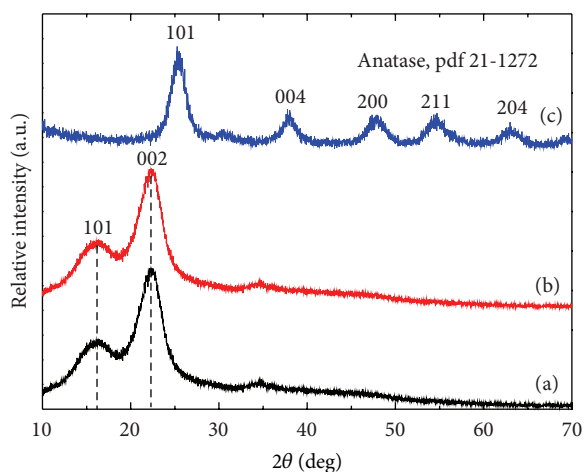


FIGURE 4: XRD patterns of (a) the original wood, (b) the wood coated by TiO_2 sol, and (c) wood-templated TiO_2 .

for the calcined sample, which indicated the formation of new crystal structures of the calcined wood sample. As shown in pattern of wood-templated TiO_2 , the diffraction peaks at 25° , 38° , 48° , and 54° could be assigned to the diffractions of the (101), (004), (200), and (211) planes of anatase TiO_2 (JCPDS number 21-1272) [36, 40], respectively. XRD pattern of the wood-templated TiO_2 also confirmed that the components of the pristine wood were completely got rid of through the calcination process.

TEM images in Figure 5(a) revealed a much more fine structure of the obtained TiO_2 sintered at 550°C for 3 h. Though TiO_2 sample has been pulverized, the slices were found in the TEM image, just like the cellular framework of the original wood. Consequently, we could safely conclude that the cellular structure of the original wood has been preserved after the calcination process. The selected area electron diffraction (SAED) of the slice in Figure 5(b) illuminated the crystalline phase of the wood-templated TiO_2 is polycrystalline with the coexistence of the diffraction rings and spots at the SAED pattern. The HRTEM image in Figure 5(c) revealed that the distance between the adjacent lattice fringes of (101) planes is about 0.352 nm which

is corresponding to the anatase TiO_2 crystal ($a = 0.325$ nm, $c = 0.521$ nm).

The photocatalytic ability of the obtained cellular-structured TiO_2 was investigated by decomposing RhB dye, a very difficult degradable and highly toxic organic pollutant. The photodegradation curves of RhB were exhibited in Figure 6. The wood-templated TiO_2 could photodegrade the RhB under UV light irradiation. The original wood shown in Figure 6(a) had a little photocatalytic activity of about 4.6% on RhB. It was mainly ascribed to the physical absorption effect because of porous wood. In Figure 6(b), the wood coated by TiO_2 sol showed a photocatalytic activity of about 8.21% on RhB. However, wood-templated TiO_2 expressed a superior photocatalytic activity of about 92.5% on RhB (Figure 6(c)). The photocatalytic efficiency of the obtained TiO_2 was greatly enhanced probably, since the prepared TiO_2 remained the original wood cellular structures. The original wood porous structure could be affording a portable carrier for absorbing and degrading much organic pollutants.

Meanwhile, the photocatalytic activity of wood-templated TiO_2 was compared to the commercially available TiO_2 P25 (Degussa, Germany) that consist of both anatase (80%) and rutile (20%) phases of TiO_2 . The same experimental conditions were selected for P25. From the comparison between catalysts wood-templated TiO_2 and P25 (Figure 6(d)), it can be seen that RhB underwent decomposition of a little faster in the case of the latter catalyst. But the problem with the P25 powder is that the TiO_2 disperses in water forming a white colloidal solution, and it is difficult to separate from the reaction mixture for reuse. The separation performance test showed that the wood-templated TiO_2 has a good sedimentation ability and can decant from the suspension in about 15 min, while the P25 do not decant after 45 min.

4. Conclusions

In the present paper, the anatase wood-templated TiO_2 was successfully fabricated by using a facile dip-coating and subsequent calcination process. The as-prepared TiO_2 possessed the typical cellular structure with unbroken vessels and uniformly arranged wood fibers. Also, this wood-templated TiO_2 presented a superior photocatalytic degradation of RhB.

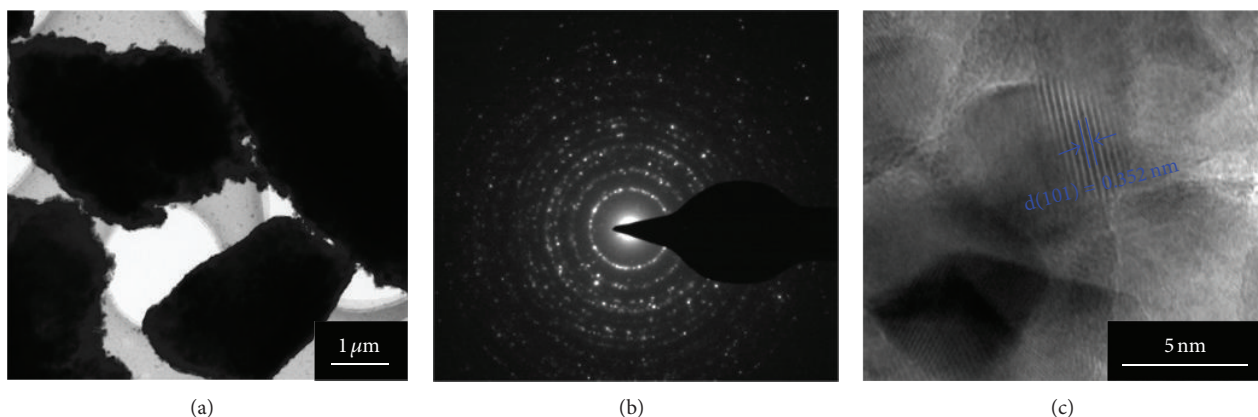


FIGURE 5: (a) TEM images, (b) the selected electron diffraction patterns, and (c) HRTEM images of the wood-templated TiO_2 .

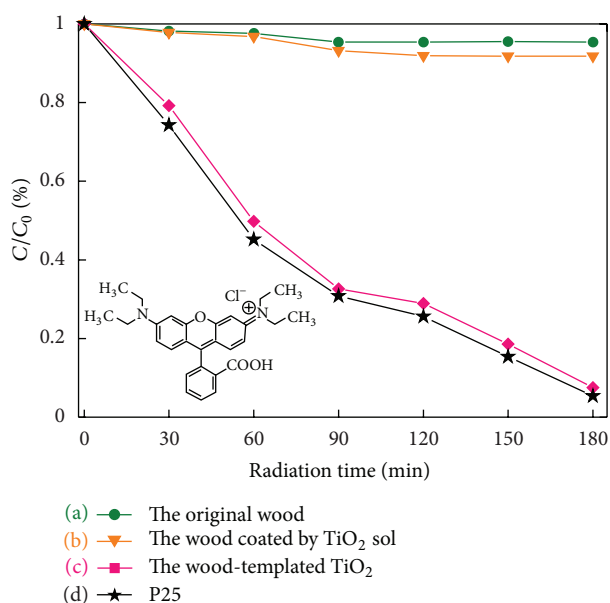


FIGURE 6: Photocatalytic activity of (a) the original wood, (b) the wood coated by TiO_2 sol, (c) the wood-templated TiO_2 , and (d) P25, respectively.

This paper probably provided another way for fabricating inorganic materials using the natural wood as template.

Acknowledgments

This work was financially supported by The National Natural Science Foundation of China (Grant nos. 31270590 and 21207073) and National Basic Research Program of China (973 Program, Grant no. 2009CB220000).

References

- [1] S. V. N. T. Kuchibhatla, A. S. Karakoti, D. Bera, and S. Seal, "One dimensional nanostructured materials," *Progress in Materials Science*, vol. 52, no. 5, pp. 699–913, 2007.
- [2] J. Li, Q. Xu, J. Wang, J. Jiao, and Z. Zhang, "Controlled synthesis of monolithic hierarchical porous materials using wood as a template with assistance of supercritical carbon dioxide," *Industrial and Engineering Chemistry Research*, vol. 47, no. 20, pp. 7680–7685, 2008.
- [3] O. Paris, I. Burgert, and P. Fratzl, "Biomimetics and biotemplating of natural materials," *MRS Bulletin*, vol. 35, no. 3, pp. 219–225, 2010.
- [4] H. Zhou, T. Fan, and D. Zhang, "Biotemplated materials for sustainable energy and environment: current status and challenges," *ChemSusChem*, vol. 4, no. 10, pp. 1344–1387, 2011.
- [5] L. Huang, Z. Wang, J. Sun et al., "Fabrication of ordered porous structures by self-assembly of zeolite nanocrystals," *Journal of the American Chemical Society*, vol. 122, no. 14, pp. 3530–3531, 2000.
- [6] Y. J. Lee, J. S. Lee, Y. S. Park, and K. B. Yoon, "Synthesis of large monolithic zeolite foams with variable macropore architectures," *Advanced Materials*, vol. 13, no. 16, pp. 1259–1263, 2001.
- [7] L. Tosheva, B. Mihailova, V. Valtchev, and J. Sterte, "Zeolite beta spheres," *Microporous and Mesoporous Materials*, vol. 48, no. 1–3, pp. 31–37, 2001.
- [8] Y. J. Wang, Y. Tang, X. D. Wang, W. L. Yang, and Z. Gao, "Fabrication of hollow zeolite fibers through layer-by-layer adsorption method," *Chemistry Letters*, no. 11, pp. 1344–1345, 2000.
- [9] S. A. Davis, S. L. Burkett, N. H. Mendelson, and S. Mann, "Bacterial templating of ordered macrostructures in silica and silica-surfactant mesophases," *Nature*, vol. 385, no. 6615, pp. 420–423, 1997.
- [10] G. Cook, P. L. Timms, and C. Göltner-Spickermann, "Exact replication of biological structures by chemical vapor deposition of silica," *Angewandte Chemie—International Edition*, vol. 42, no. 5, pp. 557–559, 2003.
- [11] H. Imai, M. Matsuta, K. Shimizu, H. Hirashima, and N. Negishi, "Preparation of TiO_2 fibers with well-organized structures," *Journal of Materials Chemistry*, vol. 10, no. 9, pp. 2005–2006, 2000.
- [12] M. W. Anderson, S. M. Holmes, N. Hanif, and C. S. Cundy, "Hierarchical pore structures through diatom zeolitization," *Angewandte Chemie—International Edition*, vol. 39, no. 15, pp. 2707–2710, 2000.

- [13] Y. Kim, "Small structures fabricated using ash-forming biological materials as templates," *Biomacromolecules*, vol. 4, no. 4, pp. 908–913, 2003.
- [14] S. Chia, J. Urano, F. Tamanoi, B. Dunn, and J. I. Zink, "Patterned hexagonal arrays of living cells in sol-gel silica films," *Journal of the American Chemical Society*, vol. 122, no. 27, pp. 6488–6489, 2000.
- [15] A. N. Shigapov, G. W. Graham, R. W. McCabe, and H. K. Plummer Jr., "The preparation of high-surface area, thermally-stable, metal-oxide catalysts and supports by a cellulose templating approach," *Applied Catalysis A*, vol. 210, no. 1-2, pp. 287–300, 2001.
- [16] S. R. Hall, H. Bolger, and S. Mann, "Morphosynthesis of complex inorganic forms using pollen grain templates," *Chemical Communications*, vol. 9, no. 22, pp. 2784–2785, 2003.
- [17] D. Yang, L. Qi, and J. Ma, "Eggshell membrane templating of hierarchically ordered macroporous networks composed of TiO_2 tubes," *Advanced Materials*, vol. 14, no. 21, pp. 1543–1546, 2002.
- [18] F. C. Meldrum and R. Seshadri, "Porous gold structures through templating by echinoid skeletal plates," *Chemical Communications*, no. 1, pp. 29–30, 2000.
- [19] T. Ota, M. Imaeda, H. Takase et al., "Porous titania ceramic prepared by mimicking silicified wood," *Journal of the American Ceramic Society*, vol. 83, no. 6, pp. 1521–1523, 2000.
- [20] A. Dong, Y. Wang, Y. Tang et al., "Zeolitic tissue through wood cell templating," *Advanced Materials*, vol. 14, no. 12, pp. 926–929, 2002.
- [21] Z. Liu, T. Fan, W. Zhang, and D. Zhang, "The synthesis of hierarchical porous iron oxide with wood templates," *Microporous and Mesoporous Materials*, vol. 85, no. 1-2, pp. 85–88, 2005.
- [22] Z. Liu, T. Fan, and D. Zhang, "Synthesis of biomorphous nickel oxide from a pinewood template and investigation on a hierarchical porous structure," *Journal of the American Ceramic Society*, vol. 89, no. 2, pp. 662–665, 2006.
- [23] Z. Liu, T. Fan, D. Zhang, X. Gong, and J. Xu, "Hierarchically porous ZnO with high sensitivity and selectivity to H_2S derived from biotemplates," *Sensors and Actuators B*, vol. 136, no. 2, pp. 499–509, 2009.
- [24] Z. Liu, T. Fan, J. Ding, D. Zhang, Q. Guo, and H. Ogawa, "Synthesis and cathodoluminescence properties of porous wood (fir)-templated zinc oxide," *Ceramics International*, vol. 34, no. 1, pp. 69–74, 2008.
- [25] J. Li, Y. Lu, D. Yang, Q. Sun, Y. Liu, and H. Zhao, "Lignocellulose aerogel from wood-ionic liquid solution (1-allyl-3-methylimidazolium chloride) under freezing and thawing conditions," *Biomacromolecules*, vol. 12, no. 5, pp. 1860–1867, 2011.
- [26] Y. Lu, Q. Sun, D. Yang et al., "Fabrication of mesoporous lignocellulose aerogels from wood via cyclic liquid nitrogen freezing-thawing in ionic liquid solution," *Journal of Materials Chemistry*, vol. 22, no. 27, pp. 13548–13557, 2012.
- [27] J. M. Qian, J. P. Wang, and Z. H. Jin, "Preparation and properties of porous microcellular SiC ceramics by reactive infiltration of Si vapor into carbonized basswood," *Materials Chemistry and Physics*, vol. 82, no. 3, pp. 648–653, 2003.
- [28] P. Greil, T. Lifka, and A. Kaindl, "Biomorphic cellular silicon carbide ceramics from wood—I: processing and microstructure," *Journal of the European Ceramic Society*, vol. 18, no. 14, pp. 1961–1973, 1998.
- [29] B. Sun, T. Fan, and D. Zhang, "Porous TiC ceramics derived from wood template," *Journal of Porous Materials*, vol. 9, no. 4, pp. 275–277, 2002.
- [30] J. Huang and T. Kunitake, "Nano-precision replication of natural cellulosic substances by metal oxides," *Journal of the American Chemical Society*, vol. 125, no. 39, pp. 11834–11835, 2003.
- [31] C. R. Rambo and H. Sieber, "Novel synthetic route to biomorphic Al_2O_3 ceramics," *Advanced Materials*, vol. 17, no. 8, pp. 1088–1091, 2005.
- [32] T. Fan, X. Li, Z. Liu, J. Gu, D. Zhang, and Q. Guo, "Microstructure and infrared absorption of biomorphic chromium oxides templated by wood tissues," *Journal of the American Ceramic Society*, vol. 89, no. 11, pp. 3511–3515, 2006.
- [33] M. Anpo and M. Takeuchi, "Design and development of second-generation titanium oxide photocatalysts to better our environment—approaches in realizing the use of visible light," *International Journal of Photoenergy*, vol. 3, no. 2, pp. 89–94, 2001.
- [34] A. D. Paola, S. Ikeda, G. Marci, B. Ohtani, and L. Palmisano, "Transition metal doped TiO_2 : physical properties and photocatalytic behaviour," *International Journal of Photoenergy*, vol. 3, no. 4, pp. 171–176, 2001.
- [35] C. C. Hu, T. C. Hsu, and L. H. Kao, "One-step cohydrothermal synthesis of nitrogen-doped titanium oxide nanotubes with enhanced visible light photocatalytic activity," *International Journal of Photoenergy*, vol. 2012, Article ID 391958, 9 pages, 2012.
- [36] X. Chen and S. S. Mao, "Titanium dioxide nanomaterials: synthesis, properties, modifications and applications," *Chemical Reviews*, vol. 107, no. 7, pp. 2891–2959, 2007.
- [37] N. Al Dahoudi, Q. Zhang, and G. Cao, "Alumina and hafnia ad layers for a niobium-doped titanium oxide photoanode," *International Journal of Photoenergy*, vol. 2012, Article ID 401393, 6 pages, 2012.
- [38] V. K. Sharma, K. Winkelmann, Y. Krasnova, C. Lee, and M. Sohn, "Heterogeneous photocatalytic reduction of ferrate(VI) in UV-irradiated titania suspensions: role in enhancing destruction of nitrogen-containing pollutants," *International Journal of Photoenergy*, vol. 5, no. 3, pp. 183–190, 2003.
- [39] D. J. Yang, Z. F. Zheng, H. Y. Zhu, H. W. Liu, and X. P. Gao, "Titanate nanofibers as intelligent absorbents for the removal of radioactive ions from water," *Advanced Materials*, vol. 20, no. 14, pp. 2777–2781, 2008.
- [40] D. Yang, H. Liu, Z. Zheng et al., "An efficient photocatalyst structure: $\text{TiO}_2(\text{B})$ nanofibers with a shell of anatase nanocrystals," *Journal of the American Chemical Society*, vol. 131, no. 49, pp. 17885–17893, 2009.
- [41] D. Yang, C. Chen, Z. Zheng et al., "Grafting silica species on anatase surface for visible light photocatalytic activity," *Energy and Environmental Science*, vol. 4, no. 6, pp. 2279–2287, 2011.
- [42] D. Yang, S. Sarina, H. Zhu et al., "Capture of radioactive cesium and iodide ions from water by using titanate nanofibers and nanotubes," *Angewandte Chemie—International Edition*, vol. 50, no. 45, pp. 10594–10598, 2011.
- [43] H. Yang, S. Zhu, and N. Pan, "Studying the mechanisms of titanium dioxide as ultraviolet-blocking additive for films and fabrics by an improved scheme," *Journal of Applied Polymer Science*, vol. 92, no. 5, pp. 3201–3210, 2004.

Research Article

Preparation of Nanostructured Cu_2SnS_3 Photocatalysts by Solvothermal Method

Qingyun Chen and Di Ma

State Key Laboratory of Multiphase Flow in Power Engineering, School of Energy and Power Engineering, Xi'an Jiaotong University, Xi'an 710049, China

Correspondence should be addressed to Qingyun Chen; qychen@mail.xjtu.edu.cn

Received 18 January 2013; Accepted 20 February 2013

Academic Editor: Krisztina Gajda-Schranz

Copyright © 2013 Q. Chen and D. Ma. This is an open access article distributed under the Creative Commons Attribution License, which permits unrestricted use, distribution, and reproduction in any medium, provided the original work is properly cited.

Nanostructured Cu-Sn-S powder was prepared by a relatively low-cost, simple, and green solvothermal method. Flower-like Cu_2SnS_3 nanostructures were successfully synthesized in 50 vol% ethanol water solution at 200 °C for 7.5 h. The structure and photophysical properties of the as-obtained samples were characterized by scanning electron microscopy, transmission electron microscopy, X-ray diffraction, and UV-Vis diffusion reflectance spectroscopy. Results showed that the cubic and tetragonal Cu_2SnS_3 was obtained by varying the ethanol contents. The band-gap energy of tetragonal Cu_2SnS_3 nanocrystals is near the optimum for photovoltaic solar conversion in a single band-gap device.

1. Introduction

With the energy crisis and environment problems becoming more and more serious, it is very urgent to explore new energy resource [1]. Solar energy is a promising new energy resource which is clean and sustainable. Cu-Sn-S, an important category of I-IV-VI chalcogenides functional materials, has attracted great attention because of their promising photocatalytic activity, photovoltaic property, nonlinear optical property, and outstanding optical-thermomechanical properties [2, 3]. Traditionally, these chalcogenides were prepared by solid-state reaction [4], which required high temperature, inert atmosphere protection, and a relatively long duration. Cu_4SnS_4 could be prepared by heating the starting materials of copper sheet, tin particles and sulfur powders at 900–1200 °C for 72 h in a silica tube [5]. Cu_2SnS_3 was obtained through a solid-state reaction by heating Cu_2S and SnS_2 at 900 °C for 48 h [6]. Similarly, Bouaziz et al. have synthesized Cu_2SnS_3 film through a solid-state reaction under vapor sulphur pressure at 530 °C for 6 h by using a sequentially deposited copper and tin [7]. Recently, solvothermal method has been used to prepare chalcogenides functional materials. Cu_2SnS_3 nanorods could be prepared by solvothermal reaction of Cu, Sn, S powders in the temperature range of 250–300 °C for 10–12 h [8]. Qu et al. [9] synthesized mesoporous

Cu_2SnS_3 spheres composed of nanoparticles via solvothermal route by using $\text{SnCl}_4 \cdot 5\text{H}_2\text{O}$, CuCl, thiourea as raw materials, PEG-1000 as surfactants, and ethanol as solvent. Qu et al. [10] also employed $\text{SnCl}_4 \cdot 5\text{H}_2\text{O}$, $\text{CuCl}_2 \cdot 2\text{H}_2\text{O}$ as metal precursor, thioacetamide as sulfur source, and PEG-200 as surfactants and successfully synthesized cabbage-like Cu_2SnS_3 nanostructures.

Therefore, we dedicated to develop a low-cost, facile, and environmental-friendly solvothermal method to synthesize I-IV-VI chalcogenides. Cu_2SnS_3 nanostructures were prepared by varying solvents with different ethanol content through solvothermal method. $\text{CuCl}_2 \cdot 2\text{H}_2\text{O}$, $\text{SnCl}_4 \cdot 5\text{H}_2\text{O}$, and thioacetamide (TAA) were used as raw materials. Both the cubic and tetragonal Cu_2SnS_3 were obtained by varying ethanol content. The crystal structure, morphology, and photocatalytic property were also characterized.

2. Experimental

2.1. Preparation. All chemicals are analytical grade and used without further purification. Water is deionized water. A series of Cu_2SnS_3 were synthesized by the following process. 0.003 mol $\text{SnCl}_4 \cdot 5\text{H}_2\text{O}$ and 0.006 mol $\text{CuCl}_2 \cdot 2\text{H}_2\text{O}$ were dissolved in 50 mL deionized water containing different

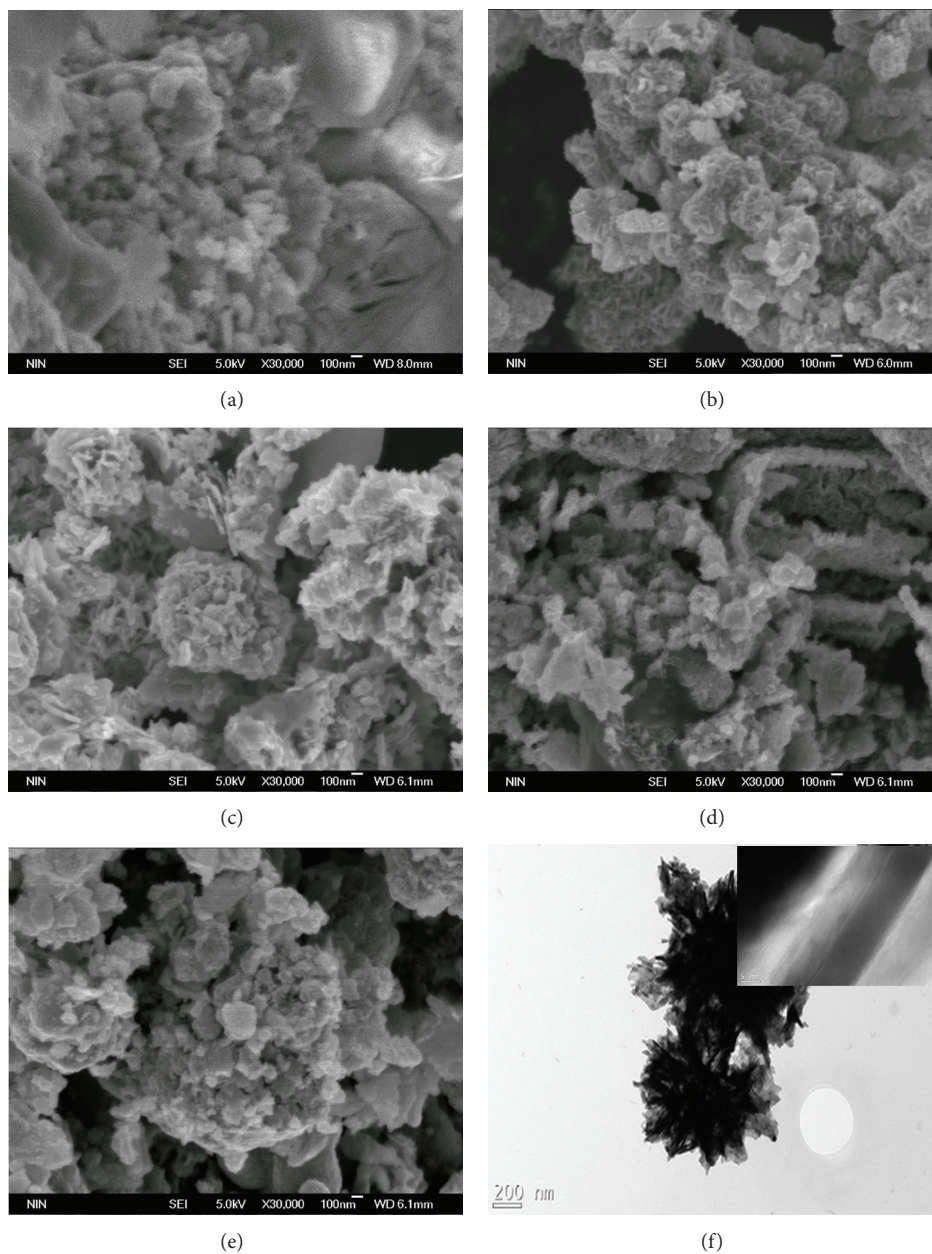


FIGURE 1: SEM images of the obtained samples at 200°C for 7.5 h as the function of different ethanol contents: (a) 100% H₂O, (b) 25% CH₃CH₂OH, (c) 50% CH₃CH₂OH, (d) 75% CH₃CH₂OH, and (e) 100% CH₃CH₂OH; (f) TEM image of sample from 50% CH₃CH₂OH (inset is TEM image of nanoflake).

concentrations of ethanol (0 vol%, 25 vol%, 50 vol%, 75 vol%, and 100 vol%) under magnetic stirring until they were dissolved completely. TAA was added and the mixture was transferred into a Teflon-lined stainless steel autoclave and sealed. The autoclave was maintained at different temperatures (180–220°C) for various durations (5.5–12.5 h) and then cooled down to room temperature. The precipitate was centrifuged and washed by deionized water and absolute ethanol for several times and finally vacuum-dried at 90°C for 5 h.

2.2. Characterization. The X-ray diffraction (XRD) patterns were recorded by a PANalytical X'pert Pro X-ray diffractometer equipped with CuK α irradiation at a scan rate of 0.02° s⁻¹. The accelerating voltage and the applied current were 40 kV and 40 mA, respectively. The morphology and microstructure of the samples were determined by field emission scanning electron microscope (SEM, JEOL JSM-6700F) and transmission electron microscope (TEM, JEM-2100). The UV-Vis absorption spectra were measured by a HITACHI UV4100 spectrometer, with the scanning range

from 100 nm to 800 nm. Raman scattering spectra were recorded on JobinYvon LabRAM HR800 spectrometer using 514.5 nm irradiation from an argon ion laser at 20 mW.

3. Results and Discussion

Figure 1 shows the SEM images of the as-obtained samples as the function of the different ethanol contents. Obviously, the morphology of the as-obtained samples is notably influenced by the solvents. When 25 vol% ethanol is employed, the morphology of the obtained samples consists of large quantities of flower-like nanocrystals as shown in Figure 1(b). As the ethanol content increases to 50 vol%, the flower-like Cu_2SnS_3 nanocrystals with the diameter of about 0.5–1 μm become bigger comparing Figure 1(a) with Figure 1(b). The Cu_2SnS_3 flowers are constructed by aggregation of large-scale thinner nanoflakes (Figure 1(f)) with the thickness of c.a. 15 nm (inset in Figure 1(f)). When the ethanol content increases more, the flower-like structure is broken and the as-obtained samples are not uniform in shape and microstructure as shown in Figures 1(d) and 1(e). It seems that the solvent plays a critical role in the process of preparing shape and crystallinity controllable Cu_2SnS_3 nanocrystals.

The XRD patterns of the as-obtained samples are shown in Figure 2. It is obvious that the ethanol content has a great effect on the crystallographic structure. The major XRD diffraction peaks that appeared at $2\theta = 28.5^\circ, 33.0^\circ, 47.6^\circ, 51.7^\circ,$ and 56.6° can be attributed to (112), (200), (220), (312), and (224) planes of Cu_2SnS_3 (JCPDS no. 89-4714), which is in good agreement with the standard data for the phase of the tetragonal Cu_2SnS_3 structure [11]. When the ethanol content is lower than 50 vol%, there appear some diffraction peaks which do not belong to the phase of Cu_2SnS_3 structure. The diffraction peaks of that synthesized in 50 vol% ethanol solution are the strongest, which indicates its highest crystallinity. In Particular, no obvious peaks attributable to other impurities are detected, confirming that the obtained sample is composed of pure tetragonal Cu_2SnS_3 structure. With the ethanol content increasing, the crystal phase of Cu_2SnS_3 changes. And the peaks corresponding to (111), (200), (220), (311), and (222) crystal planes appear, which match with the standard data for the pure phase of the cubic Cu_2SnS_3 structure according JCPDS no. 89-2877 [9]. It shows that the cubic Cu_2SnS_3 structure can be obtained when 100% ethanol was used as the solvent, but the crystalline structures are not as good as those of the tetragonal Cu_2SnS_3 structure because of the broaden diffraction peaks. In order to confirm the preparation of the pure tetragonal Cu_2SnS_3 , the Raman analysis is performed and the results are shown in Figure 3. Figure 3 is the Raman spectrum of the as-obtained Cu_2SnS_3 prepared in 50 vol% ethanol water solution at 200°C for 7.5 h. There are two peaks around 338 cm^{-1} and 298 cm^{-1} which are assigned to the tetragonal Cu_2SnS_3 [12]. Therefore, the pure tetragonal Cu_2SnS_3 with good crystallinity can be synthesized by the 50 vol% ethanol solvothermal method.

The reaction temperature and time are the other important parameters for the solvothermal method. The effect of the solvothermal temperature on the crystalline structures of

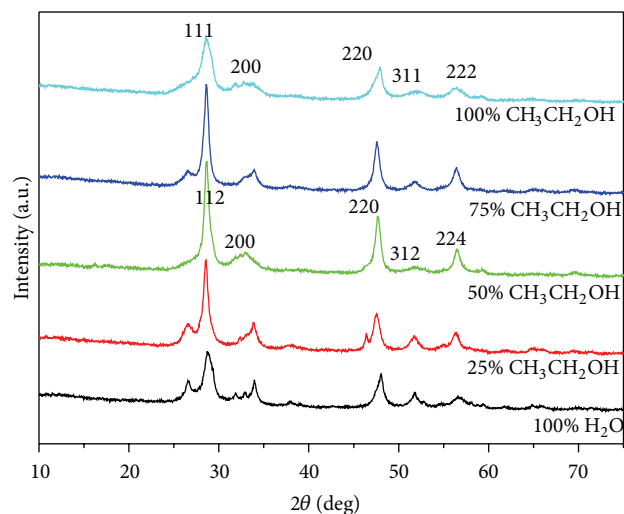


FIGURE 2: XRD spectra of the obtained samples at 200°C for 7.5 h as the function of different ethanol contents.

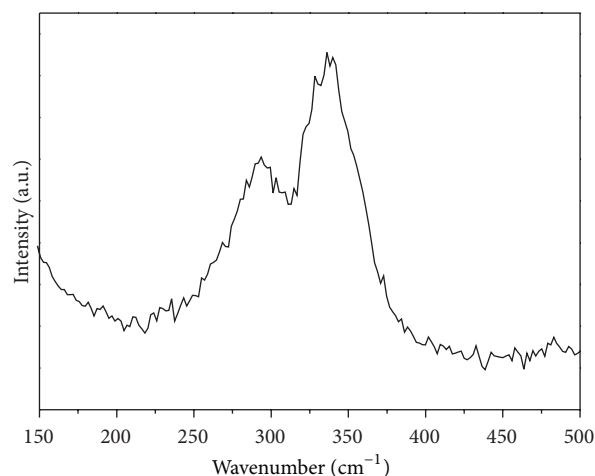


FIGURE 3: Raman spectrum of the obtained samples at 200°C for 7.5 h with 50 vol% ethanol.

Cu_2SnS_3 is investigated by fixing the reaction time of 7.5 h and the result is shown in Figure 4. As shown in Figure 4, the diffraction peaks of Cu_2SnS_3 prepared at 200°C match well with pure tetragonal Cu_2SnS_3 , and the peaks intensity of them is higher and sharper than that of those prepared at 180°C and 220°C . When the temperature increases to 220°C , many other peaks appear in the XRD patterns which imply the production of impurities. Then the best reaction temperature would be 200°C . Figure 5 shows XRD patterns of the as-obtained samples at 200°C for different reaction times. It is obvious that XRD intensity for pure Cu_2SnS_3 structure by treating 7.5 h is the strongest. Then we can conclude that the conditions for pure tetragonal Cu_2SnS_3 preparation by solvothermal method are 200°C for 7.5 h with 50 vol% ethanol in this study.

The optical band gap of the as-obtained tetragonal Cu_2SnS_3 nanocrystals can be evaluated from the UV-Vis

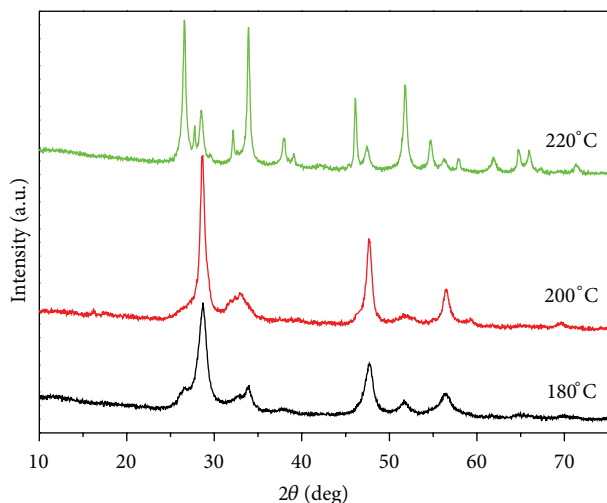


FIGURE 4: XRD spectra of the obtained samples for 7.5 h at the different temperatures.

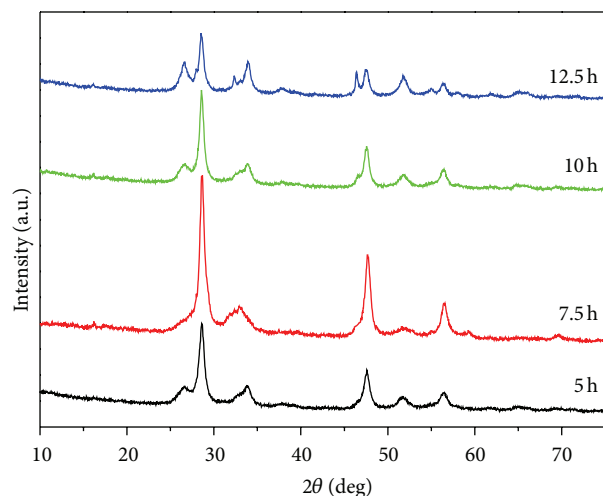


FIGURE 5: XRD spectra of the obtained samples at 200°C for the different reaction times.

absorption spectrum. Figure 6 shows the absorption spectrum of Cu_2SnS_3 prepared at 200°C for 7.5 h. From Figure 6, it can be seen that the as-obtained tetragonal Cu_2SnS_3 has broad absorption in the entire visible light region, and the absorption edge of about 872 nm is estimated from the intercept by extrapolating straight line to the horizontal axis. The band gap is calculated to be about 1.42 eV through the formula: E_g (eV) = 1240/ λ (λ = 872 nm). Obviously, the band gap of tetragonal Cu_2SnS_3 nanocrystals is near the optimum for photovoltaic solar conversion in a single band-gap device.

4. Conclusion

In this study, Cu_2SnS_3 nanocrystals were prepared through an environmental-friendly facile solvothermal method. It was found that the crystal structure and morphology of

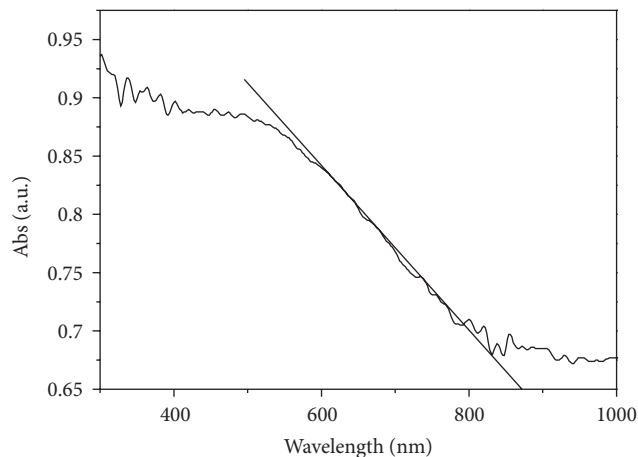


FIGURE 6: UV-Visible absorption spectrum of the obtained samples at 200°C for 7.5 h.

the productions were strongly influenced by the reaction conditions including solvents, temperature, and time. It is noticeable that the choice of ethanol water solution as solvents, which is a common, nontoxic, and low-cost solvent whose advantages are beneficial to sustainable development, is a key to successfully synthesize tetragonal Cu_2SnS_3 . The pure tetragonal Cu_2SnS_3 nanocrystals were prepared in 50 vol% ethanol solution at 200°C for 7.5 h, and the band gap is about 1.42 eV which is suitable to be solar cells materials.

Acknowledgments

This work was financially supported by the National Basic Research Program of China (2009CB220000), the Research Fund for the Doctoral Program of Higher Education of China (20110201120042), and the Natural Science foundation of China (21206133).

References

- [1] X. B. Chen, S. H. Shen, L. J. Guo, and S. S. Mao, "Semiconductor-based photocatalytic hydrogen generation," *Chemical Reviews*, vol. 11, pp. 6503–6570, 2010.
- [2] B. Li, Y. Xie, J. X. Huang, and Y. T. Qian, "Synthesis, characterization, and properties of nanocrystalline Cu_2SnS_3 ," *Journal of Solid State Chemistry*, vol. 153, pp. 170–173, 2000.
- [3] C. Wu, Z. Hu, C. Wang, H. Sheng, J. Yang, and Y. Xie, "Hexagonal Cu_2SnS_3 with metallic character: another category of conducting sulfides," *Applied Physics Letters*, vol. 91, no. 14, Article ID 143104, 3 pages, 2007.
- [4] Y. Xiong, Y. Xie, G. Du, and H. Su, "From 2D framework to quasi-1D nanomaterial: preparation, characterization, and formation mechanism of Cu_3SnS_4 nanorods," *Inorganic Chemistry*, vol. 41, no. 11, pp. 2953–2959, 2002.
- [5] M. Hasaka, T. Aki, T. Morimura, and S. I. Kondo, "Thermoelectric properties of Cu-Sn-S," *Energy Conversion and Management*, vol. 38, no. 9, pp. 855–859, 1997.
- [6] M. Onoda, X. A. Chen, A. Sato, and H. Wada, "Crystal structure and twinning of monoclinic Cu_2SnS_3 ," *Materials Research Bulletin*, vol. 35, pp. 1563–1570, 2000.

- [7] M. Bouaziz, M. Amlouk, and S. Belgacem, "Structural and optical properties of Cu_2SnS_3 sprayed thin films," *Thin Solid Films*, vol. 517, no. 7, pp. 2527–2530, 2009.
- [8] X. Chen, X. Wang, C. An, J. Liu, and Y. Qian, "Preparation and characterization of ternary Cu-Sn-E (E = S, Se) semiconductor nanocrystallites via a solvothermal element reaction route," *Journal of Crystal Growth*, vol. 256, no. 3-4, pp. 368–376, 2003.
- [9] B. H. Qu, M. Zhang, D. N. Lei et al., "Facile solvothermal synthesis of mesoporous Cu_2SnS_3 spheres and their application in lithium-ion batteries," *Nanoscale*, vol. 3, no. 9, pp. 3646–3651, 2011.
- [10] B. H. Qu, H. X. Li, M. Zhang, L. Mei, L. B. Chen, and Y. G. Wang, "Ternary Cu_2SnS_3 cabbage-like nanostructures: large-scale synthesis and their application in Li-ion batteries with superior reversible capacity," *Nanoscale*, vol. 3, pp. 4389–4393, 2011.
- [11] P. A. Fernandes, P. M. P. Salomé, and A. F. da Cunha, "Study of ternary Cu_2SnS_3 and Cu_3SnS_4 thin films prepared by sulfurizing stacked metal precursors," *Journal of Physics D: Applied Physics*, vol. 43, no. 21, Article ID 215403, 2010.
- [12] P. A. Fernandes, P. M. P. Salomé, and A. F. da Cunha, "Study of polycrystalline $\text{Cu}_2\text{ZnSnS}_4$ films by Raman scattering," *Journal of Alloys and Compounds*, vol. 509, no. 28, pp. 7600–7606, 2011.

Research Article

In Situ Measurement of Local Hydrogen Production Rate by Bubble-Evolved Recording

Xiaowei Hu, Liejin Guo, and Yechun Wang

State Key Laboratory of Multiphase Flow in Power Engineering, International Research Center for Renewable Energy, Xi'an Jiaotong University, Shaanxi 710049, China

Correspondence should be addressed to Xiaowei Hu; hu-xiaowei@mail.xjtu.edu.cn and Liejin Guo; lj-guo@mail.xjtu.edu.cn

Received 15 January 2013; Accepted 18 February 2013

Academic Editor: Krisztina Gajda-Schranz

Copyright © 2013 Xiaowei Hu et al. This is an open access article distributed under the Creative Commons Attribution License, which permits unrestricted use, distribution, and reproduction in any medium, provided the original work is properly cited.

Hydrogen visibly bubbles during photocatalytic water splitting under illumination with above-bandgap radiation, which provides a direct measurement of local gas-evolving reaction rate. In this paper, optical microscopy of superfield depth was used for recording the hydrogen bubble growth on $\text{Cd}_{0.5}\text{Zn}_{0.5}\text{S}$ photocatalyst in reaction liquid and illuminated with purple light. By analyzing change of hydrogen bubble size as a function of time, we understood that hydrogen bubble growth experienced two periods, which were inertia effect dominated period and diffusion effect dominated period, respectively. The tendency of hydrogen bubble growth was similar to that of the gas bubble in boiling, while the difference in bubble diameter and growth time magnitude was great. Meanwhile, we obtained the local hydrogen production rate on photocatalyst active site by measuring hydrogen bubble growth variation characteristics. This method makes it possible to confirm local actual hydrogen evolution rate quantitatively during photocatalytic water splitting.

1. Introduction

Hydrogen production from solar energy by splitting water directly using semiconductor material is a promising source of carbon-free energy [1]. A lot of research has been developed on the performance improvement of semiconductor material by providing active sites and structuring semiconductor surface [2–7]. But for the heterogeneous photocatalytic reaction system, many issues concerning the semiconductor-liquid interface remain unsolved, such as the nature of the active sites and confirmation for actual reaction rate and hydrogen evolution rate [8, 9].

Hydrogen visibly bubbles during water splitting process, which couples the effects of the solid-liquid interface, hydrogen transfer process, and the multiphase system. Taking water splitting of photocatalysis, for example, due to the heterogeneous system, the reactant molecules will absorb on the catalyst surface before the photocatalytic reaction starts. When the lights radiate on the catalyst, hydrogen will start to evolve. The hydrogen generated will dissolve in the liquid adjacent to the catalyst surface firstly and will gather at solid-liquid interface randomly. When the gas gathering energy is

equal to or larger than the interface-free energy, bubble will start to nucleate and grow, and then, the local concentration and supersaturation degree are both critical values. Driven by the hydrogen molecules transfer due to supersaturation degree, finally hydrogen bubble will grow to a maxim size and detach from the catalyst surface into the reaction liquid. The hydrogen will be generated continuously, and hydrogen bubble will evolve on the same site continuously during the reaction process. The investigations on hydrogen bubble evolution characteristics will help understanding the hydrogen transfer process and the effects of the solid-liquid interface and heterogeneous system, but the research on this field is almost blank.

On the other hand, the hydrogen evolution rate or the reaction rate is a key parameter during hydrogen production process [10]. However, the determination for the hydrogen evolution rate precisely is believed to be difficult. Usually, during the process of photocatalytic water splitting, the hydrogen production rate is reflected by gas chromatograph. For the photoelectrochemical water splitting, the parameter of photocurrent is analyzed as a reaction rate index. The common approach mentioned above could not analyze the nature

TABLE I: Experimental conditions in this paper.

Reaction liquid	Photocatalyst	Incident light
Na_2SO_3 (0.25 mol/L)/ Na_2S (0.35 mol/L)	$\text{Cd}_{0.5}\text{Zn}_{0.5}\text{S}$ /mass fraction 1%	Purple light

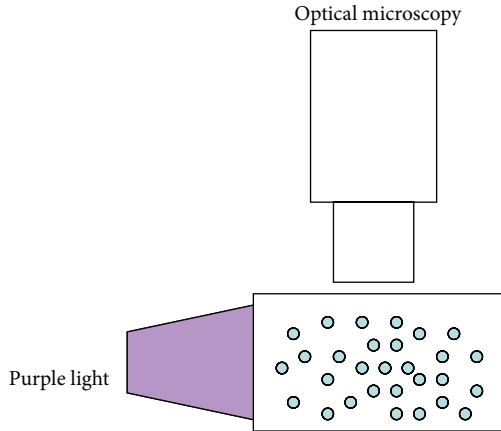


FIGURE 1: Reaction and measurement system.

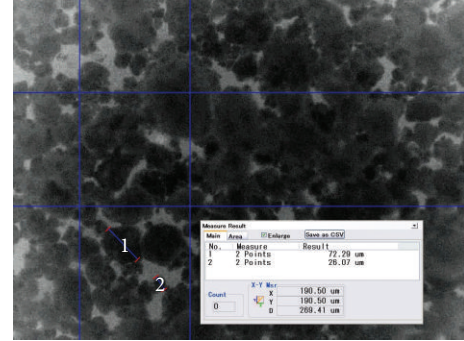
of the local active sites or the structuring surface providing only the average reaction rate. While methods based on local activity could offer a wealth of information about the surface sites important for efficient charge transfer. Examining the evolved hydrogen bubbles could provide a local measurement by recording growth rate. Additionally, measuring the bubble and the actual gas produced provides a more accurate value than that obtained by gas chromatograph or photocurrent. The straight technique of optical microscopy provides a localized measurement of the hydrogen production rate or reaction rate [9].

In this paper, the hydrogen bubble evolution process in photocatalytic reaction will be investigated. By the bubble growth recording, the research on bubble growth characteristics will be carried out, clearing the hydrogen transfer process and key affecting factors. Meanwhile, the hydrogen production rate on local active sites will be obtained and analyzed.

2. Experimental Section

In this paper, the whole experimental system was shown in Figure 1. Generally, photocatalyst, reaction liquid, and illumination conditions are the main factors affecting the reaction process. In this paper, the reaction system of $\text{Cd}_{0.5}\text{Zn}_{0.5}\text{S}$ photocatalyst which was prepared by precipitation-hydrothermal method with nanotwins [11] in reaction liquid of Na_2SO_3 (0.25 mol/L)/ Na_2S (0.35 mol/L) under the illumination of purple light was applied, as shown in Table I. On the other hand, temperature is also a key parameter during bubble evolving by affecting gas molecules movement and transfer process. Here, the operating temperature is 25°C.

Generally speaking, the high speed camera was used to record the bubble growth. But under the photocatalytic conditions, the size scale for hydrogen bubble is relatively

FIGURE 2: $\text{Cd}_{0.5}\text{Zn}_{0.5}\text{S}$ photocatalyst in liquid.

small due to the heterogeneous system of photocatalyst. The resolution radius for ordinary high speed method will not meet the requirements. In order to catch the growth process well, a microscopy photography method by Keyence/VHX-600 was used in this paper, and the catalyst distribution in reaction liquid is shown in Figure 2.

3. Results and Discussion

3.1. Hydrogen Bubble Growth Characteristics. The hydrogen generated firstly dissolves in the reaction liquid and then nucleates to form bubble when the hydrogen concentration reaches supersaturation point. Interface between catalyst and reaction liquid lowers the free energy for bubble nucleation, which is a typical heterogeneous bubble nucleation process. In the process of photocatalysis, hydrogen bubble grows continuously and finally detaches from the solid-liquid interface reaching maximum diameter.

Research on bubble growth has been carried out systematically based on the nucleate boiling phenomena [12–15]. The bubble growth process has been divided into stages with inertia effects controlled and stages with diffusion effects controlled [16]. At the initial stage, the bubble growth is driven by the pressure difference between the outside and inside of the bubble interface for its large value according to the Laplace equation. Surface tension and other inertia effects will prevent the growth, called by inertia effects controlled stage with a high bubble growth rate. With the growth of the bubble, the pressure difference between the outside and inside of the bubble interface becomes smaller, and the transfer process of gas molecules from outside to inside becomes the key factor preventing bubble growth. So the later stage is called diffusion effects controlled stage. During this stage, the bubble growth rate is relatively small.

Figure 3 shows the hydrogen bubble growth characteristics during a bubble growth period and the comparison with the bubble growth under the condition of nucleate boiling

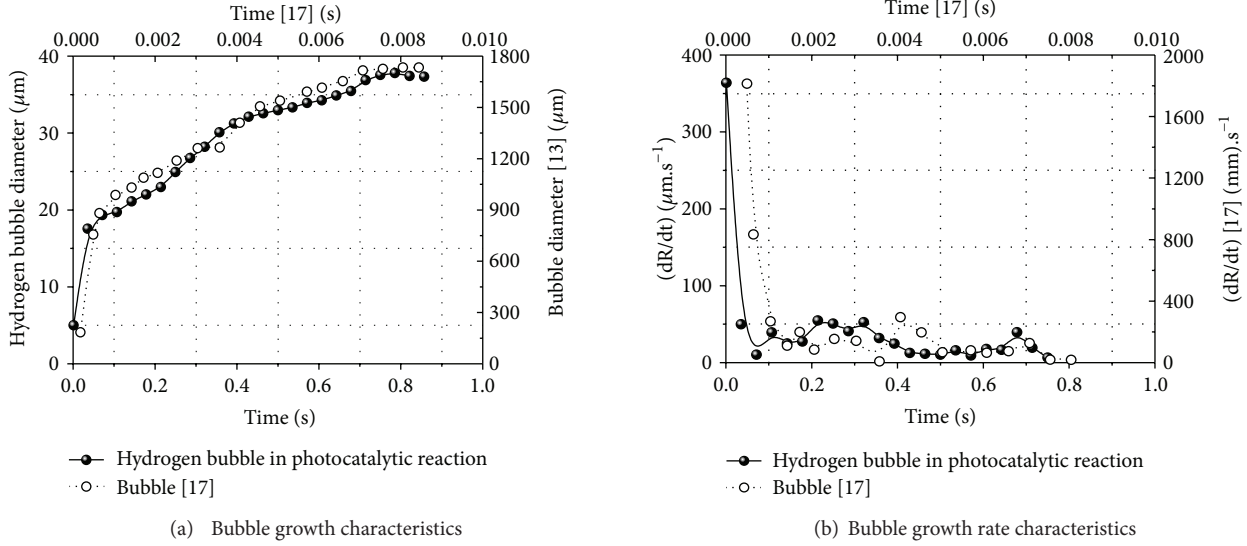


FIGURE 3: Hydrogen bubble growth characteristics during a bubble growth period and the comparison with the bubble growth under the condition of nucleate boiling.

in n-pentane liquid of $P = 760$ mmHg, $T_w - T_s = 31^\circ\text{F}$ in the literature [17]. From the figure, we can understand that the characteristics of hydrogen bubble in photocatalysis and bubble in nucleate boiling are almost consistent that the whole periods of bubble growth contain two stages with different growth rates. However, there are apparent differences between time scale and bubble size scale. Under photocatalysis condition, a whole growth period was about one second including hydrogen bubble from nucleation to detachment with max bubble diameter of 40 micrometers, while a whole growth period was about 100 milliseconds with max bubble diameter of 2 millimeters under the conditions of nucleate boiling. For the hydrogen bubble, hydrogen bubble grows rapidly to a certain size at the first stage of inertia effects controlled, and after that, the growth rapid slows down turning into the longer stage of hydrogen molecular diffusion effects controlled. Figure 4 shows a typical hydrogen bubble growth period on an active site of photocatalyst.

On the other hand, hydrogen bubble generates periodically as shown in Figure 5. After the first bubble evolution, hydrogen bubble will evolve continuously under the purple lights radiation. The period for bubble evolution can be described by nucleation time t_n and growth time t_g . Nucleation time describes the time from bubble detachment to nucleation of a new bubble, and growth time describes the time from the bubble nucleation to bubble detachment. The two parameters reflect the influences of growth process and nucleation process on the whole bubble evolution period. Generally, if $t_g/t_n > 1$, the influence of growth process is more important, which means that the effects of gas molecules transfer process are the key factors. On the contrary, the influence of nucleation process is more important, which means that the effects of supersaturation degree or reaction rate are dominated. Figure 5 indicates that the nucleation time is larger than growth time during the whole bubble

evolution period. That means that the photocatalytic reaction process driving bubble nucleation is the key factor affecting the hydrogen mass transfer process during hydrogen evolution.

3.2. Hydrogen Production Rates. Assuming for each bubble (i) an approximately spherical shape, (ii) a composition of gaseous hydrogen molecules, and (iii) a temperature equalling to the environment, according to the Laplace equation

$$P_i - P_o = \frac{2\gamma_{gl}}{R}, \quad (1)$$

and considering

$$P_i = P_{H_2}, \quad (2)$$

the number of hydrogen molecules inside the bubble can be calculated by ideal gas law

$$N_{H_2, \text{bubble}} = \frac{P_o + 2\gamma_{gl}/R}{kT} \frac{4}{3}\pi R^3, \quad (3)$$

where $P_o = 1.013 \times 10^5$ Pa is the ambient pressure, γ_{gl} is the gas-liquid surface tension, k is Boltzmann's constant, and $T = 298$ K is the ambient temperature. So we can obtain the variation of hydrogen gas in bubble with time, as shown in Figure 6.

In fact, the hydrogen produced exists in two parts: gas in bubble and gas dissolving in liquid. When the bubble starts to form, the concentration of hydrogen in liquid is supposed to reach the saturation value, achieving stable state. So, the variation of gas in bubble reflects the reaction production rate. Figure 7 shows the calculated local hydrogen production rate on an active site of photocatalyst. During the process of bubble evolution, the reaction rate was not stable, with a little

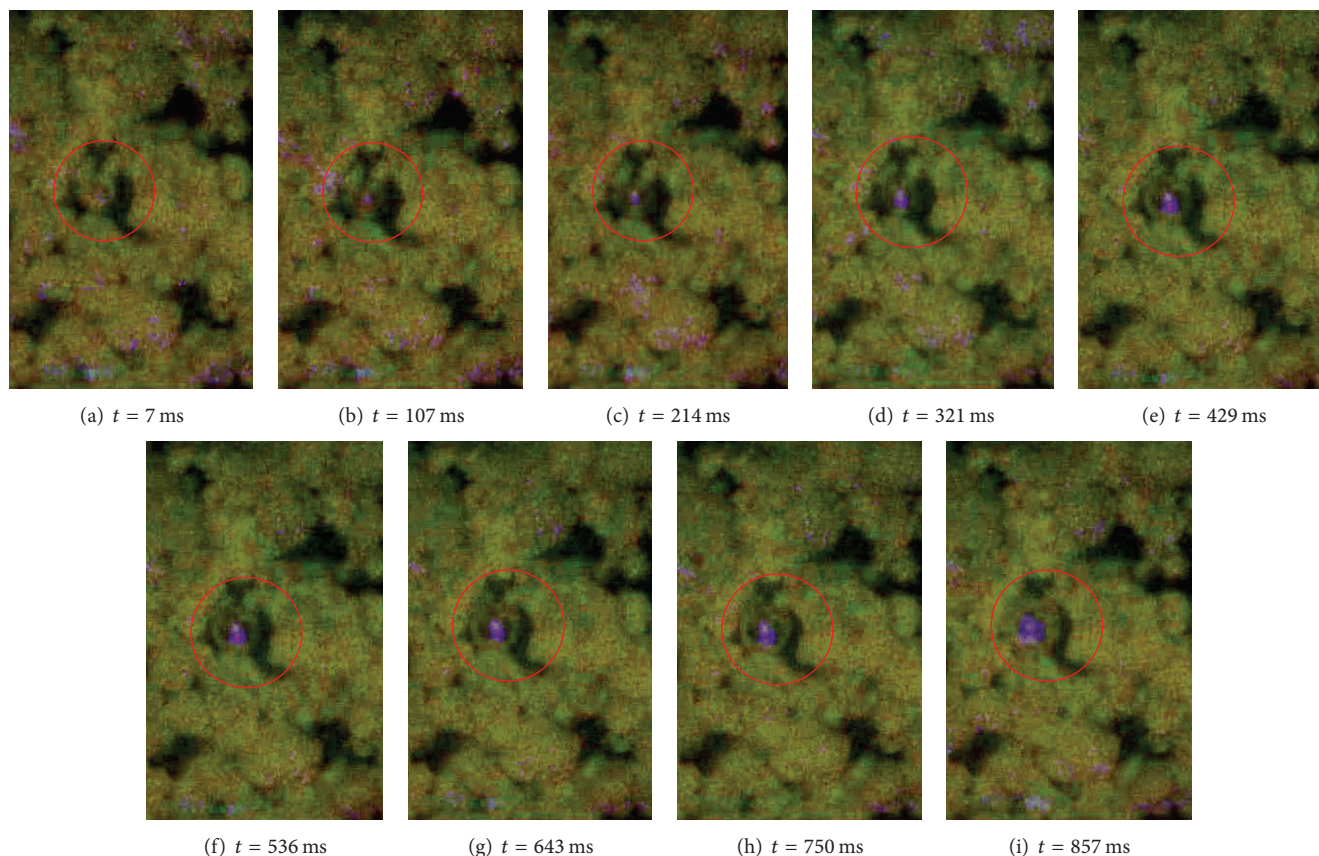


FIGURE 4: Hydrogen bubble evolution process.

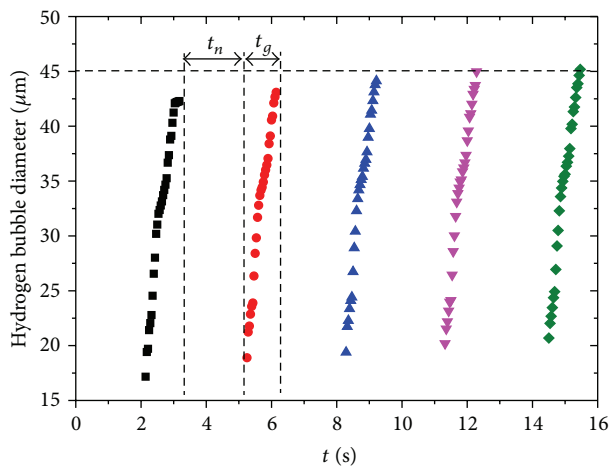


FIGURE 5: Hydrogen bubble evolution cycle on the selected site.

fluctuation, which is mostly caused by the “bubble-shadow effect.” The bubble will scatter some lights during evolution, affecting the local photon energy absorption of photocatalyst and influencing the active site performance.

Recording bubble growth during photocatalysis provides a way for local hydrogen production rate determination on a certain site. Unlike the average hydrogen production rate

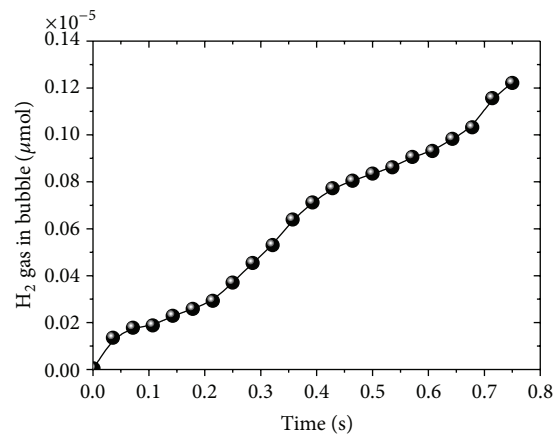


FIGURE 6: Calculated hydrogen evolution rate from gas bubble.

over some time, this local hydrogen production rate contains wealth of information about the active site and can help for understanding of the catalyst surface characteristics and its photocatalytic performance directly.

4. Conclusions

In this study, by above-bandgap light illuminating on Cd_{0.5}Zn_{0.5}S photocatalyst, evolving of individual hydrogen

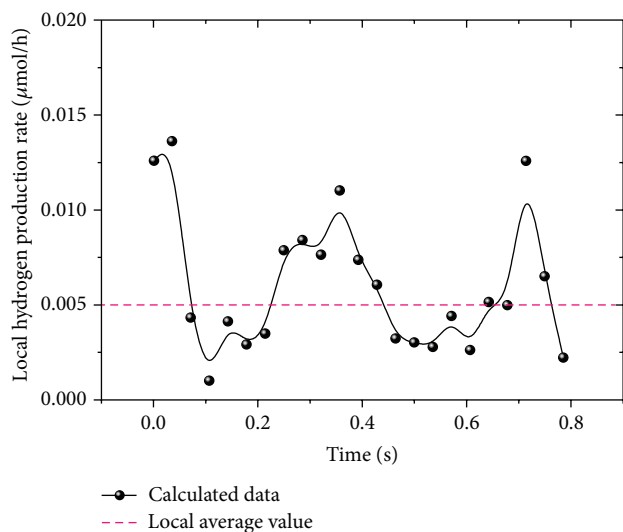


FIGURE 7: Calculated local hydrogen production rate (red dashed line indicates the average value in a bubble evolution period).

bubble, and recording of the hydrogen bubble growth, we analyzed the hydrogen bubble growth characteristics. Hydrogen bubble growth experienced two periods, which are inertia effect dominated period and diffusion effect dominated period, respectively. The tendency of hydrogen bubble growth is similar to that of the gas bubble in boiling, while the difference in bubble diameter and growth time magnitude is great. We also found that the nucleation time of hydrogen bubble was larger than the growth time, which means that the nucleation process is the key factor during the whole process of hydrogen bubble evolution.

We also provide an in situ direct and quantitative measurement of local hydrogen production rate. The variation of local hydrogen production rate indicates the effects of bubble shadow on local photon energy absorption of $\text{Cd}_{0.5}\text{Zn}_{0.5}\text{S}$ photocatalyst. The results also provide the possibility of comparing the effects of different heterogeneous catalyst or morphology on photocatalytic performance systematically.

Abbreviations

P_i :	The pressure of inside the bubble, Pa
P_{H_2} :	The pressure of hydrogen inside the bubble, Pa
P_o :	Ambient pressure, Pa
γ_{gl} :	Gas-liquid surface tension, $\text{N} \cdot \text{m}^{-1}$
R :	Bubble radius, m
$N_{\text{H}_2, \text{bubble}}$:	The number of hydrogen molecules inside the bubble
T :	Ambient temperature, K
k :	Boltzmann's constant, $1.038065 \times 10^{-23} \text{ J} \cdot \text{K}^{-1}$
t_n :	Nucleation time, s
t_g :	Growth time, s.

Conflict of Interests

The authors declare no conflict of interest.

Acknowledgments

The authors gratefully acknowledge the financial support of the National Natural Science Foundation of China (no. 51236007, no. 51121092, and no. 51102194) National Basic Research Program of China (no. 2009CB220000). One of the authors (X. Hu) was supported by the "Fundamental Research Funds for the Central Universities."

References

- [1] J. Nowotny, C. C. Sorrell, L. R. Sheppard, and T. Bak, "Solar-hydrogen: environmentally safe fuel for the future," *International Journal of Hydrogen Energy*, vol. 30, no. 5, pp. 521–544, 2005.
- [2] Z. G. Zou, J. H. Ye, K. Sayama, and H. Arakawa, "Direct splitting of water under visible light irradiation with an oxide semiconductor photocatalyst," *Nature*, vol. 414, no. 6864, pp. 625–627, 2001.
- [3] S. U. M. Khan, M. Al-Shahry, and W. B. Ingler, "Efficient photochemical water splitting by a chemically modified n-TiO_2 ," *Science*, vol. 297, no. 5590, pp. 2243–2245, 2002.
- [4] A. Kudo and Y. Miseki, "Heterogeneous photocatalyst materials for water splitting," *Chemical Society Reviews*, vol. 38, no. 1, pp. 253–278, 2009.
- [5] K. Maeda and K. Domen, "Photocatalytic water splitting: recent progress and future challenges," *The Journal of Physical Chemistry Letters*, vol. 1, no. 18, pp. 2655–2661, 2010.
- [6] J. S. Lee, "Photocatalytic water splitting under visible light with particulate semiconductor catalysts," *Catalysis Surveys from Asia*, vol. 9, no. 4, pp. 217–227, 2005.
- [7] X. B. Chen, S. H. Shen, L. J. Guo, and S. S. Mao, "Semiconductor-based photocatalytic hydrogen generation," *Chemical Reviews*, vol. 110, no. 11, pp. 6503–6570, 2010.
- [8] M. W. Kanan and D. G. Nocera, "In situ formation of an oxygen-evolving catalyst in neutral water containing phosphate and Co^{2+} ," *Science*, vol. 321, no. 5892, pp. 1072–1075, 2008.
- [9] A. J. Leenheer and H. A. Atwater, "Water-splitting photoelectrolysis reaction rate via microscopic imaging of evolved oxygen bubbles," *Journal of the Electrochemical Society*, vol. 157, no. 9, pp. B1290–B1294, 2010.
- [10] M. Ni, M. K. H. Leung, D. Y. C. Leung, and K. Sumathy, "A review and recent developments in photocatalytic water-splitting using TiO_2 for hydrogen production," *Renewable and Sustainable Energy Reviews*, vol. 11, no. 3, pp. 401–425, 2007.
- [11] M. C. Liu, L. Z. Wang, M. Lu, X. D. Yao, and L. J. Guo, "Twins in $\text{Cd}_{1-x}\text{Zn}_x\text{S}$ solid solution: highly efficient photocatalyst for hydrogen generation from water," *Energy and Environmental Science*, vol. 4, no. 4, pp. 1372–1378, 2011.
- [12] M. S. Plesset and S. A. Zwick, "The growth of vapor bubbles in superheated liquids," *Journal of Applied Physics*, vol. 25, no. 4, pp. 493–500, 1954.
- [13] H. K. Forster and N. Zuber, "Growth of a vapor bubble in a superheated liquid," *Journal of Applied Physics*, vol. 25, no. 4, pp. 474–478, 1954.
- [14] G. Son, V. K. Dhir, and N. Ramanujapu, "Dynamics and heat transfer associated with a single bubble during nucleate boiling

- on a horizontal surface," *Journal of Heat Transfer*, vol. 121, no. 3, pp. 623–631, 1999.
- [15] A. Asai, "Bubble dynamics in boiling under high heat-flux pulse heating," *Journal of Heat Transfer*, vol. 113, no. 4, pp. 973–979.
- [16] A. J. Robinson and R. L. Judd, "The dynamics of spherical bubble growth," *International Journal of Heat and Mass Transfer*, vol. 47, no. 23, pp. 5101–5113, 2004.
- [17] R. Cole and H. L. Shulman, "Bubble growth rates at high Jakob numbers," *International Journal of Heat and Mass Transfer*, vol. 9, no. 12, pp. 1377–1390, 1966.

Research Article

Facile Growth of Porous Hematite Films for Photoelectrochemical Water Splitting

Shaohua Shen, Jiangang Jiang, Penghui Guo, and Liejin Guo

International Research Center for Renewable Energy, State Key Laboratory of Multiphase Flow in Power Engineering, Xi'an Jiaotong University, Shaanxi 710049, China

Correspondence should be addressed to Shaohua Shen; shshen_xjtu@mail.xjtu.edu.cn

Received 2 December 2012; Accepted 10 February 2013

Academic Editor: Krisztina Gajda-Schranz

Copyright © 2013 Shaohua Shen et al. This is an open access article distributed under the Creative Commons Attribution License, which permits unrestricted use, distribution, and reproduction in any medium, provided the original work is properly cited.

We introduced a simple fabrication method of porous hematite films with tunable thickness in an aqueous solution containing FeCl_3 as the single precursor. We demonstrated that the optimized thickness was necessary for high performance photoelectrochemical water splitting, by balancing photon absorption and charge carrier transport. The highest photocurrent of *ca.* 0.15 mA cm^{-2} at 1.0 V versus Ag/AgCl was achieved on the 300 nm thick porous hematite film as photoanode, with IPCE at 370 nm and 0.65 V versus Ag/AgCl to be 9.0%. This simple method allows the facile fabrication of hematite films with porous nanostructure for enabling high photon harvesting efficiency and maximized interfacial charge transfer. These porous hematite films fabricated by this simple solution-based method could be easily modified by metal doping for further enhanced photoelectrochemical activity for water splitting.

1. Introduction

Since Fujishima and Honda reported water splitting in a photoelectrochemical (PEC) cell using TiO_2 as photoanode and Pt as cathode in 1972 [1], solar hydrogen production via PEC water splitting has been of great interest as the most promising way to convert solar light and water to chemical energy. In the past decades, numerous efforts have advanced considerable progress on high performance water splitting, and synchronously various semiconductor materials have been developed as photoelectrodes to show PEC activity [2–9]. However, the solar hydrogen conversion efficiency is still very low, due to the lack of suitable materials. The ideal photoelectrode material must be strongly absorptive in solar spectrum, have excellent electronic properties for efficient separation of photoexcited charges, have and high reactivity for surface chemical reactions (generally water oxidation reaction for photoanodes). Unfortunately, such an ideal material has not been found yet.

By comparing other metal oxides such as TiO_2 , WO_3 , and ZnO, hematite ($\alpha\text{-Fe}_2\text{O}_3$) has been extensively studied

as a strong photoanode candidate for solar water oxidation, because its narrow band gap permits light absorption in wide range solar spectrum, and additionally it is low cost, nontoxic, chemically stable [10]. However, its PEC performance has been severely limited by some unfavorable characteristics, such as small optical absorption coefficient, poor carrier mobility, and ultrafast recombination of photogenerated carriers. In spite of this, recent efforts on metal doped and nanostructured hematite photoanodes have resulted in encouraging advances in high performance PEC water splitting by increasing visible light response as well as promoting charge transport. For example, various n-type dopants such as Ti^{4+} [11], Zr^{4+} [12], Sn^{4+} [13], Pt^{4+} [14], and Ta^{5+} [15] have been introduced into hematite lattice to improve electrical conductivity for efficient charge transfer and separation, which, without exception, gave rise to enhanced PEC performances for water splitting on these metal doped hematite. Kay et al. [16] produced a very successful system of Si doped cauliflower-type Fe_2O_3 prepared by atmospheric pressure chemical vapor deposition (APCVD). A high photocurrent, 2.2 mA cm^{-2} at 1.23 V versus

the reversible hydrogen electrode (RHE) in 1 M NaOH at standard solar condition, was obtained on this photoanode. They also successfully increased the performance of hematite photoelectrodes for solar water splitting by preparing an extremely thin layer (12.5 nm) of this visible light absorber on a nanostructured scaffold (SiO_x) using a spray pyrolysis method [17]. The SiO_x monolayer could change the hematite nucleation and growth mechanism, increasing its crystallinity and reducing the concentration of carrier trapping states of the ultrathin hematite films. Very recently, Lin et al. [18] fabricated an innovative p-n hematite junction using atomic layer deposition (ALD) method. When grown on n-type hematite, the p-type layer was found to create a built-in field that could be used to assist PEC water splitting reactions.

Hematite films can be successfully fabricated by different methods, including APCVD [16], pulse laser deposition [19], ALD [20], and reactive DC magnetron sputtering [21], with facile control of chemical composition, deposition parameters, and excellent reproducibility. However, these techniques and related manufacturing equipments are of high cost, which severely limits their application for the fabrication of large surface area hematite films. In contrast, solution-based growth methods are always economic and manageable and thus have attracted great interest to be used for hematite film growth. For example, Lionel and coworkers developed a low temperature aqueous chemical growth method for the fabrication of hematite nanorod arrays for PEC water splitting [22, 23]. Despite of its low PEC activity even after doping metal, the nanorod structure is still supposed to favor charge transport [24, 25]. Wang et al. [26] reported a simple deposition-annealing process for the fabrication of transparent, mesoporous hematite films on FTO (F: SnO_2) substrate, using nontoxic FeCl_3 as the Fe precursor, as well as their implementation as photoanodes for efficient water oxidation. Grätzel group [27, 28] demonstrated the formation of mesoporous hematite films using a nanoparticle suspension by the doctor-blade method. This solution-based colloidal route offers an inexpensive path to electrodes with highly attractive morphologies for enabling high photon harvesting efficiency and maximized interfacial charge transfer, which resulted in the highest photocurrent reported for a solution-processed hematite photoanode.

In this study, a simple solution-based method was developed for growing porous hematite films on FTO substrates using FeCl_3 as the only precursor. It was found that the film thickness could be easily controlled by the concentration of FeCl_3 aqueous solution, which was supposed to be the critical factor determining the PEC activities of these porous hematite films for solar water splitting.

2. Experimental Section

Porous $\alpha\text{-Fe}_2\text{O}_3$ films with tunable thickness were facilely grown on FTO (Pilkington, TEC7) substrates in an aqueous solution containing ferric chloride ($\text{FeCl}_3 \cdot 6\text{H}_2\text{O}$, Sigma-Aldrich) as the only precursor. Typically, two back-to-back FTO glasses were placed, leaning against the wall, in a cap-sealed glass bottle containing ferric chloride ($\text{FeCl}_3 \cdot 6\text{H}_2\text{O}$)

aqueous solution with different concentrations. After heated in a regular oven at 100°C for 24 h, the resultant yellow or light yellow films were washed with distilled water and dried, then annealed at 750°C for 5 min with ramping rate of $25^\circ\text{C}/\text{min}$. These $\alpha\text{-Fe}_2\text{O}_3$ films, grown in 0.02, 0.05, 0.10, and 0.15 M FeCl_3 aqueous solution, were denoted as Fex ($x = 0.02, 0.05, 0.10, \text{ and } 0.15$), respectively.

Scanning electron microscopy (SEM) images were obtained with a Hitachi environmental field emission scanning electron microscope (model S-4300SE/N) operating in secondary electron detection mode. Raman scattering study was performed on a Jobin Yvon LabRAM HR spectrometer using 514.5 nm irradiation from an argon ion laser at 20 mW. Spectral transmittance and absorbance measurements were taken on the samples with a commercial thin film metrology system (Scientific Computing International, FilmTek Par 3000 SE). The X-ray photoelectron spectroscopy (XPS) measurements were conducted on a Kratos spectrometer (AXIS Ultra DLD) with monochromatic Al $K\alpha$ radiation ($h\nu = 1486.69 \text{ eV}$) and with a concentric hemispherical analyzer.

PEC measurements were conducted by a potentiostat (Pine Instruments Bipotentiostat) in 0.5 M NaCl (pH 6.7) using a three-electrode configuration, with the porous $\alpha\text{-Fe}_2\text{O}_3$ film as the working electrode, Ag/AgCl as the reference electrode, and Pt as the counter electrode. A 1 cm^2 masked-off, sealed area of the $\alpha\text{-Fe}_2\text{O}_3$ sample was irradiated with a 300 W Xe lamp solar simulator through an AM 1.5G filter (Oriel) with light intensity set as $100 \text{ mW}\cdot\text{cm}^{-2}$. Incident photon-to-current conversion efficiency (IPCE) measurements were performed using a 300 W Xe lamp integrated with a computer-controlled monochromator (Beijing Optic Instrument Factory), a photo chopper (PARC), and a lock-in amplifier (Signal Recovery) used for photocurrent detection. IPCE measurements were performed in 0.5 M NaCl solution with potential controlled at 0.65 V as versus Ag/AgCl reference electrode (i.e., 1.23 V versus reversible hydrogen electrode (RHE), calculated from $E_{\text{RHE}} = E_{\text{Ag/AgCl}} + 0.1976 + 0.057 \cdot \text{pH}$). N_2 gas was continuously bubbled in solution before and during all these electrochemical experiments to remove any dissolved O_2 and therefore suppress the reduction of O_2 at the counter electrode.

3. Results and Discussion

In this study, we introduced a new facile fabrication method of porous $\alpha\text{-Fe}_2\text{O}_3$ films with controlled thickness in an aqueous solution only containing FeCl_3 as the single precursor and demonstrated the PEC property depending on the thickness which was influenced by the concentration of FeCl_3 aqueous solution.

The thickness of porous $\alpha\text{-Fe}_2\text{O}_3$ films as a function of the concentration of FeCl_3 aqueous solution was investigated by SEM images in Figures 1 and 2. As shown in Figures 1(a) and 2(a), the Fe0.02 film showed FTO substrate partially uncovered, due to the low concentration of FeCl_3 aqueous solution. With the concentration of FeCl_3 aqueous solution increasing from 0.02 M to 0.15 M, the FTO substrates were covered by $\alpha\text{-Fe}_2\text{O}_3$ films (Figures 1(b)–1(d)) and simultaneously thickness

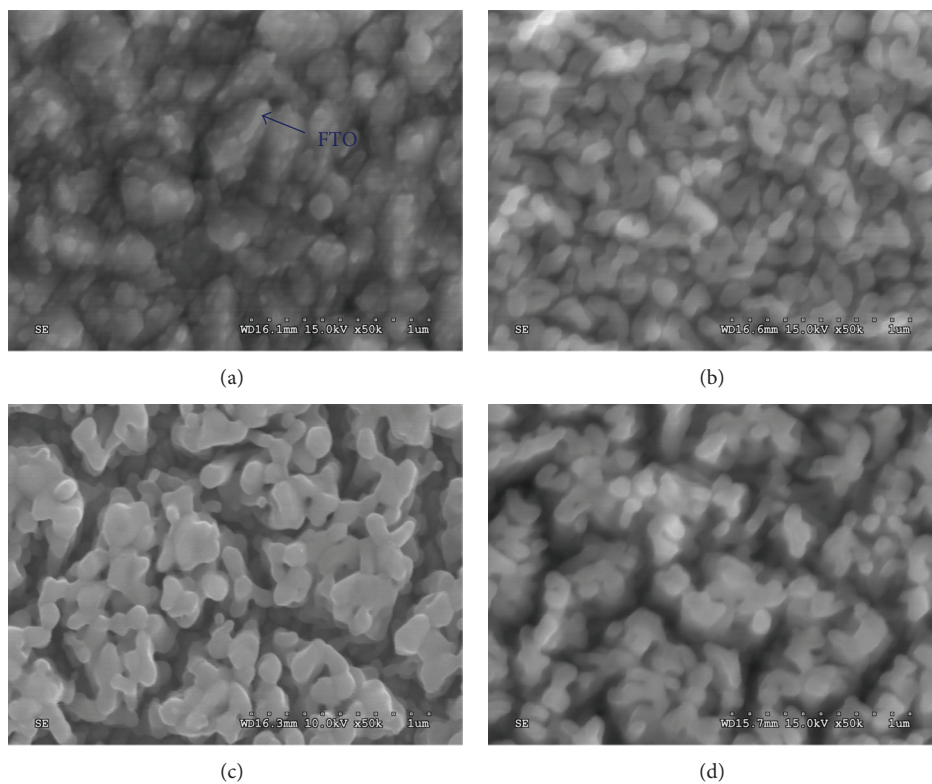


FIGURE 1: Top view SEM images of porous α - Fe_2O_3 films grown in FeCl_3 aqueous solution. (a) Fe0.02, (b) Fe0.05, (c) Fe0.10, and (d) Fe0.15.

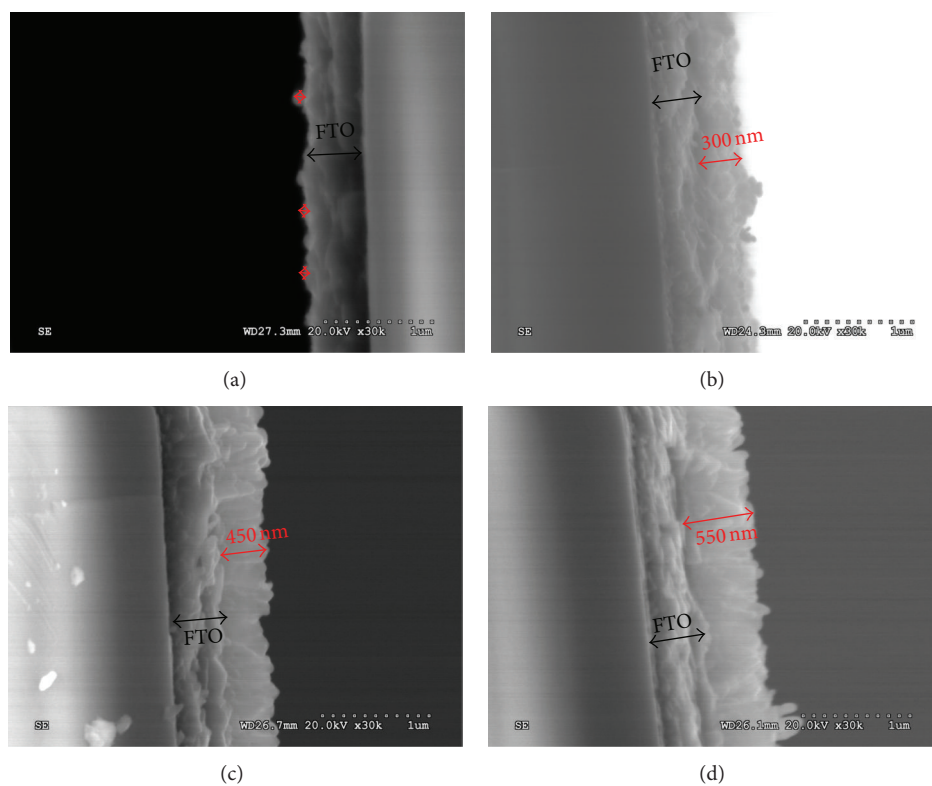


FIGURE 2: Cross-sectional SEM images of porous α - Fe_2O_3 films grown in FeCl_3 aqueous solution. (a) Fe0.02, (b) Fe0.05, (c) Fe0.10, and (d) Fe0.15.

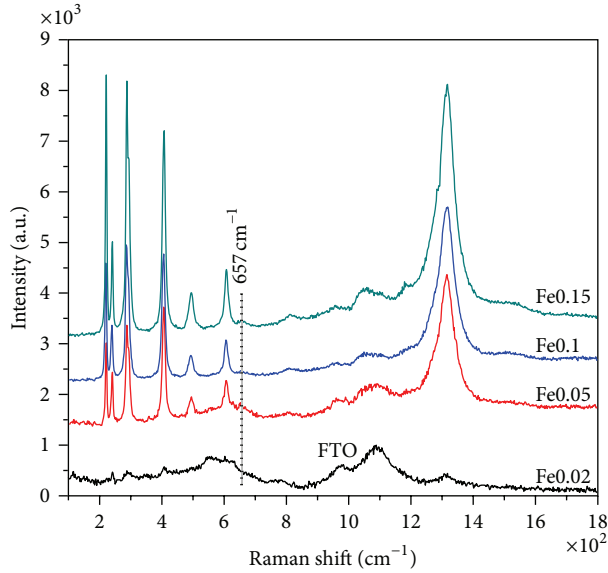


FIGURE 3: The Raman spectra of porous α - Fe_2O_3 films grown in FeCl_3 aqueous solution.

increased from 300 nm up to 550 nm (Figures 2(b)–2(d)). Except for the Fe0.02 film with FTO substrate exposed, all the other films were of porous structure. Such porosity structured films are of highly attractive morphologies for enabling a high photon harvesting efficiency with hematite and providing large contact area between semiconductor photoanode and electrolyte to promote interfacial charge transfer [27]. Furthermore, the thickness of the porous α - Fe_2O_3 films could be easily controlled by varying FeCl_3 precursor solution concentration during the solution-based process.

The crystal structure of these prepared α - Fe_2O_3 films was confirmed by the Raman spectra. As shown in Figure 3, the films of Fe0.05, Fe0.10, and Fe0.15 exhibited characteristic peaks ascribed to hematite crystalline phase [29], while the Fe0.02 film mainly showed the Raman bands which arose from the FTO (fluorine-doped SnO_2) substrate [30], due to the small thickness of α - Fe_2O_3 or the partial coverage of FTO by α - Fe_2O_3 (see SEM image in Figures 1(a) and 2(a)). The additional peak located at approximately 657 cm^{-1} should be assigned to magnetite (Fe_3O_4), and its existence has been previously reported in some other high-valence metal-doped or high-temperature annealed hematite photoelectrodes [14, 29]. This should be related to the doping of high-valence metal or diffusion of Sn^{4+} from FTO substrate into the lattice of hematite, which induced the appearance of Fe^{2+} (Fe_3O_4) to keep the electric neutrality.

XPS spectroscopy was performed on these porous α - Fe_2O_3 films to analyze the chemical states of Fe and Sn in hematite crystal lattice. The Fe 2p spectra shown in Figure 4(a) revealed that iron exists predominately as Fe^{3+} , with binding energies for Fe $2p_{3/2}$ and Fe $2p_{1/2}$ levels located at *ca.* 710.9 and 724.3 eV, respectively. With the decreasing film thickness, the emerging peak located at *ca.* 716.6 eV should be related to Sn 3p, due to the diffusion of Sn from

FTO substrate to hematite lattice. This was also confirmed by Sn 3d spectra, as shown in Figure 4(b). The increasing intensity of Sn 3p peak (Figure 4(a)) and Sn 3d peak (Figure 4(b)) indicates that the decreasing film thickness from Fe0.15 to Fe0.02 makes it increasingly easy for Sn to diffuse from FTO substrate to hematite near-surface region. As a result, the surface molar ratio of Sn:Fe obviously increased, for the thinnest film of Fe0.02 especially, as shown in Figure 4(c). By carefully checking the position at *ca.* 713.8 eV in Fe 2p spectra, the increasing intensity could be associated with the superposition of XPS peak (satellite) of divalent iron in the form of Fe_3O_4 [31, 32]. The existence of Fe_3O_4 , to maintain charge neutrality by compensating for Sn^{4+} diffusion, could be reasonable as also evidenced by the Raman spectra.

The color of the prepared α - Fe_2O_3 films varied from red brown to light yellow, depending on the decreasing concentration of FeCl_3 precursor solution. As reflected in optical spectra shown in Figure 5(a), the transmittance decreased in the whole visible spectrum for these films, due to the thickness gradually increasing from Fe0.02 to Fe0.15. It is indicated the thickness of α - Fe_2O_3 films affects their photon absorptivity. However, the band gaps of these α - Fe_2O_3 films were quite similar and at 2.1–2.2 eV (Figure 5(b)), as estimated from (1) (Kubelka-Munk equation) [33] as follows:

$$\alpha hv = C(hv - E_g)^m \quad (1)$$

where α is the absorption coefficient of the material, hv is the photon energy in eV, E_g is the band gap in eV, and C is a proportionality constant. m is also a constant, being 1/2 for a direct and 2 for an indirect band gap semiconductor. In this case, m is equal to 2 for α - Fe_2O_3 as an indirect band gap semiconductor [17, 21]. The onset of electronic transition at *ca.* 3.7 eV for Fe0.02 and Fe0.05 should be derived from FTO substrate, due to their small thickness of α - Fe_2O_3 . That is to say, the various thicknesses mainly affected the absorptivity rather than the band gap of these prepared α - Fe_2O_3 films. The influence of thickness on the PEC activity will be discussed in the following section.

It has been reported that high temperature annealing, which induced Sn diffusion from FTO substrate to hematite lattice and thus the appearance of Fe^{2+} , was very effective for enhanced PEC activity. It was proposed that diffused Sn^{4+} (like some dopants such as Ti^{4+} [11], Zr^{4+} [12], Pt^{4+} [14], etc.) could act as electron donating substitutional impurities for increased electronic conductivity [28] meanwhile, the existence of both Fe^{3+} and Fe^{2+} contributed to the improvement of electron transport by a polaron hopping mechanism [31, 34]. Thus, a high temperature annealing process was used in this study to activate the porous α - Fe_2O_3 films for efficient PEC water splitting. Considering the same activation process for all these α - Fe_2O_3 films, some other reasons should be responsible for their different PEC activities, for example, film thickness. Indeed, film thickness is a key factor affecting the PEC activity of photoelectrodes by simultaneously influencing photon absorption and charge carrier transport. In order to achieve optical thickness for enough charge carriers created by photons, physically thick structures are always required. However, the thick films

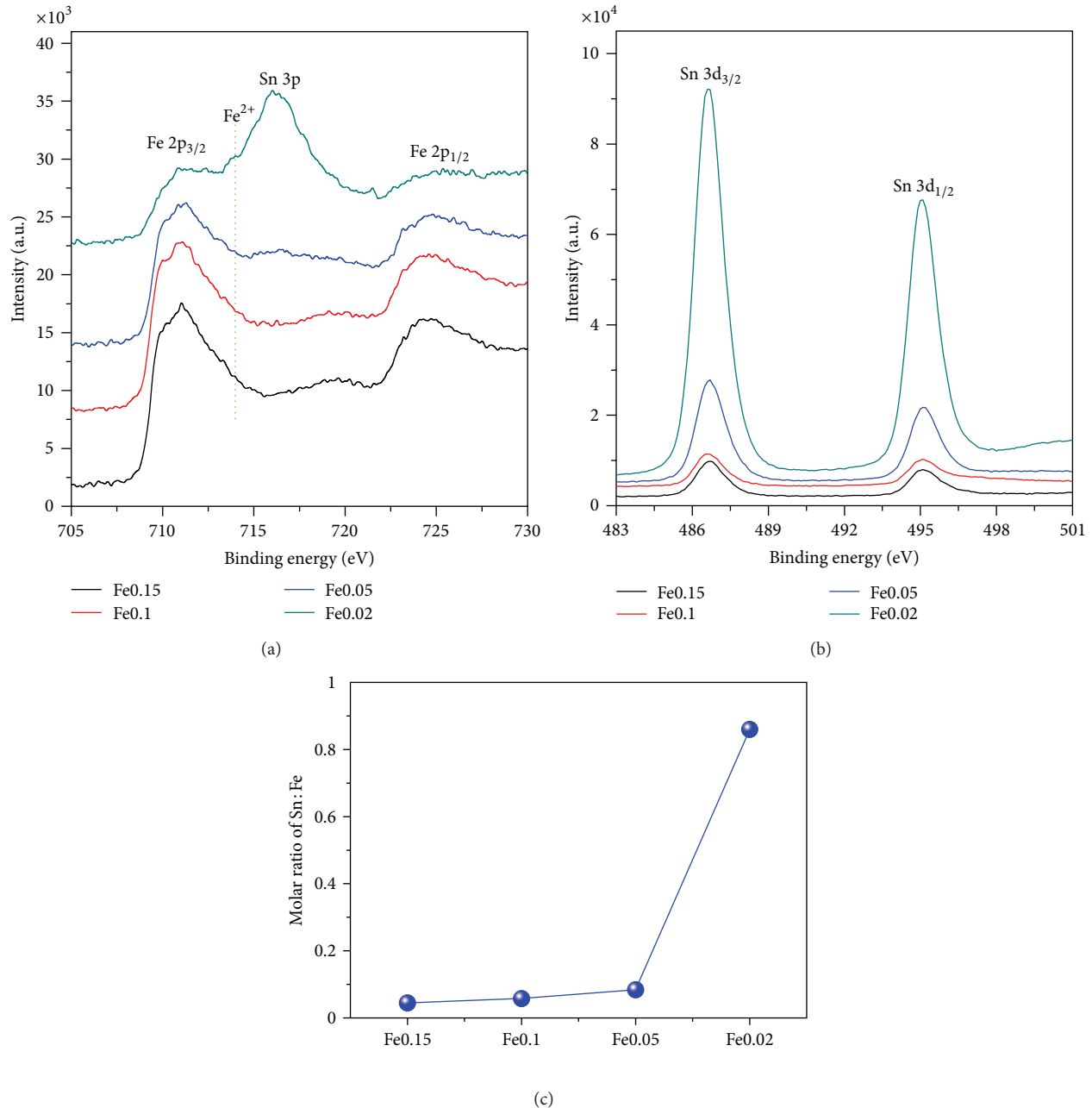


FIGURE 4: XPS analysis results of prepared porous α -Fe₂O₃ films. (a) Fe 2p spectra, (b) Sn 3d spectra, and (c) surface molar ratio of Sn:Fe.

would result in long diffusion distance for charge carriers to be transferred to surface before recombination.

The PEC performance for these porous α -Fe₂O₃ films, with different thickness, is shown by sweeping current-potential scans in 0.5 M NaCl electrolyte (pH 6.7) with chopped illumination of solar simulator (AM 1.5 G, 100 mW cm⁻²) in Figure 6. The Fe0.02 film exhibited a quite low photocurrent, due to its very small thickness which greatly limited the photon absorption. With thickness increasing to 300 nm for the Fe0.05 film, the PEC performance was remarkably enhanced with photocurrent

at 1.0 V versus Ag/AgCl increased by about 15 times. This is because the much thicker film could absorb enough photons to create electrons and holes for PEC water splitting. However, when the film thickness further increased for Fe0.10 and Fe0.15, the photocurrents gradually decreased. This should be related to the long diffusion distance for charge carriers hampered their facile transfer to surface before recombination. Figure 7 revealed the change tendency of IPCE at 370 nm for these porous α -Fe₂O₃ films, which increased from 1.8% for Fe0.02 to 9.0% for Fe0.05, and then gradually decreased to 3.3% for Fe0.15. Consequently,

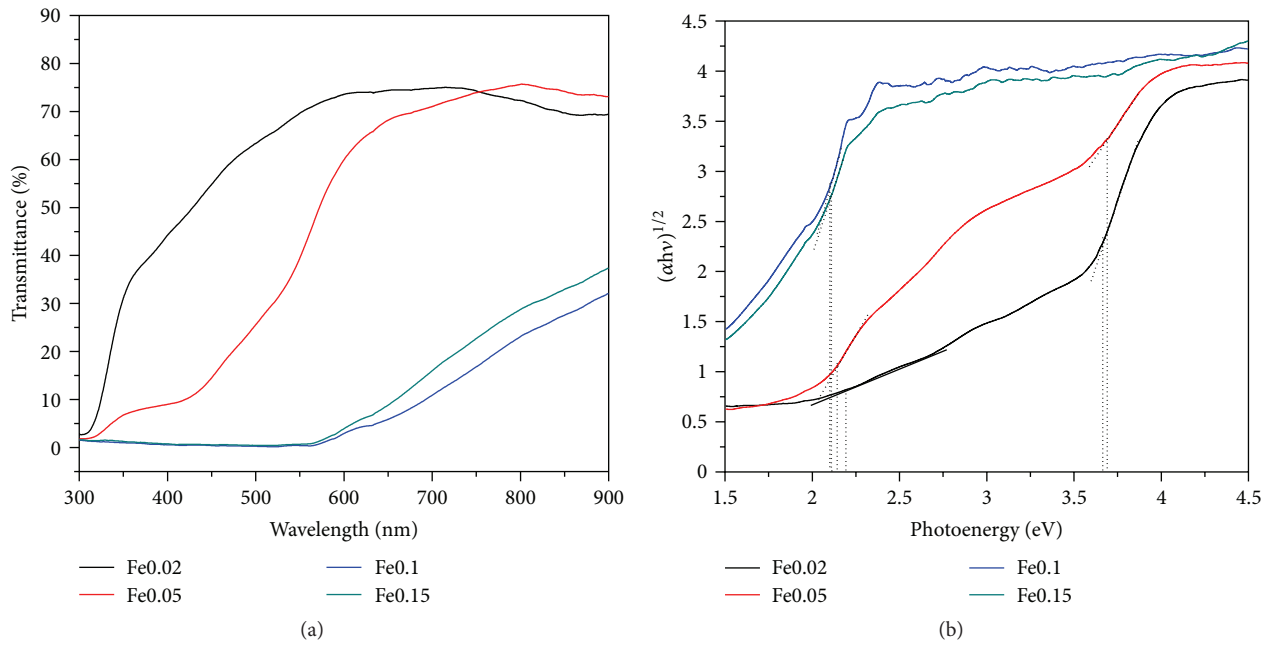


FIGURE 5: (a) Spectral transmittance and (b) Tauc plots of porous α - Fe_2O_3 films grown in FeCl_3 aqueous solution.

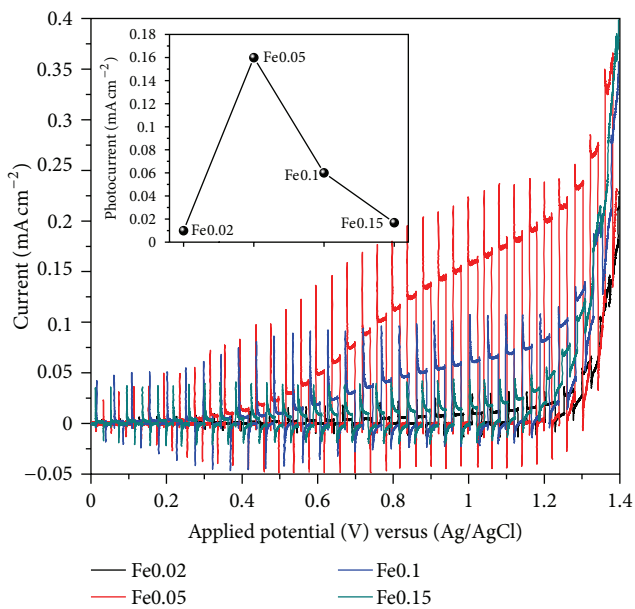


FIGURE 6: Chopped current-voltage curves of porous α - Fe_2O_3 films grown in FeCl_3 aqueous solution. Inset: photocurrent of porous α - Fe_2O_3 films at applied potential of 1 V versus Ag/AgCl.

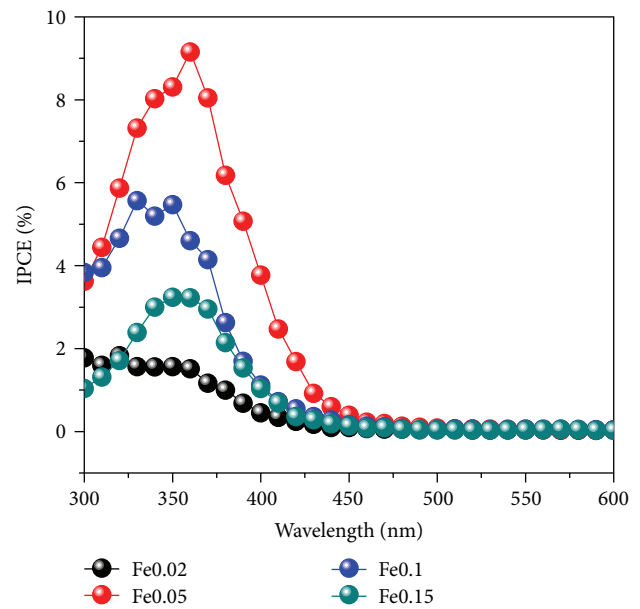


FIGURE 7: IPCE of porous α - Fe_2O_3 films with potential controlled at 0.65 versus Ag/AgCl.

optimized film thickness to balance photon absorption and charge carrier transport is of great importance for high performance PEC water splitting.

4. Conclusions

In this study, porous hematite films with tunable thickness were facilely fabricated in an aqueous solution containing

FeCl_3 as the single precursor. With the concentration of FeCl_3 aqueous solution increasing, the thickness gradually increased, whereas the photoelectrochemical performance increased first and then decreased. The optimized thickness was found to be necessary for high performance photoelectrochemical water splitting, by balancing photon absorption and charge carrier transport. It is believed that these porous hematite films fabricated via a facile solution-based method

could show enhanced photoelectrochemical activity for water splitting after further modification (e.g., metal doping).

Conflict of Interests

The authors declare no conflict of interest.

Acknowledgments

The authors gratefully acknowledge the financial support of the National Natural Science Foundation of China (no. 51102194, and no. 51121092), the Doctoral Program of the Ministry of Education (no. 20110201120040), the Natural Science Foundation of Shaanxi province (no. 2011JQ7017), and the National Basic Research Program of China (no. 2009CB220000). One of the authors (S. Shen) was supported by the Fundamental Research Funds for the Central Universities.

References

- [1] A. Fujishima and K. Honda, "Electrochemical photolysis of water at a semiconductor electrode," *Nature*, vol. 238, no. 5358, pp. 37–38, 1972.
- [2] H. M. Chen, C. K. Chen, R. S. Liu, L. Zhang, J. J. Zhang, and D. P. Wilkinson, "Nano-architecture and material designs for water splitting photoelectrodes," *Chemical Society Reviews*, vol. 41, no. 17, pp. 5654–5671, 2012.
- [3] J. Z. Zhang, "Metal oxide nanomaterials for solar hydrogen generation from photoelectrochemical water splitting," *MRS Bulletin*, vol. 36, no. 1, pp. 48–55, 2011.
- [4] Y. Li and J. Z. Zhang, "Hydrogen generation from photoelectrochemical water splitting based on nanomaterials," *Laser and Photonics Reviews*, vol. 4, no. 4, pp. 517–528, 2010.
- [5] B. D. Alexander, P. J. Kulesza, I. Rutkowska, R. Solarska, and J. Augustynski, "Metal oxide photoanodes for solar hydrogen production," *Journal of Materials Chemistry*, vol. 18, no. 20, pp. 2298–2303, 2008.
- [6] J. Sun, D. K. Zhong, and D. R. Gamelin, "Composite photoanodes for photoelectrochemical solar water splitting," *Energy and Environmental Science*, vol. 3, no. 9, pp. 1252–1261, 2010.
- [7] X. Chen, S. Shen, L. Guo, and S. S. Mao, "Semiconductor-based photocatalytic hydrogen generation," *Chemical Reviews*, vol. 110, no. 11, pp. 6503–6570, 2010.
- [8] S. Shen and S. S. Mao, "Nanostructure designs for effective solar-to-hydrogen conversion," *Nanophotonics*, vol. 1, no. 1, pp. 31–50, 2012.
- [9] S. Shen, J. Shi, P. Guo, and L. Guo, "Visible-light-driven photocatalytic water splitting on nanostructured semiconducting materials," *International Journal of Nanotechnology*, vol. 8, no. 6-7, pp. 523–591, 2011.
- [10] K. Sivula, F. Le Formal, and M. Grätzel, "Solar water splitting: progress using hematite (α -Fe₂O₃) photoelectrodes," *ChemSusChem*, vol. 4, no. 4, pp. 432–449, 2011.
- [11] P. Zhang, A. Kleiman-Shwarsctein, Y.-S. Hu et al., "Oriented Ti doped hematite thin film as active photoanodes synthesized by facile APCVD," *Energy and Environmental Science*, vol. 4, no. 3, pp. 1020–1028, 2011.
- [12] P. Kumar, P. Sharma, R. Shrivastav, S. Dass, and V. R. Satsangi, "Electrodeposited zirconium-doped α -Fe₂O₃ thin film for photoelectrochemical water splitting," *International Journal of Hydrogen Energy*, vol. 36, no. 4, pp. 2777–2784, 2011.
- [13] Y. Ling, G. Wang, D. A. Wheeler, J. Z. Zhang, and Y. Li, "Sn-doped hematite nanostructures for photoelectrochemical water splitting," *Nano Letters*, vol. 11, no. 5, pp. 2119–2125, 2011.
- [14] Y.-S. Hu, A. Kleiman-Shwarsctein, A. J. Forman, D. Hazen, J.-N. Park, and E. W. McFarland, "Pt-doped α -Fe₂O₃ thin films active for photoelectrochemical water splitting," *Chemistry of Materials*, vol. 20, no. 12, pp. 3803–3805, 2008.
- [15] V. M. Aroutiounian, V. M. Arakelyan, G. E. Shahnazaryan, G. M. Stepanyan, J. A. Turner, and O. Khaselev, "Investigation of ceramic Fe₂O₃/Ta photoelectrodes for solar energy photoelectrochemical converters," *International Journal of Hydrogen Energy*, vol. 27, no. 1, pp. 33–38, 2002.
- [16] A. Kay, I. Cesar, and M. Grätzel, "New benchmark for water photooxidation by nanostructured α -Fe₂O₃ films," *Journal of the American Chemical Society*, vol. 128, no. 49, pp. 15714–15721, 2006.
- [17] F. L. Formal, M. Grätzel, and K. Sivula, "Controlling photoactivity in Ultrathin Hematite films for solar water-splitting," *Advanced Functional Materials*, vol. 20, no. 7, pp. 1099–1107, 2010.
- [18] Y. Lin, Y. Xu, M. T. Mayer et al., "Growth of p-type hematite by atomic layer deposition and its utilization for improved solar water splitting," *Journal of American Chemical Society*, vol. 134, no. 12, pp. 5508–5511, 2012.
- [19] C. X. Kronawitter, S. S. Mao, and B. R. Antoun, "Doped, porous iron oxide films and their optical functions and anodic photocurrents for solar water splitting," *Applied Physics Letters*, vol. 98, no. 9, Article ID 092108, 2011.
- [20] M. Aronniemi, J. Saino, and J. Lahtinen, "Characterization and gas-sensing behavior of an iron oxide thin film prepared by atomic layer deposition," *Thin Solid Films*, vol. 516, no. 18, pp. 6110–6115, 2008.
- [21] J. A. Glasscock, P. R. F. Barnes, I. C. Plumb, and N. Savvides, "Enhancement of photoelectrochemical hydrogen production from hematite thin films by the introduction of Ti and Si," *Journal of Physical Chemistry C*, vol. 111, no. 44, pp. 16477–16488, 2007.
- [22] L. Vayssieres, N. Beermann, S. E. Lindquist, and A. Hagfeldt, "Controlled aqueous chemical growth of oriented three-dimensional crystalline nanorod arrays: application to iron(III) oxides," *Chemistry of Materials*, vol. 13, no. 2, pp. 233–235, 2001.
- [23] T. Lindgren, H. Wang, N. Beermann, L. Vayssieres, A. Hagfeldt, and S. E. Lindquist, "Aqueous photoelectrochemistry of hematite nanorod array," *Solar Energy Materials and Solar Cells*, vol. 71, no. 2, pp. 231–243, 2002.
- [24] S. Shen, J. Jiang, P. Guo, C. X. Kronawitter, S. S. Mao, and L. Guo, "Effect of Cr doping on the photoelectrochemical performance of hematite nanorod photoanodes," *Nano Energy*, vol. 1, no. 5, pp. 732–741, 2012.
- [25] S. Shen, C. X. Kronawitter, J. Jiang, S. S. Mao, and L. Guo, "Surface tuning for promoted charge transfer in hematite nanorod arrays as water-splitting photoanodes," *Nano Research*, vol. 5, no. 5, pp. 327–336, 2012.
- [26] G. Wang, Y. Ling, D. A. Wheeler et al., "Facile synthesis of highly photoactive α -Fe₂O₃-based films for water oxidation," *Nano Letters*, vol. 11, no. 8, pp. 3503–3509, 2011.
- [27] J. Brillet, M. Grätzel, and K. Sivula, "Decoupling feature size and functionality in solution-processed, porous hematite electrodes for solar water splitting," *Nano Letters*, vol. 10, no. 10, pp. 4155–4160, 2010.

- [28] K. Sivula, R. Zboril, F. Le Formal et al., "Photoelectrochemical water splitting with mesoporous hematite prepared by a solution-based colloidal approach," *Journal of the American Chemical Society*, vol. 132, no. 21, pp. 7436–7444, 2010.
- [29] A. Duret and M. Grätzel, "Visible light-induced water oxidation on mesoscopic α -Fe₂O₃ films made by ultrasonic spray pyrolysis," *Journal of Physical Chemistry B*, vol. 109, no. 36, pp. 17184–17191, 2005.
- [30] L. J. Larsen, D. D. Tune, P. Kemppinen, K. N. Winzenberg, S. E. Watkins, and J. G. Shapter, "Increased performance of single walled carbon nanotube photovoltaic cells through the addition of dibenzo[*b, def*]chrysene derivative," *Journal of Photochemistry and Photobiology A*, vol. 235, pp. 72–76, 2012.
- [31] R. Morrish, M. Rahman, J. M. D. MacElroy, and C. A. Wolden, "Activation of hematite nanorod arrays for photoelectrochemical water splitting," *ChemSusChem*, vol. 4, no. 4, pp. 474–479, 2011.
- [32] M. C. Biesinger, B. P. Payne, A. P. Grosvenor, L. W. M. Lau, A. R. Gerson, and R. S. C. Smart, "Resolving surface chemical states in XPS analysis of first row transition metals, oxides and hydroxides: Cr, Mn, Fe, Co and Ni," *Applied Surface Science*, vol. 257, no. 7, pp. 2717–2730, 2011.
- [33] A. E. Morales, E. S. Mora, and U. Pal, "Use of diffuse reflectance spectroscopy for optical characterization of unsupported nanostructures," *Revista Mexicana De Fisica S*, vol. 53, no. 5, pp. 18–22, 2007.
- [34] N. T. Hahn and C. B. Mullins, "Photoelectrochemical performance of nanostructured Ti- and Sn-doped α -Fe₂O₃ photoanodes," *Chemistry of Materials*, vol. 22, no. 23, pp. 6474–6482, 2010.

Research Article

Structural and Photoelectrochemical Properties of Cu-Doped CdS Thin Films Prepared by Ultrasonic Spray Pyrolysis

Rui Xie, Jinzhan Su, Mingtao Li, and Liejin Guo

International Research Center for Renewable Energy, State Key Laboratory of Multiphase Flow in Power Engineering, Xi'an Jiaotong University, Xi'an 710049, China

Correspondence should be addressed to Liejin Guo; lj-guo@mail.xjtu.edu.cn

Received 6 December 2012; Accepted 13 January 2013

Academic Editor: Shaohua Shen

Copyright © 2013 Rui Xie et al. This is an open access article distributed under the Creative Commons Attribution License, which permits unrestricted use, distribution, and reproduction in any medium, provided the original work is properly cited.

Cu-doped CdS thin films of variable doping levels have been deposited on indium tin oxide-coated glass substrate by simple and cost-effective ultrasonic spray pyrolysis. The influences of doping concentration and annealing treatment on the structure and photoelectrochemical properties of the films were investigated. The deposited films were characterized by XRD, SEM, and UV-Vis spectra. Moreover, the films were investigated by electrochemical and photoelectrochemical measurements with regard to splitting water for solar energy conversion. The results showed that the Cu impurity can cause a structural change and red shift of absorption edge. It was found that the photocurrent can be improved by the Cu-doping process for the unannealed films under the weak illumination. The unannealed 5 at.% Cu-doped sample obtained the maximum IPCE, which achieved about 45% at 0.3 V versus SCE potential under 420 nm wavelength photoirradiation. In addition, the p-type CdS was formed with a doping of 4 at.% ~10 at.% Cu after 450°C 2 h annealed in vacuum.

1. Introduction

Hydrogen is widely considered to be the energy carrier of the future. The most promising method, environmentally friendly, of hydrogen generation is based on photoelectrochemical water decomposition using solar energy [1]. The crucial problem of this method is an appropriate choice of the suitable photoanode material. Many oxide photoelectrodes such as TiO₂, WO₃, ZnO, and SrTiO₃ have been extensively studied for hydrogen production during the past decades [2–6]. However, due to their wide band gaps, these oxides can respond only to ultraviolet (UV) light, the energy of which makes up only a small fraction of the solar spectrum. For enhancing the efficiency of light conversion, it is necessary to develop semiconductor photoelectrodes with suitable band gap to work under visible light irradiation [7]. Many efforts have been made to modify these oxide materials to visible response [8–10].

In contrast to these metal oxide photoelectrodes, many metal sulfides such as CdS have narrower band gaps that correspond to the visible light. Pristine CdS is known to show n-type characteristics due to the intrinsic defects [11]. It has

generally been considered that the formation of p-type CdS is very difficult, because of strong self-compensation effect due to sulphur vacancies [11, 12]. Cu doping was regularly conducted to form p-type CdS. The doping procedure was always by Cu element diffusion from a copper layer over the CdS layer with annealing process [13, 14]. Some other ways such as electrochemical deposition [15], chemical bath deposition [16], vacuum deposition [17], and pulsed laser deposition [18] have been tried to form p-type CdS. Ultrasonic spray pyrolysis as a simple and cost-effective method is widely used for the preparation of sulfide and oxide thin films [19]. Ultrasonic nebulized atomization provides a method to get droplets of precursor with extremely small sizes. As the droplets approach the heated substrate, the reactants diffuse to the substrate, and a heterogeneous reaction occurs, which led to the formation of thin films. In this paper, Cu-doped CdS thin films were prepared by an ultrasonic spray pyrolysis aqueous precursor, and some properties of the deposited films such as structural, morphologic, optical, and photoelectrochemical characteristics were examined to find out the probability of efficiency improving in water splitting application.

2. Experimental

2.1. Preparation of Films. Cu-doped CdS thin films were prepared by ultrasonic spray pyrolysis method with a locally fabricated ultrasonically nebulizing spray pyrolysis apparatus, which was similar to the apparatus used in [20]. ITO-coated glass ($15 \Omega/\text{sq.}$) with dimensions of $60 \times 20 \times 1.1 \text{ mm}^3$ heated at 300°C was used as substrate. The substrate temperature was calibrated by fixing a k-type thermocouple temporarily on the surface of the substrate and simultaneously measuring the heat plate temperature. Some additional parameters such as the distance between the hot plate and nozzle, the carrier gas (nitrogen, N_2) flow rate, and the velocity of the nozzle motion were optimized previously to get good quality films. In all our experiments the flow rate of carrier gas was fixed at $0.2 \text{ m}^3/\text{h}$. The intensity of oscillation of the PZT (piezoelectric transducer), the scan length, the velocity of the nozzle, and the times of scanning motion were all kept constant.

A mixed aqueous solution of cadmium chloride, thiourea and copper chloride was used as the precursor solution to deposit Cu-doped CdS thin films. At first, the aqueous solutions of cadmium chloride (0.05 M) and thiourea (0.055 M) were prepared, respectively. A solution of copper chloride (0.005 M) was obtained by adding excess EDTA to copper chloride solution and maintaining in 80°C water bath for 30 min. Then, a fixed volume of mixed aqueous solution was got by taking equal volume (20 mL) of cadmium chloride and thiourea. After that, the variable volume of copper chloride was added into the above-mentioned mixed aqueous solution with constant stirring.

After deposition, samples were subsequently cooled naturally to room temperature in air. Then each sample was cut into four pieces with dimensions of $15 \times 20 \times 1.1 \text{ mm}^3$, two of which would be annealed in vacuum at 450°C for two hours. Ohmic contacts were made on the non-CdS-coated part of ITO using Cu wire with the help of silver glue and sealed with epoxy resin. The assembled working electrodes have surface areas varying from 0.8 to 1.3 cm^2 .

2.2. Film Characterization. The surface morphology of films was recorded using a model JSM-6700F field emission scanning electron microscopy (SEM) from JOEL. The structural analysis of as-prepared films was performed by X-ray diffraction (XRD) employing a model X'Pert PRO X-ray diffractometer from PANalytical equipped with Cu K α irradiation. Optical absorption spectra were recorded in the wavelength range of 300–800 nm using a model UV4100 UV-Vis-NIR Spectrophotometer from Hitachi equipped with an integrating sphere.

Photoelectrochemical measurements were performed in a custom made cell equipped with a quartz window. The cell set up was made up of a working electrode (the deposited sample), a counter electrode (round-shaped platinum wafer with diameter of 1.8 cm and thickness of 0.1 cm), and a reference electrode (SCE, saturated calomel electrode). The measurements were performed at ambient temperature (22°C) employing an EG and G Princeton Applied Research Model 273A potentiostat and a SIGNAL RECOVERY model 5210

lock-in amplifier. The electrolyte for the capacitance measurements which were carried out at dark was 0.5 M KOH (pH = 13.6). While the electrolyte for the action spectra and linear sweep voltammetry measurement was 0.5 M Na_2SO_3 . In the linear sweep voltammetry a 350 W Xe lamp was used as light source whose intensity was determined by a radiometer (FZA, Beijing Normal University, China). While in the measurement of photocurrent action spectra, the light source was the same 350 W Xe lamp with its output chopped with a model 197 chopper (SIGNAL RECOVERY) and monochromated with an Computer Controlled monochromator (WGD30-2, BOIF, China), and its intensities were calibrated with an IL1400BL radiometer (International Light, Inc.) equipped with an SEL033 sensor head. The IPCE (the Incident Photon to Electron Conversion Efficiency) was calculated via the formula in [9] without correction for the reflection loss of the quartz window and the absorption loss of the electrolyte.

3. Results and Discussion

3.1. Structure and Morphology. The deposited films appear transparent, smooth, and uniform to the eye, while their colors became darker with higher doping level. Figure 1 shows SEM pictures of six of the samples. It was observed that the diameters of particles in the films decrease and then increase with increasing the amount of Cu doping. The 1 at.% Cu-doped CdS particle has the smallest diameter. This should be a result of the crystalline structure change, as will be demonstrated shortly by XRD analysis, due to Cu doping. The inset of Figure 1(d) shows the cross-sectional view of 2 at.% Cu-doped CdS film. It confirmed the uniformity of the films and exhibited three layers in which the bottom layer was the glass, the interlayer was ITO, and the top layer was the CdS film with a thickness of about 284 nm.

The results of the structural analysis of the undoped and Cu-doped CdS thin films by XRD are shown in Figure 2. All the XRD peaks in all samples corresponded to those of hexagonal CdS (JCPDF 01-080-0006) except two ITO's peaks (marked by "*", JCPDF 01-089-4597) in the 10 at.% Cu-doped sample. No peak corresponds to CuS or Cu_2S , indicating that no crystalline CuS or Cu_2S phase was formed. In the low doping level a (002) preferred orientation was observed, while in the high doping level this preferred orientation disappeared. As the concentration of Cu increase the peak intensities of (100) (101) (110) (112) direction increase, while that of (002) and (103) direction decrease. So it was thought that the Cu doping provoked a crystalline structure change, which caused a change of morphology that was shown by SEM images. For the annealing samples, the XRD pattern did not change significantly after annealed in vacuum, which means that annealing treatment does not improve the crystalline quality anymore.

3.2. Optical Characteristics. The UV-Vis spectra of unannealed samples are shown in Figure 3. Two absorption edges were observed at 517 nm and 650 nm corresponding to 2.4 eV and 1.9 eV, respectively. The absorption strength in the wavelength range between 517 nm and 650 nm increases

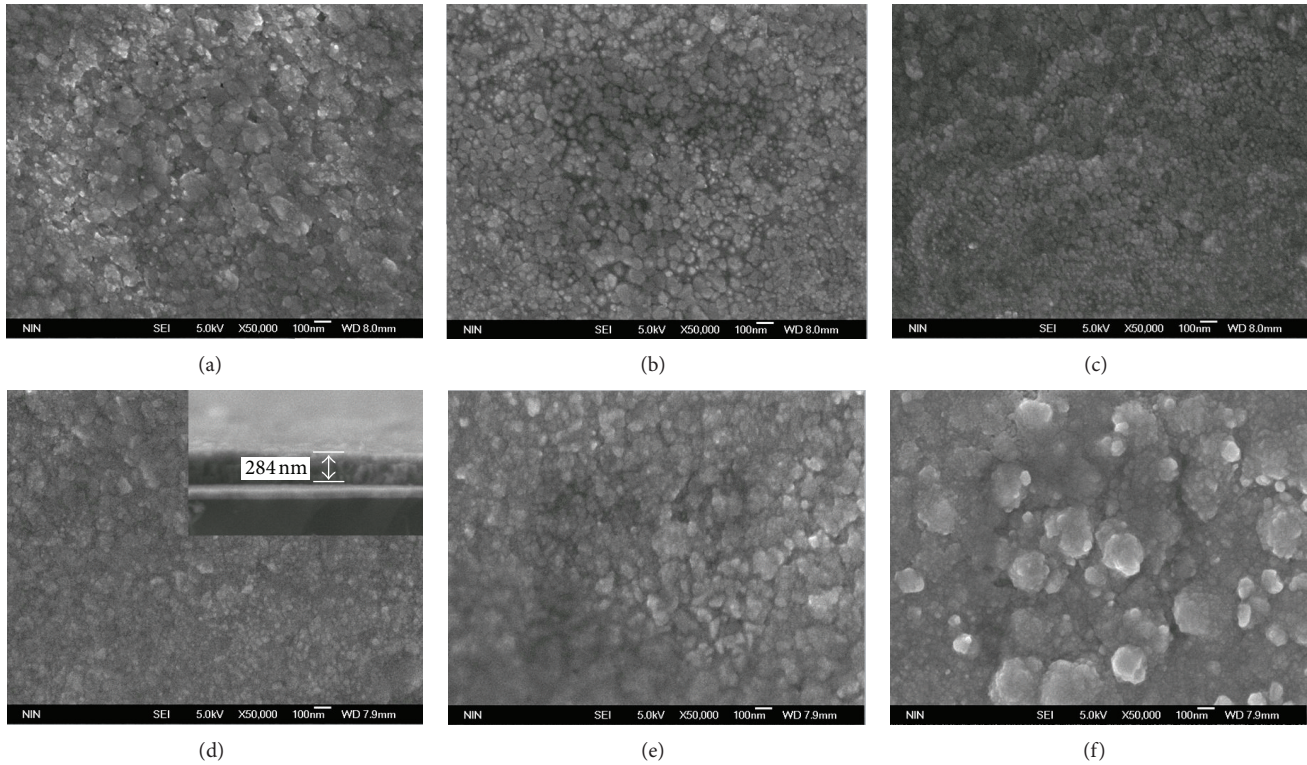


FIGURE 1: SEM images of Cu-doped CdS films: (a) 0 at.% doped, (b) 0.5 at.% doped, (c) 1 at.% doped, (d) 2 at.% doped (inset is its cross-sectional view), (e) 4 at.% doped, and (f) 5 at.% doped.

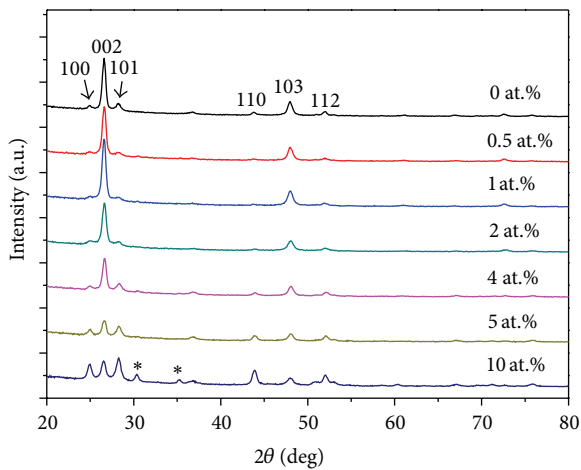


FIGURE 2: XRD patterns of Cu-doped CdS films with different doping levels.

with higher dopant concentration, which indicates that the light absorption in this wavelength range is provoked by Cu doping. A close value of 2.0 eV for the absorption edge of Cu-doped CdS was obtained by Sebastian [16]. It was assumed that the dopant of Cu gives a level situated at about 0.5 eV above the top of the valence band of the host CdS. The absorption edge of 650 nm may result from excitation from Cu level to conduction band (CB). Substitutional Cu

on a Cd site is expected to be a single acceptor, whose ionization level is located at 0.6 eV above the valence band (VB). But interstitial Cu which is expected to be a single donor has two ionization levels: one is at 0.7 eV below the CB, and the other is just below the CB [21]. Our estimated Cu level is close to ionization level of substitutional Cu, and the XRD characteristic peaks of all samples have no obvious shift, which may be infer that the Cu doping of our CdS films occurs by substitution of Cd ions with Cu ions in the lattice, rather than Cu ions occupying the interlattice sites. In addition, the UV-Vis spectra of annealed samples not shown here have no obvious changes with that of unannealed samples.

3.3. Electrochemical and Photoelectrochemical Characteristics.

Figure 4 illustrates Mott-Schottky plots of unannealed Cu-doped CdS with different doping levels. At low dopant concentration (0~2 at.%), the films reveal n-type semiconducting behavior, as positive slopes were obtained whose value increased with higher dopant concentration, indicating that the donor densities are reduced by the compensation of Cu acceptor. At higher dopant concentration (4~10 at.%), the films exhibit a different behavior. The 4 at.% doped and 10 at.% doped samples give both positive and negative slopes in their Mott-Schottky plots which means that they reveal both n-type and p-type characteristics [22]. We ascribe this duplex character behavior to the Cu atoms unevenly distributed in the host CdS film. In contrast with other samples, the 5

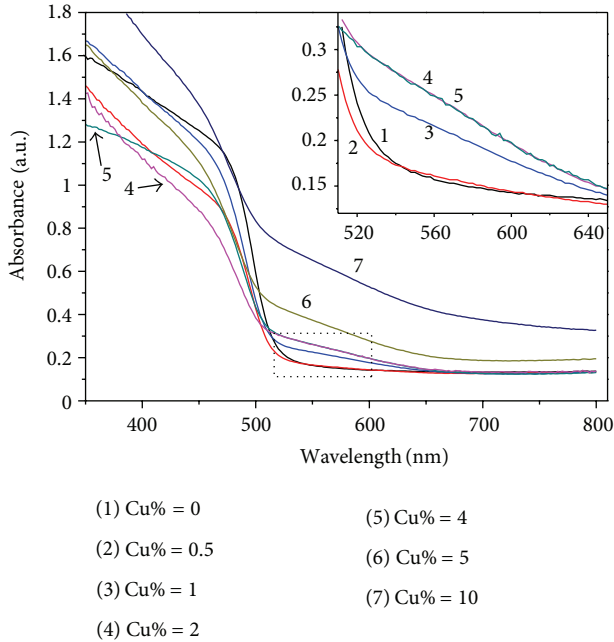


FIGURE 3: UV-Vis spectra for Cu-doped CdS films with different doping levels.

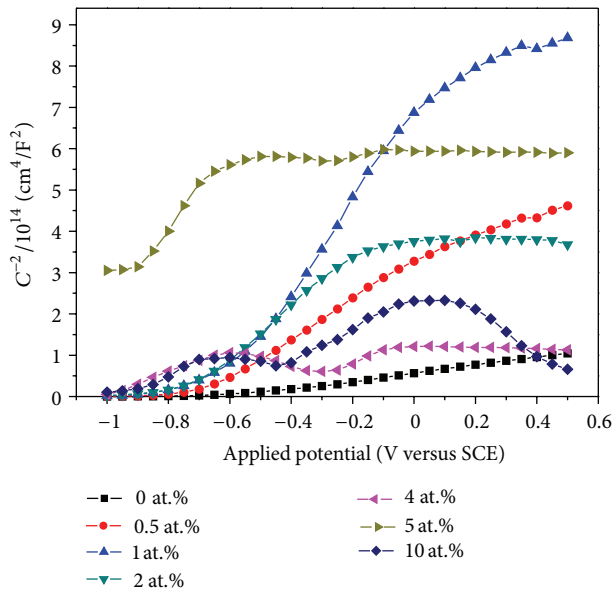


FIGURE 4: Mott-Schottky plots of unannealed Cu-doped CdS films with different doping levels.

at.% doped sample is entirely different whose capacitance value does not change significantly with different electrode potentials. Thus, this film behaves as a capacitor or more probably as a low doped-like semiconductor [22]. That should result from the equality strength of effects from Cu acceptors and defect donors (such as S vacancy).

Mott-Schottky plots for the annealed samples are represented in Figure 5. The low doped (0.5 at.% and 1 at.%) CdS

films do not showing n-type characteristic after annealing but behave like unannealed 5 at.% doped CdS as a low doped-like semiconductor [22]. The annealed 2 at.% doped CdS reveals both n-type and p-type characteristics. With the dopant concentration getting higher than 4 at.%, the conversion of conductivity type from n-type to p-type was observed for the annealed Cu-doped CdS. This annealing effect on the conductivity type that should ascribe to the Cu atoms become uniformly distributed in the host CdS film after annealing.

Figure 6 shows wavelength dependence of IPCE (incident photon-to-current conversion efficiencies) for CdS electrodes with different dopant concentrations unannealed or annealed at 450°C in vacuum. These curves clearly show the occurrence of longer wavelength response (red shift) as a result of Cu doping, as is expected from UV-Vis absorption spectra (Figure 3). The threshold wavelength is around 680 nm (corresponding to 1.82 eV), which is 30 nm longer than the absorption spectra result (650 nm). The IPCE in the red shift region increases with higher dopant concentration before the dopant concentration of 5 at.% but gets a little lower for the 10 at.% doped sample. The IPCE in the fundamental absorption region are also improved after Cu-doped. The photocurrent in this region should be derived from the exciting of electron from valence band to conduction band. It was thought that a nonuniform distribution of Cu atoms in the host CdS films was formed due to an asynchronous formation of Cd-S bond and Cu-S bond during the pyrolysis, and this nonuniform distribution of Cu atoms caused formation of disordered tiny local p-n junctions in the films. The Cu acceptors may decrease the photocurrent by acting as a recombination center, but the disordered local p-n junctions separated the generated electrons and holes and improved the photocurrent. The maximum IPCE achieved 45% at 420 nm under 0.3 V versus SCE potential for the 5 at.% doped sample.

As show in Figure 6(b), the IPCE of the annealed films increases by 18% at low dopant level (0.5 at.% and 1 at.% doped) but decreases dramatically when the dopant concentration gets higher than 2 at.%. The reason for this should be the high concentration of Cu acceptors which function as a recombination center. And there were no more local p-n junctions in the films because they were eliminated by uniformly dispersing of Cu atoms which was caused by the annealing treatment.

Figure 7 shows a plot of the photocurrent density versus applied potential obtained by linear sweep voltammetry measurement in which a shutter was used for evaluating the anodic current both in dark and light conditions. The illumination light here was white light from Xe lamp with an intensity of 165 mW/cm². It was observed that the photocurrents diminished after Cu doping. The undoped film has the highest photocurrent of approximately 5.1 mA/cm² at 0.3 V versus SCE. For the annealed Cu-doped films, the photocurrents, which were not shown here, dropped even more dramatically after doping.

The decrease of photocurrent after doping under the white light illumination was corresponding to the high carrier recombination rate. This is different from the result of IPCE measurement. The reason for this difference should

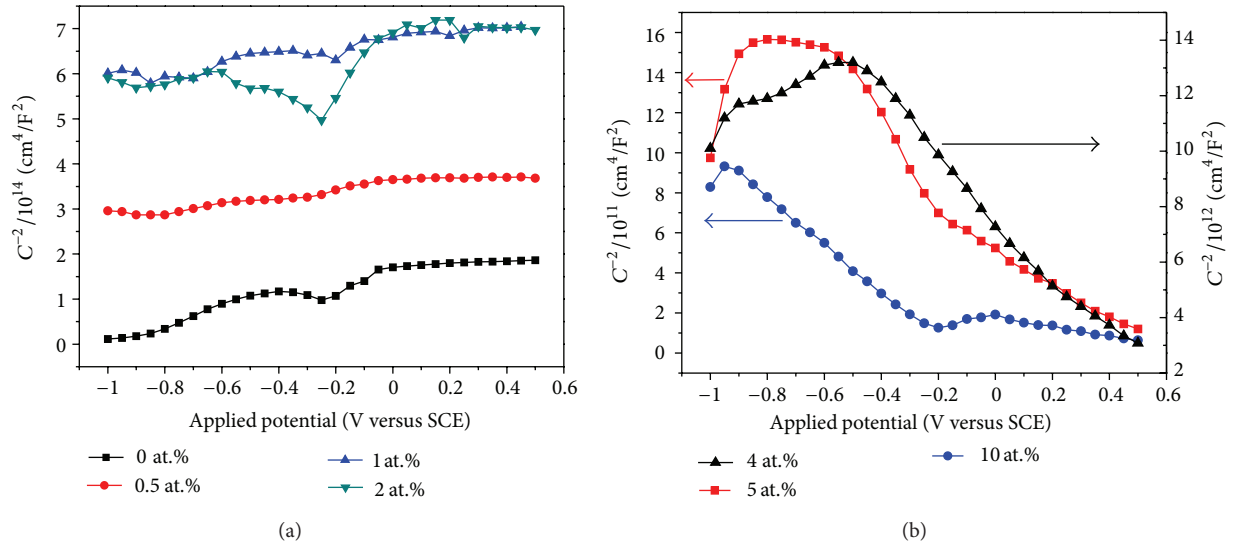


FIGURE 5: Mott-schottky plots of (a) 0 at.%, 0.5 at.%, 1 at.%, and 2 at.% Cu-doped samples and (b) 4 at.%, 5 at.%, and 10 at.% Cu-doped samples. (All samples were annealed.)

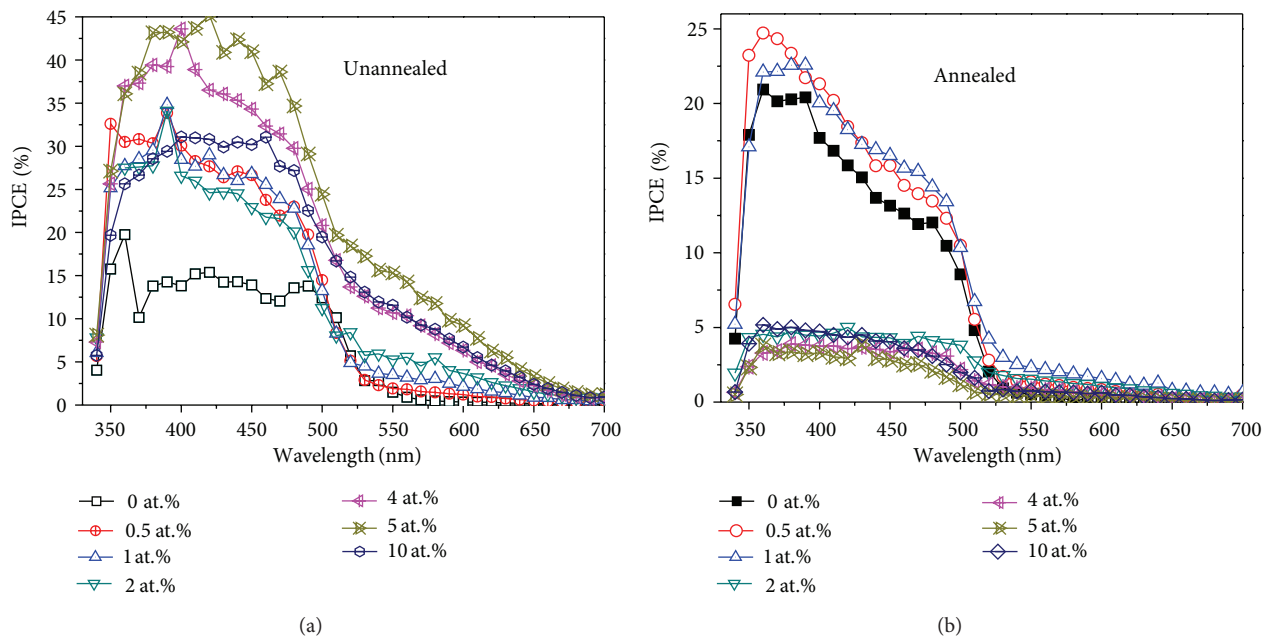


FIGURE 6: Photocurrent action spectra of (a) unannealed and (b) annealed Cu-doped CdS films with different doping levels. (The electrode potential is fixed at 0.3 V versus SCE in 0.5 M Na_2SO_3 aqueous solution.)

be the different intensity of the illumination light. The IPCE measurement was taken using the weak monochromatic light ($130\sim 750 \mu\text{W}/\text{cm}^2$), while in the linear sweep voltammetry measurement an intense white light was utilized ($165 \text{mW}/\text{cm}^2$). The large difference of the light intensity causes the variation of the photocurrent response in these two measurements. Under the weak light illumination the electron-hole pairs were spatially separated by the disordered local p-n junctions and then the separated electrons and

holes drifted towards the side of substrate and electrolyte, respectively, due to the electric field within the space-charge region, so the efficiency could be relatively high for the weak illumination. It was reported that the electron lifetime decreases with increasing light intensity [23], so the recombination of electrons and holes can be higher under the intense white light illumination, causing the photocurrent drop of the Cu-doped samples. In addition, the electric field in the space-charge region diminished under the intense white light

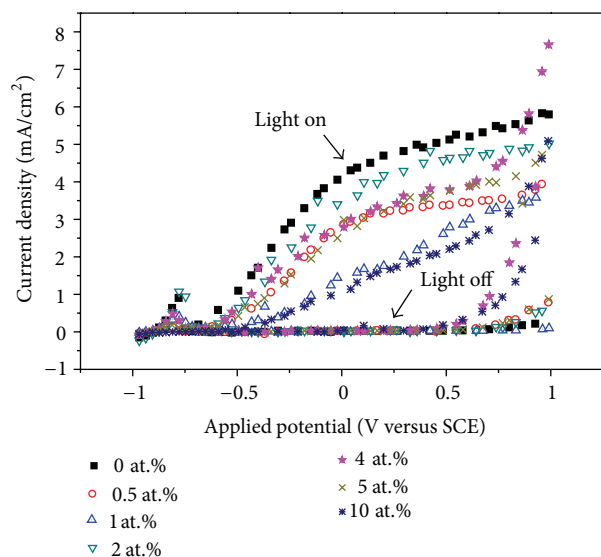


FIGURE 7: Photocurrent density versus applied potential for the unannealed Cu-doped CdS films with different doping levels recorded in 0.5 M Na_2SO_3 solution, illumination at an intensity of 165 mW/cm^2 .

illumination, then the local p-n junctions separated electrons and holes could not be further separated and recombined before they reached the substrate or the electrolyte side.

4. Conclusions

The present work demonstrated Cu-doped CdS films synthesized by ultrasonic spray pyrolysis with Cu^{2+} containing agent added into precursor directly. The morphology changed with Cu doping. The diameters of particles in the films decrease and then increase with increasing amount of Cu dopant. In this alteration of diameter changing direction, the (002) preferred orientation disappeared. The Cu doping causes a red shift of absorption edge from 517 nm to 650 nm, and the absorption strength increase with higher dopant concentration.

The unannealed films reveal n-type semiconducting behavior at dopant concentration lower than 2 at.% and both n-type and p-type characteristics at dopant concentration higher than 4 at.%. After annealing none of the doped films show n-type anymore. Only the annealing samples with more than 4 at.% Cu-doped films reveal p-type characteristic. Other samples reveal complex conducting characteristics.

The IPCE was improved by Cu doping for the unannealed samples. A maximum IPCE of 45% was got at 420 nm for the 5 at.% doped sample. But for the annealed samples, only that of 0.5 at.% and 1 at.% doped samples were slightly improved. IPCE of 2~10 at.% doped samples decreased dramatically. Under intensity illumination, the photocurrent of all the doped samples decreased. In the linear swept voltammetry measurement, charge separation efficiency in the space charge region was dependent on the illumination intensity. It decreased as the illumination intensity increased.

The p-type CdS can only be formed by high level doping (more than 4 at.%) and then annealing to make Cu element uniformly dispersible. But the doping caused a dramatically decrease of photocurrent. This p-type CdS deposition could not be thought to be advantageous, but as the unannealed Cu-doped samples give an increase in efficiency under weak illumination, which was ascribed to formation of disordered local p-n junction in the film, it can be said that this gives a new way easy to grasp to improve the separation of electron-hole pairs in the photoelectrochemical cells.

Acknowledgments

The authors gratefully acknowledge the financial supports from the National Natural Science Foundation of China (Contract no. 51121092, no. 51202186) and the National Basic Research Program of China (no. 2009CB220000). One of the authors (J. Su) was supported by the the Fundamental Research Funds for the Central Universities.

References

- [1] A. Mills and S. Le Hunte, "An overview of semiconductor photocatalysis," *Journal of Photochemistry and Photobiology A*, vol. 108, no. 1, pp. 1–35, 1997.
- [2] T. Bak, J. Nowotny, M. Rekas, and C. C. Sorrell, "Photoelectrochemical hydrogen generation from water using solar energy. Materials-related aspects," *International Journal of Hydrogen Energy*, vol. 27, no. 10, pp. 991–1022, 2002.
- [3] K. Rajeshwar, "Hydrogen generation at irradiated oxide semiconductor-solution interfaces," *Journal of Applied Electrochemistry*, vol. 37, no. 7, pp. 765–787, 2007.
- [4] T. Yoko, A. Yuasa, K. Kamiya, and S. Sakka, "Sol-gel-derived TiO_2 film semiconductor electrode for photocleavage of water. Preparation and effects of postheating treatment on the photoelectrochemical behavior," *Journal of the Electrochemical Society*, vol. 138, no. 8, pp. 2279–2285, 1991.
- [5] N. R. de Tacconi, C. R. Chenthamarakshan, G. Yogeewaran et al., "Nanoporous TiO_2 and WO_3 films by anodization of titanium and tungsten substrates: influence of process variables on morphology and photoelectrochemical response," *The Journal of Physical Chemistry B*, vol. 110, no. 50, pp. 25347–25355, 2006.
- [6] M. Guo, P. Diao, and S. Cai, "Hydrothermal growth of perpendicularly oriented ZnO nanorod array film and its photoelectrochemical properties," *Applied Surface Science*, vol. 249, no. 1–4, pp. 71–75, 2005.
- [7] S. Shen, J. Shi, P. Guo, and L. Guo, "Visible-light-driven photocatalytic water splitting on nanostructured semiconducting materials," *International Journal of Nanotechnology*, vol. 8, no. 6–7, pp. 523–591, 2011.
- [8] R. Asahi, T. Morikawa, T. Ohwaki, K. Aoki, and Y. Taga, "Visible-light photocatalysis in nitrogen-doped titanium oxides," *Science*, vol. 293, no. 5528, pp. 269–271, 2001.
- [9] T. Lindgren, J. M. Mwabora, E. Avandaño et al., "Photoelectrochemical and optical properties of nitrogen doped titanium dioxide films prepared by reactive DC magnetron sputtering," *The Journal of Physical Chemistry B*, vol. 107, no. 24, pp. 5709–5716, 2003.
- [10] A. Hameed, M. A. Gondal, and Z. H. Yamani, "Effect of transition metal doping on photocatalytic activity of WO_3 for

- water splitting under laser illumination: role of 3d-orbitals,” *Catalysis Communications*, vol. 5, no. 11, pp. 715–719, 2004.
- [11] G. Mandel, “Self-compensation limited conductivity in binary semiconductors. I. Theory,” *Physical Review*, vol. 13, no. 4, pp. A1073–A1079, 1964.
- [12] D. A. Cusano, “CdTe solar cells and photovoltaic heterojunctions in II-VI compounds,” *Solid State Electronics*, vol. 6, no. 3, pp. 217–218, 1963.
- [13] K. P. Varkey, K. P. Vijayakumar, T. Yoshida, and Y. Kashiwaba, “Spray pyrolysed thin film CdS homojunction solar cell with improved performance,” *Renewable Energy*, vol. 18, no. 4, pp. 465–472, 1999.
- [14] S. Mathew, P. S. Mukerjee, and K. P. Vijayakumar, “Characterization of spray pyrolysed CdS thin film doped with Cu,” *Japanese Journal of Applied Physics*, vol. 34, no. 9A, pp. 4940–4944, 1995.
- [15] H. Minoura, T. Sugiura, E. Suzuki, Y. Mizuno, Y. Ueno, and D. P. Amalnerkar, “Photoelectrochemical properties of polycrystalline films of CdS doped with Cu,” *Journal of the Electrochemical Society*, vol. 136, no. 5, pp. 1346–1350, 1989.
- [16] P. J. Sebastian, “P-type CdS thin films formed by in situ Cu doping in the chemical bath,” *Applied Physics Letters*, vol. 62, no. 23, pp. 2956–2958, 1993.
- [17] H. Xie, C. Tian, W. Li et al., “Preparation of p-type CdS thin films and in situ dark conductivity in vacuum deposited CdS : Cu films,” *Applied Surface Science*, vol. 257, no. 5, pp. 1623–1627, 2010.
- [18] S. M. Mahdavi, A. Irajizad, A. Azarian, and R. M. Tilaki, “Optical and structural properties of copper doped CdS thin films prepared by pulsed laser deposition,” *Scientia Iranica*, vol. 15, no. 3, pp. 360–365, 2008.
- [19] P. S. Patil, “Versatility of chemical spray pyrolysis technique,” *Materials Chemistry and Physics*, vol. 59, no. 3, pp. 185–198, 1999.
- [20] M. T. Li, J. Z. Su, and L. J. Guo, “Preparation and characterization of ZnIn₂S₄ thin films deposited by spray pyrolysis for hydrogen production,” *International Journal of Hydrogen Energy*, vol. 33, no. 12, pp. 2891–2896, 2008.
- [21] K. Nishidate, T. Sato, Y. Matsukura, M. Baba, M. Hasegawa, and T. Sasaki, “Density-functional electronic structure calculations for native defects and Cu impurities in CdS,” *Physical Review B*, vol. 74, no. 3, Article ID 035210, 8 pages, 2006.
- [22] M. F. Montemor, M. G. S. Ferreira, N. E. Hakiki, and M. da Cunha Belo, “Chemical composition and electronic structure of the oxide films formed on 316 L stainless steel and nickel based alloys in high temperature aqueous environments,” *Corrosion Science*, vol. 42, no. 9, pp. 1635–1650, 2000.
- [23] L. M. Peter and K. G. U. Wijayantha, “Electron transport and back reaction in dye sensitized nanocrystalline photovoltaic cells,” *Electrochimica Acta*, vol. 45, no. 28, pp. 4543–4551, 2000.

Research Article

TiO₂ and ZnO Nanoparticles in Photocatalytic and Hygienic Coatings

Veronika Jašková,^{1,2} Libuše Hochmannová,² and Jarmila Vytršová³

¹ University of Pardubice, Faculty of Chemical Technology, Institute of Chemistry and Technology of Macromolecular Materials, Studentská 573, 532 10 Pardubice, Czech Republic

² SYNPO, a.s., S. K. Neumanna 1316, 532 07 Pardubice, Czech Republic

³ University of Pardubice, Faculty of Chemical Technology, Department of Biological and Biochemical Sciences, Studentská 573, 532 10 Pardubice, Czech Republic

Correspondence should be addressed to Veronika Jašková; veronika.jaskova@centrum.cz

Received 30 November 2012; Revised 21 January 2013; Accepted 28 January 2013

Academic Editor: Elias Stathatos

Copyright © 2013 Veronika Jašková et al. This is an open access article distributed under the Creative Commons Attribution License, which permits unrestricted use, distribution, and reproduction in any medium, provided the original work is properly cited.

Antimicrobial paints were based on the aqueous acrylic dispersion and various nanoparticles of zinc oxide and titanium dioxide. Antimicrobial ability and photoactivity were assumed in these paints. It was possible to observe the photoactivity thanks to change of organic dyes due to oxidative-reductive reaction. The best photocatalytic effect showed the coating containing the mixture of the first type of TiO₂ and nano-ZnO despite the fact that the first type of TiO₂ was not better in the photocatalytic test than the other types of TiO₂. The agar dilution method was used to test antimicrobial ability. The *Escherichia coli*, *Pseudomonas aeruginosa*, and *Staphylococcus aureus* were chosen as test bacteria and *Penicillium chrysogenum* and *Aspergillus niger* as test molds. The antimicrobial effect of coatings with the mixture of the first type of TiO₂ and nano-ZnO was the best of all the tested samples.

1. Introduction

The worldwide spread of diseases is a great problem of modern society [1]. Infection is a major medical complication associated with health care environments [2]. Infection control is of utmost importance in various places, which require a high level of hygiene as technical applications for antimicrobial coatings include medical products, packaging materials, or filters used in air-conditioning systems. Hospitals, pharmaceutical production units, food factories, and so forth, need to be rigorously disinfected in order to destroy pathogenic microbes [3–5]. Microbial contamination of water poses a major threat to public health too. With the emergence of microorganisms resistant to multiple antimicrobial agents there is increased demand for improved disinfection methods [6]. A promising possibility to overcome these difficulties is the development of a concept to kill bacteria based on physical interactions. It has been proved that the chemicals with positively charged groups, such as quaternary ammonium or phosphonium, can kill bacteria upon

contact [3]. Also coatings containing photocatalytic TiO₂ can be interpreted as contact-active surfaces that kill approaching microbes by light-induced formation of hydroxyl radicals. The threat of device-related infection has become publicized due to recent global events involving MRSA or enterovirus. Unexpected multiplication of germs or other bacteria poses a serious health problem [7, 8].

Nanoparticles seem to be a very good option for antimicrobial additives mostly thanks to their size which is similar to the size of the cells and particles and can pass through the membrane easily. The main mechanism of toxicity of nanoparticles is thought to be via oxidative stress that damages lipids, carbohydrates, proteins, and DNA. Lipid peroxidation is considered the most dangerous as it leads to alterations in cell membrane properties which in turn disrupt vital cellular functions [9–12].

Fujishima and Honda found in 1972 [13] that the photocatalytic properties of certain materials have been used to convert solar energy into chemical energy to oxidize or reduce materials to obtain useful materials including hydrogen

TABLE 1: Characteristics of photocatalytic oxides.

Photocatalytic oxide	ZnO	TiO ₂ I	TiO ₂ II	TiO ₂ III
Appearance	Fine white powder	Fine white powder	Fine white powder	Fine white powder
Crystal form	Zincite	Anatase	Anatase	Anatase
Crystal size (nm)	30–40	550–600	40	10
Specific surface area, BET (m ² /g)	25–35	10	20–30	300
ZnO or TiO ₂ content (%)	99,5	98	97,5	99

and hydrocarbons and to remove pollutants and bacteria [14–16] on wall surfaces and in air and water.

Photocatalytic titanium dioxide (TiO₂) has been developed and extensively applied due to its nontoxicity, high catalytic activity, strong self-cleaning characteristics, and low cost. The photocatalytic process of TiO₂ or ZnO involves the generation of electron-hole pairs during exposure to light. These holes are able to react with nearby molecules to produce oxidants. The reaction of these particles with water produces the hydroxyl radical (OH[•]). In the case of oxygen, the result is the superoxide molecule (O₂^{•-}). Zinc oxide and other semiconductor materials may provide unusual electronic and chemical mechanisms for inhibiting the growth of microorganisms in a similar way to titanium dioxide [17, 18]. These radicals eventually attack bacteria or viruses in terms of inhibiting DNA clonal processing and destroy coenzymes, enzymes in the self-regeneration, and enzymes in the respiratory system. As a result, the radical stops the reproduction of bacteria and molds, thereby inhibiting bacteria growth or preventing virus DNA multiplication [19–21].

Waterborne coating systems are complex mixtures of polymers, pigments, fillers, and functional additives. The additives are used to improve different appearance or performance characteristics of the final coating. Unexpected synergies or reductions in performance may arise when certain components are included.

The ability of all of these additives to fulfill their roles is greatly impacted by the environment in which they operate. Antimicrobials are one class of additives that is very dependent on what else is in the system formulation [22].

2. Experimental

2.1. Preparation of the Hygienic Paints. Antimicrobial ability and photoactivity were assumed in these interior paints based on aqueous acrylic dispersion and different types of nano-titanium dioxide or nano-zinc oxide. These additives are commercially produced products. The characteristics of oxides are taken from datasheets of products, and they are listed in Table 1.

The first set of paints was formulated with different types of photocatalytic anatase titanium dioxide, and a combination of titanium dioxide and zinc oxide was used too. The content of nano-ZnO was 4 vol.%, and the amount of all different types of titanium dioxide was the same in all samples. The second series of antimicrobial paints was based only on nano-zinc oxide. The content of nano-ZnO was varied from 1 to 4 vol.%. Paint without nanooxides was formulated as control paint.

2.2. Evaluation of Photocatalytic Effect. The photoactivity of nanoparticles TiO₂ and ZnO is dependent on air humidity and ultraviolet (UV) radiation. It is possible to observe the photoactivity thanks to changes in organic dyes due to oxidative-reductive reaction. The interior paints were coated by brush thrice in Petri dishes (diameter 70 mm). These samples were dried for at least 1 week before photocatalytic testing. Then the solution of Orange II (15 g of 0.0014% by wt.) was poured on the surface of coating in the Petri dishes and covered by lids. A control coating without photocatalytic oxide was always tested too. Then, the samples were irradiated with UV lamps (11 fluorescent tubes with power of 11 W) emitting a wavelength of 300–400 nm for 120 min. The distance between the UV lamps and the samples was approximately 29 cm. Samples of Orange II solution were taken at definite time intervals. The absorbance of Orange II solution was measured by means of a photometer (SPEKOL 11, length of cuvette 1 cm) at the wavelength of 485 nm. The same procedure was used for the samples of coatings that were exposed to normal laboratory fluorescent tubes. The samples were irradiated for 72 hours.

2.3. Testing the Antimicrobial Efficiency of Coatings. The tests of antimicrobial efficiency were made on these coatings too. Acrylate coatings were applied in two layers on filter paper (sorte 391), size 5 × 5 cm, which were exposed to UV radiation (300–400 nm) before application for 30 minutes.

Testing microorganisms were *Escherichia coli* CCM 3954, *Staphylococcus aureus* CCM 4223, *Pseudomonas aeruginosa* CCM 3955, *Aspergillus niger* CCM 8189, and *Penicillium chrysogenum* CCM 8034 (Czech Collection of Microorganisms, Brno). Instruments and tested films were sterilized. Suspensions of cultures in solution of NaCl (0,9% by wt.) were prepared (density 10⁶ cells/mL, in fungi 10⁶ spores/mL). Density control of cells in the suspensions was carried out by culture of the suspension for each organism on an appropriate nutrient medium at optimum temperature. Fungi were cultured on agar MALT (HIMEDIA, India) at 24–25°C for 2–5 days and bacteria on nutrient agar no. 2 (HIMEDIA, India) at 37°C for 24–48 hours. The tested coatings, spread on filter paper (5 × 5 cm), were placed on Petri dishes with the appropriate cultivating medium and inoculated with the suspension of the testing microbe (0.1 mL). After incubation at optimum temperature for the optimum time for each microorganism, growths on the surface of the coatings were found out. Inhibition zones around the coatings were observed in some samples. The results are shown in Tables 2 and 3 and Figure 5.

TABLE 2: Amount of bacteria/mold growth (%) on the coatings with various types of TiO₂ or mixture of nano TiO₂ I and nano ZnO.

	<i>Escherichia coli</i>	<i>Staphylococcus aureus</i>	<i>Pseudomonas aeruginosa</i>	<i>Penicillium chrysogenum</i>	<i>Aspergillus niger</i>
Control	80	90	95	100	100
TiO ₂ I	0	0	80	80	80
TiO ₂ II	70	80	100	100	90
TiO₂ I + ZnO	0	0	80	30	0
TiO ₂ III	100	100	80	100	100

TABLE 3: Amount of bacteria/mold growth (%) on the coatings containing nano ZnO in various concentrations.

	<i>Escherichia coli</i>	<i>Staphylococcus aureus</i>	<i>Pseudomonas aeruginosa</i>	<i>Penicillium chrysogenum</i>	<i>Aspergillus niger</i>
Control	80	90	95	100	100
1% ZnO	0	0	80	100	90
2% ZnO	0	0	80	100	80
3% ZnO	0	0	40	95	15
4% ZnO	0	0	25	95	5

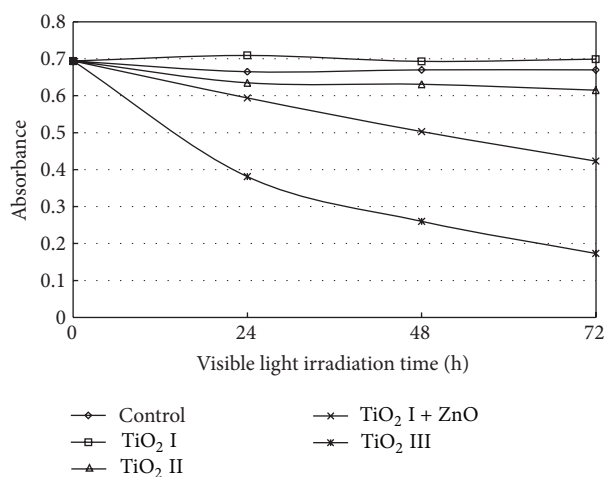


FIGURE 1: Absorbance of Orange II solution versus visible light irradiation time for various nanophotocatalytic oxides.

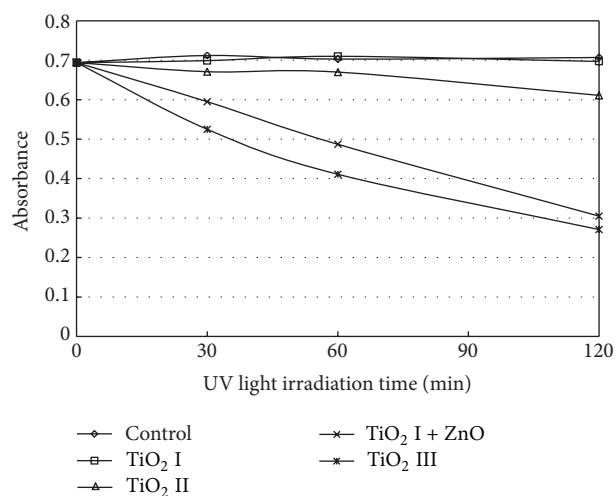


FIGURE 2: Absorbance of Orange II solution versus UV irradiation time for various nano photocatalytic oxides.

3. Results and Discussion

The photocatalytic activity was investigated for the coatings containing nano-ZnO, nano-TiO₂, mixture of these nanooxides, and coatings without nanooxides after exposure to UV radiation and VIS radiation. The absorbance changes in Orange II solution were measured, and the results are showed in Figures 1, 2, 3, and 4.

The paints based on aqueous acrylic dispersion doped by different nanooxides showed the photoactivity in case of the ultraviolet irradiation and also visible light irradiation. The control coating and coating containing TiO₂ I did not have any photocatalytic effect. The coating that included TiO₂ III showed the highest amount of photoactivity. There was a visible influence of nano-ZnO on the paint where the combination of nano-ZnO and TiO₂ I was used compared to coating containing only TiO₂ I.

Because of this result the photoactivity was also tested on the samples containing a various amount of nano-ZnO.

Photoactivity of samples after 24-hour irradiation of visible light changed quickly and then was nearly constant. The photoactivity of coatings after UV irradiation was relatively high but it was not as high as the photoactivity of nano-TiO₂ III. It was obvious that the photoactivity of coatings containing the mixture of TiO₂ I and nano-ZnO was higher than the photoactivity of coatings with 4 vol.% nano-ZnO. This synergic effect was observed in the case of UV radiation and also by exposure to visible light.

The antimicrobial efficacy of coatings containing nano-TiO₂, nano-ZnO and control coating without both nanoparticles is showed in Tables 2 and 3. It is obvious that coatings containing nano-TiO₂ showed poor antimicrobial efficacy compared to coatings with mixture of TiO₂ I and nano-ZnO and also compared to coatings with nano-ZnO. The antimicrobial effects of coatings with combination of TiO₂ I and nano-ZnO against bacteria *Escherichia coli* and *Staphylococcus aureus* and fungi *Aspergillus niger* were excellent.

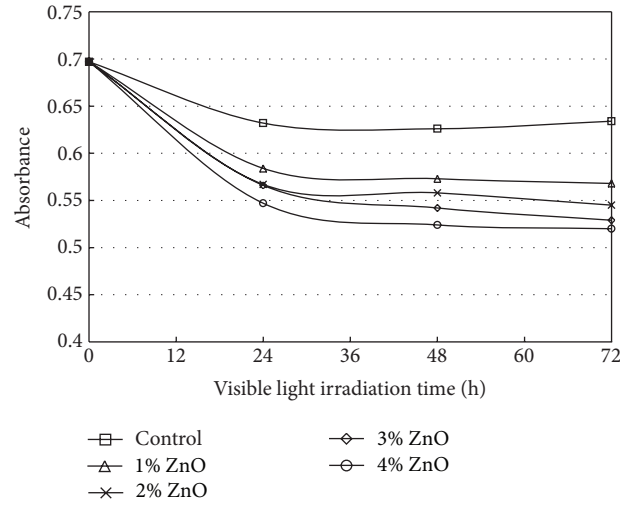


FIGURE 3: Absorbance of Orange II solution versus visible light irradiation time for various nano-ZnO pigment volume concentrations.

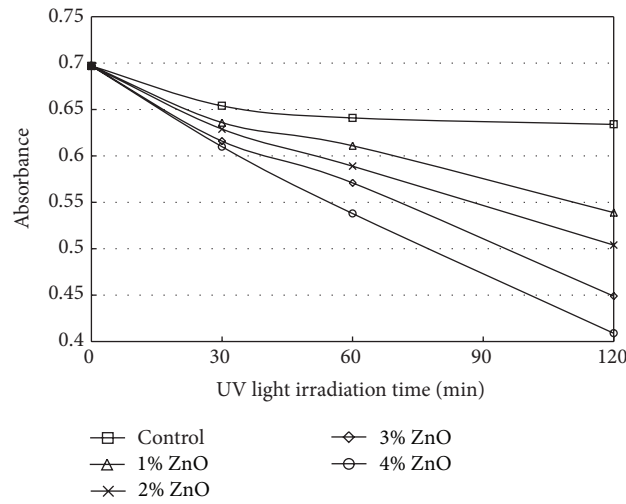


FIGURE 4: Absorbance of Orange II solution versus UV irradiation time for various nano-ZnO pigment volume concentrations.

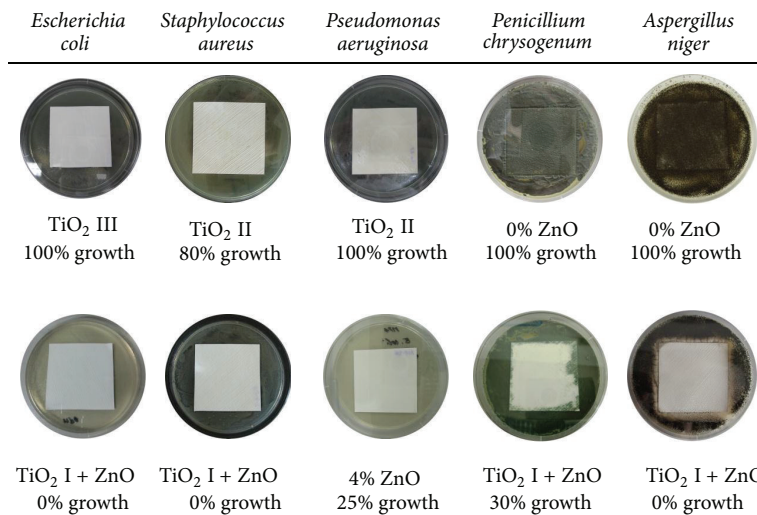


FIGURE 5: Photos of Petri dishes containing samples of coatings after growth of bacteria/mold.

The lowest concentration of nano-ZnO in the coating was effective against bacteria *Escherichia coli* and *Staphylococcus aureus*. Higher content of nano-ZnO improved inhibition against bacteria *Pseudomonas aeruginosa* and fungi *Aspergillus niger*. It could be caused by the toxic influence of nano-ZnO to the microbial cell. Nanosized particles can pass through the microbial cell, and they can damage organelles [12].

The effectiveness of the combination of TiO₂ I and nano-ZnO was somewhat better than that of the highest amount of nano-ZnO. Unfortunately the efficacy against *Pseudomonas aeruginosa* and *Penicillium chrysogenum* was poor in all cases. The better results were obtained for a combination of nanosized titanium dioxide and nanosized zinc oxide. This is probably caused by the influence of nanosized zinc oxide as written previously.

Very good antimicrobial effects of zinc oxide are consistent with the results published by Sawai and Kathirvelu [23, 24]. According to Chen et al., the antimicrobial activity of oxides depends on many factors such as humidity, temperature, UV light irradiation time, surface treatment, and morphology of nanoparticles [25]. In their work, Akiyama et al. using ZnO confirmed the inhibition of *S. aureus*. They found that 5% ZnO inhibited the growth of this bacterium [26].

Further experiments involving various concentrations of TiO₂ and ZnO nanoparticles or their mixtures to improve the antimicrobial efficacy could be tried. Maybe a mixture with organic biocides could show an interesting result.

4. Conclusion

The lowest concentration (1 vol.%) of nano-ZnO in the coating was effective against bacteria *Escherichia coli* and *Staphylococcus aureus*. Higher nano-ZnO content in coatings improved inhibition of bacteria *Pseudomonas aeruginosa* and fungi *Aspergillus niger*. However even the highest tested amount of ZnO was not sufficient to inhibit fungi *Penicillium chrysogenum*. The coatings containing a mixture of the first type of TiO₂ and nano-ZnO did not show the best photocatalytic effect, but the antimicrobial efficacy against *Escherichia coli*, *Staphylococcus aureus*, and *Aspergillus niger* was excellent.

Conflict of Interests

There was no conflict of interests present regarding the use of commercial products; all products used in this study were purchased from the market.

Acknowledgment

This study was financially supported by Ministry of Industry and Trade of the Czech Republic, Project no. FR-TI3/176.

References

- [1] J. C. Tiller, C. Sprich, and L. Hartmann, "Amphiphilic conetworks as regenerative controlled releasing antimicrobial coatings," *Journal of Controlled Release*, vol. 103, no. 2, pp. 355–367, 2005.
- [2] U. Makala and L. Wood, "Polyurethane biocidal polymeric surface modifiers," *Biomaterials*, vol. 27, pp. 1316–1326, 2006.
- [3] Y. Guan, H. Xiao, H. Sullivan, and A. Zheng, "Antimicrobial-modified sulfite pulps prepared by in situ copolymerization," *Carbohydrate Polymers*, vol. 69, no. 4, pp. 688–696, 2007.
- [4] J. Thome and A. Holländer, "Ultrathin antibacterial polyammonium coatings on polymer surfaces," *Surface and Coatings Technology*, vol. 174–175, pp. 584–587, 2003.
- [5] K. Barnes, J. Liang, R. Wu et al., "Synthesis and antimicrobial applications of 5,5'-ethylenebis[5-methyl-3-(3-triethoxysilylpropyl)hydantoin]," *Biomaterials*, vol. 27, no. 27, pp. 4825–4830, 2006.
- [6] J. P. Ruparelia, A. K. Chatterjee, S. P. Duttagupta, and S. Mukherji, "Strain specificity in antimicrobial activity of silver and copper nanoparticles," *Acta Biomaterialia*, vol. 4, no. 3, pp. 707–716, 2008.
- [7] C. J. Chung, C. C. Chiang, C. H. Chen et al., "Photocatalytic TiO₂ on copper alloy for antimicrobial purposes," *Applied Catalysis B*, vol. 85, no. 1–2, pp. 103–108, 2008.
- [8] C. J. Chung, H. I. Lin, and J. L. He, "Antimicrobial efficacy of photocatalytic TiO₂ coatings prepared by arc ion plating," *Surface and Coatings Technology*, vol. 202, no. 4–7, pp. 1302–1307, 2007.
- [9] M. Heinlaan and A. Ivask, "Toxicity of nanosized and bulk ZnO, CuO and TiO₂ to bacteria *Vibrio*," *Chemosphere*, vol. 71, pp. 1308–1316, 2008.
- [10] A. Kandelbauer and P. Widsten, "Antibacterial melamine resin surfaces for wood-based furniture and flooring," *Progress in Organic Coatings*, vol. 65, no. 3, pp. 305–313, 2009.
- [11] A. Travan, E. Marsich, I. Donati et al., "Silver-polysaccharide nanocomposite antimicrobial coatings for methacrylic thermosets," *Acta Biomaterialia*, vol. 7, no. 1, pp. 337–346, 2011.
- [12] M. N. Ragnail, M. Brown, D. Ye et al., "Internal benchmarking of a human blood-brain barrier cell model for screening of nanoparticle uptake and transcytosis," *European Journal of Pharmaceutics and Biopharmaceutics*, vol. 77, no. 3, pp. 360–367, 2011.
- [13] A. Fujishima and K. Honda, "Electrochemical photolysis of water at a semiconductor electrode," *Nature*, vol. 238, no. 5358, pp. 37–38, 1972.
- [14] L. Caballero, K. A. Whitehead, N. S. Allen, and J. Verran, "Inactivation of *Escherichia coli* on immobilized TiO₂ using fluorescent light," *Journal of Photochemistry and Photobiology A*, vol. 202, no. 2–3, pp. 92–98, 2009.
- [15] T. Matsunaga, R. Tomoda, T. Nakajima, and H. Wake, "Photoelectrochemical sterilization of microbial cells by semiconductor powders," *FEMS Microbiology Letters*, vol. 29, no. 1–2, pp. 211–214, 1985.
- [16] K. Nakata and A. Fujishima, "TiO₂ photocatalysis: design and applications," *Journal of Photochemistry and Photobiology C*, vol. 13, pp. 169–189, 2012.
- [17] S. D. Gittard, J. R. Perfect, N. A. Monteiro-Riviere, W. Wei, C. Jin, and R. J. Narayan, "Assessing the antimicrobial activity of zinc oxide thin films using disk diffusion and biofilm reactor," *Applied Surface Science*, vol. 255, no. 11, pp. 5806–5811, 2009.
- [18] L. Hochmannova and J. Vytrasova, "Photocatalytic and antimicrobial effects of interior paints," *Progress in Organic Coatings*, vol. 67, no. 1, pp. 1–5, 2010.
- [19] C. J. Chung, C. C. Chiang, C. H. Chen et al., "Photocatalytic TiO₂ on copper alloy for antimicrobial purposes," *Applied Catalysis B*, vol. 85, no. 1–2, pp. 103–108, 2008.

- [20] C. J. Chung, H. I. Lin, and J. L. He, "Antimicrobial efficacy of photocatalytic TiO₂ coatings prepared by arc ion plating," *Surface and Coatings Technology*, vol. 202, no. 4–7, pp. 1302–1307, 2007.
- [21] M. Heinlaan, A. Ivask, I. Blinova, H. C. Dubourguier, and A. Kahru, "Toxicity of nanosized and bulk ZnO, CuO and TiO₂ to bacteria *Vibrio fischeri* and crustaceans *Daphnia magna* and *Thamnocephalus platyurus*," *Chemosphere*, vol. 71, no. 7, pp. 1308–1316, 2008.
- [22] A. M. Rhoades, D. A. Wicks, B. Miriyala, and J. Williamson, "Interactions of an antimicrobial peptide (Ac-RRWWRF-NH₂) and surfactants: towards antimicrobial peptide additives for coatings applications," *Progress in Organic Coatings*, vol. 58, no. 2-3, pp. 209–216, 2007.
- [23] J. Sawai, E. Kawada, F. Kanou et al., "Detection of active oxygen generated from ceramic powders having antibacterial activity," *Journal of Chemical Engineering of Japan*, vol. 29, no. 4, pp. 627–633, 1996.
- [24] S. Kathirvelu, L. D'Souza, and B. Dhurai, "A study on functional finishing of cotton fabrics using nanoparticles of zinc oxide," *Materials Science*, vol. 15, no. 1, pp. 75–79, 2009.
- [25] F. Chen, X. Yang, and Q. Wu, "Antifungal capability of TiO₂ coated film on moist wood," *Building and Environment*, vol. 44, no. 5, pp. 1088–1093, 2009.
- [26] H. Akiyama, O. Yamasaki, H. Kanzaki, J. Tada, and J. Arata, "Effects of zinc oxide on the attachment of *Staphylococcus aureus* strains," *Journal of Dermatological Science*, vol. 17, no. 1, pp. 67–74, 1998.

Research Article

Effect of PdS on Photocatalytic Hydrogen Evolution of Nanostructured CdS under Visible Light Irradiation

Qingyun Chen, Cheng Suo, Shu Zhang, and Yunhai Wang

State Key Laboratory of Multiphase Flow in Power Engineering, School of Energy and Power Engineering, Xi'an Jiaotong University, Xi'an 710049, China

Correspondence should be addressed to Qingyun Chen; qychen@mail.xjtu.edu.cn

Received 12 December 2012; Accepted 12 January 2013

Academic Editor: Elias Stathatos

Copyright © 2013 Qingyun Chen et al. This is an open access article distributed under the Creative Commons Attribution License, which permits unrestricted use, distribution, and reproduction in any medium, provided the original work is properly cited.

To investigate the effect of PdS as a cocatalyst for photocatalytic hydrogen evolution, nanostructured PdS/CdS were prepared by an in situ coprecipitation and hydrothermal method, respectively. The as-prepared photocatalysts were characterized by transmission electron microscopy (TEM), X-ray diffraction (XRD), UV-visible absorption spectra, and photoluminescence spectra (PL). With PdS highly dispersed in the CdS nanostructures, the photoactivity was evaluated by hydrogen evolution from aqueous solution containing Na₂S/Na₂SO₃ as sacrificial reagents under visible light irradiation. When the concentration of PdS was 1% by weight, PdS/CdS, prepared by the in situ coprecipitation, showed the highest photocatalytic activity, while that prepared by hydrothermal method showed the most stability for hydrogen evolution. The effect of highly dispersed PdS on the photoactivity was discussed.

1. Introduction

Hydrogen, as a kind of renewable energy, has attracted more and more attention due to the depletion of fossil fuels and the pollution caused by continuously increasing energy demands [1–3]. Photocatalytic water-splitting hydrogen evolution using semiconducting photocatalysts is one of the most ideal ways to make full use of solar energy to produce hydrogen [4]. Up to now, a lot of semiconducting photocatalysts have been reported to produce hydrogen, such as TiO₂ [5], CdS [6], and ZnS [7]. Among them, CdS has been widely studied because of its excellent light absorption property in the visible region [8].

CdS alone demonstrates low photoactivity and bad stability for hydrogen evolution under visible light because, in its photocatalytic process, the phenomenon of photocorrosion is prone to occur [9]. Many efforts have been made to overcome the problem of photocorrosion, such as photosensitizing CdS with photosensitizers [4, 10], combining CdS with another semiconductor [11], and exploiting alternative preparation approaches to control the size and shape of CdS [12].

Loading a cocatalyst onto CdS is also a good method to improve its photoactivity and stability. A suitable cocatalyst cannot only promote the separation of photoexcited electrons and holes and suppress their recombination, but also decrease the activation potentials for H₂ evolution [13]. Transition metals and their oxides (sulfides) have been widely used as cocatalysts including Pd [14–16], Pt [17, 18], NiO [19], RuO₂ [20], and MoS₂ [21]. Therefore, it is highly desirable to find suitable cocatalysts to improve the photoactivity and stability of CdS. Recently, Yan et al. reported that CdS loaded with Pt-PdS bicomponent cocatalyst achieved the highest quantum yield of about 93% in the presence of sacrificial reagents under visible light irradiation [22]. Therefore, it would be of great interest to investigate the effect of the cocatalyst on the photocatalytic performance of CdS.

In this paper, nanostructured PdS/CdS photocatalysts were synthesized by in situ coprecipitation and hydrothermal method, respectively. The effect of PdS on the photoactivity and stability of CdS was investigated for hydrogen evolution under visible light from water containing Na₂S and Na₂SO₃ as sacrificial reagents.

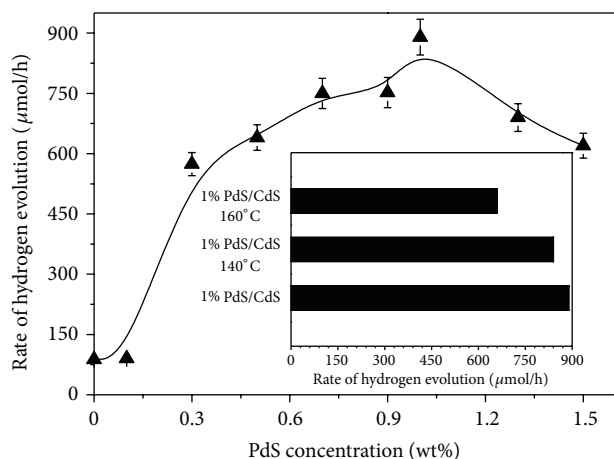


FIGURE 1: Rate of hydrogen evolution on PdS/CdS samples loaded with different amounts of PdS under visible light; (insert) rate of hydrogen evolution on PdS/CdS samples loaded with 1 wt% amount of PdS prepared by different hydrothermal temperatures and in situ coprecipitation.

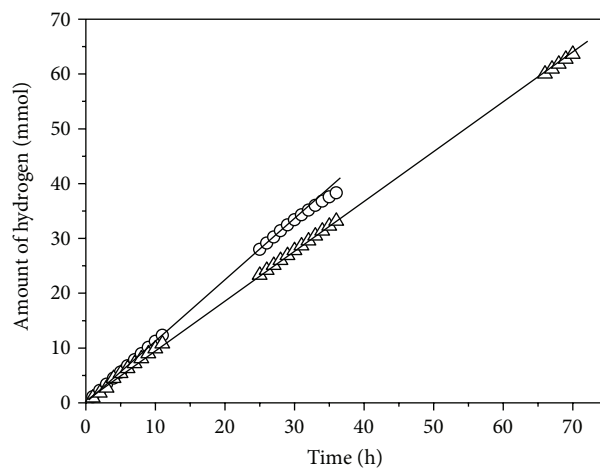
2. Experiments

2.1. Synthesis of PdS/CdS. All of the chemicals were of analytical grade and used without further purification. Deionized water was used in the sample synthesis.

The nanostructured CdS particles were synthesized as follows: an aqueous solution of 0.14 M Na_2S was added slowly to 0.14 M $\text{Cd}(\text{OAc})_2$ solution under vigorous stirring at room temperature. The yellow mixture was stirred for 12 h and kept for additional 12 h. The resulting yellow solid was collected by filtration and washed with deionized water several times. The wet solid was suspended in deionized water and transferred into a 100 mL stainless Teflon-lined autoclave. The autoclave was sealed and heated at 200°C for 24 h and then cooled down to room temperature naturally. The yellow solid was filtered and washed with water and ethanol subsequently, followed by drying at 80°C for 24 h.

The loading of PdS on CdS producing PdS/CdS was realized by the following two methods. For the in situ coprecipitation, a PdCl_2 aqueous solution was added dropwise under stirring at room temperature to a suspension of CdS nanoparticles (0.2 g, as prepared above) dispersed in Na_2S aqueous solution just before the photocatalytic reaction. For the hydrothermal method, the mixture obtained by the in situ coprecipitation was stirred for 12 h. The resulting precipitates were centrifuged and washed with deionized water several times. The precipitates were suspended in deionized water, transferred into a 100 mL stainless Teflon-lined autoclave, and heated at a certain temperature for 6 h.

2.2. Characterization. The X-ray diffraction (XRD) patterns of catalysts were obtained from a Panalytical X'pert Pro X-ray diffractometer equipped with $\text{Cu K}\alpha$ irradiation with the scanning step of $0.05^\circ/\text{s}$; the operation voltage and current were 45 kV and 40 mA, respectively. UV-visible absorption spectra were measured by a HITACHI UV4100 instrument,



○ 1% PdS/CdS in situ
△ 1% PdS/CdS 140°C

FIGURE 2: Time courses of hydrogen evolution on PdS/CdS samples loaded with 1 wt% PdS prepared by different methods.

with the scanning range from 300 to 800 nm. The photoluminescence spectra (PL) were measured at room temperature using a PTI QM-4 fluorescence spectrophotometer. The crystallite morphologic micrograph was observed on a high resolution transmission electron microscopy (HRTEM) JEOL JEM-3010 instrument and a field emission scanning electron microscopy (SEM) JSM-6700F (Japan).

2.3. Evaluation of Photocatalytic Activity. Photocatalytic reaction was carried out in a side-irradiation Pyrex cell. The effective irradiation area for the cell is 12.56 cm^2 . The powder of photocatalyst (0.2 g) was dispersed by a magnetic stirrer in an aqueous solution (200 mL) consisting of Na_2S (0.5 M) and Na_2SO_3 (0.5 M) as electron donors in the cell. The photocatalysts were irradiated with visible light through a cutoff filter ($\lambda > 430\text{ nm}$, $T = 65\%$) from a 300 W Xe lamp. The amount of H_2 gas was determined by an online thermal conductivity detector (TCD) gas chromatograph (NaX zeolite column, nitrogen as a carrier gas).

3. Results and Discussion

Figure 1 shows the rate of hydrogen evolution on PdS/CdS photocatalysts loaded with different amounts of PdS prepared by the in situ coprecipitation under visible light, together with those prepared by the hydrothermal method (insert in Figure 1). As the amount of PdS increases from 0 to 1%, the hydrogen evolution rate on PdS/CdS increases markedly from $\sim 88.1\ \mu\text{mol/h}$ to $\sim 890.3\ \mu\text{mol/h}$, about 10 times higher. However, when the amount of PdS increases to 1.3%, the photocatalytic activity decreases slightly. The surplus PdS can work as an optical filter to shield incident light and hence suppress further enhancement of photocatalytic activity for hydrogen evolution. For comparing, the insert in Figure 1 shows the rate of hydrogen evolution on the PdS/CdS photocatalyst loaded with 1 wt% PdS prepared by hydrothermal

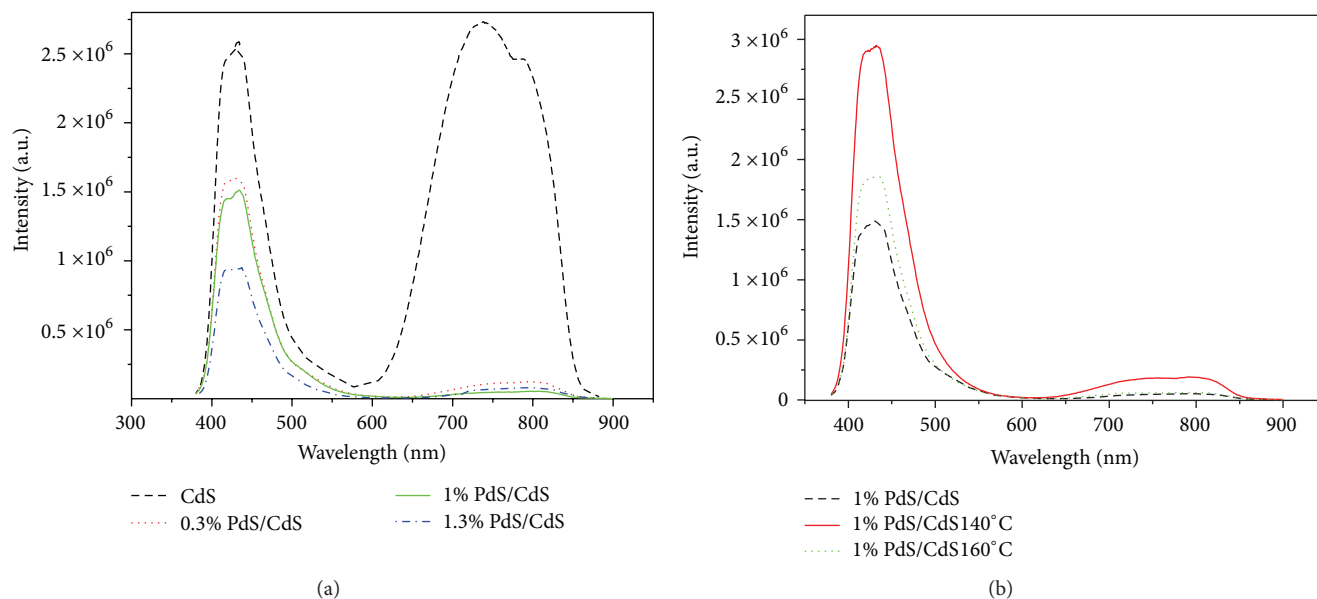


FIGURE 3: (a) Photoluminescence spectra of PdS/CdS samples loaded with different amounts of PdS. (b) Photoluminescence spectra of PdS/CdS samples loaded with 1 wt% PdS prepared by different methods.

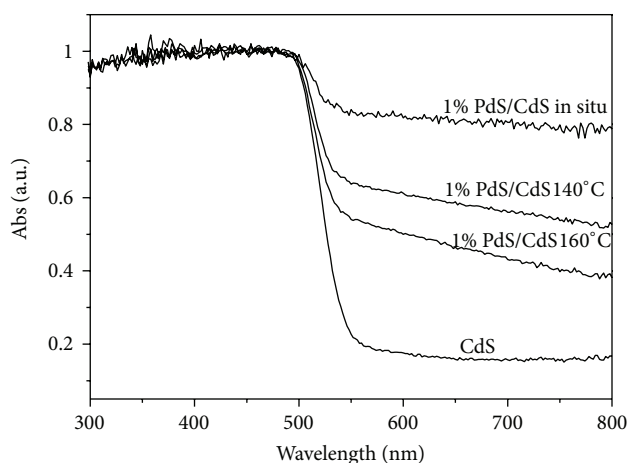


FIGURE 4: UV-visible absorption spectra of CdS and PdS/CdS samples.

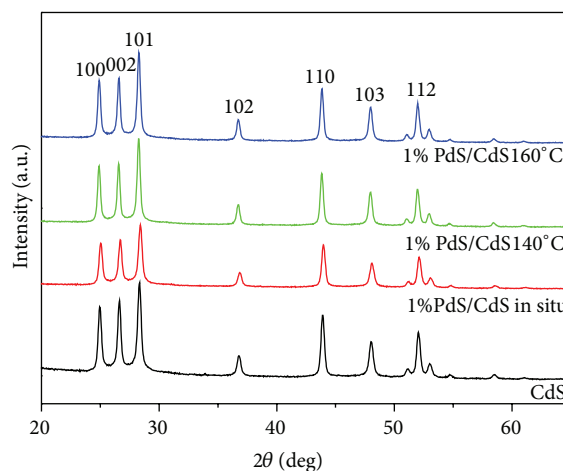


FIGURE 5: XRD patterns of PdS/CdS samples.

method. It appears that the photocatalytic activity also decreases slightly. But the photocatalytic stability improves, as shown in Figure 2 which shows the hydrogen evolution on PdS/CdS photocatalysts loaded with 1% PdS prepared by different methods as long as $\text{Na}_2\text{S}/\text{Na}_2\text{SO}_3$ is present. PdS/CdS photocatalysts prepared by the in situ coprecipitation can act stably for less than 40 hours. It is noted that PdS/CdS photocatalysts prepared by hydrothermal method can exhibit significantly improved stability, showing steady hydrogen production more than 70 hours. The observation suggests that the dispersion of PdS in nanostructured CdS can improve the photoactivity, but the stable photocatalytic activity for hydrogen evolution can be influenced by the synthesis method.

To analyze the reason, Figure 3 shows the photoluminescence spectra of PdS/CdS photocatalysts. The photoluminescence spectroscopy can give information about the photoexcited energy/electron transfer and recombination process, and it has been widely used to investigate the photophysical and photochemical properties of photocatalysts [23]. As shown in Figure 3(a), the pure CdS exhibits broad fluorescence peak related to Stoke's shifts ~ 435 nm and ~ 750 nm [4]. The band at ~ 432 nm is due to intrinsic emission, whereas that at 750 nm originates from transition of electrons trapped at surface state to the valance band of CdS. This fact suggests that nanostructured CdS has defects. By loading PdS, the fluorescence intensities are quenched, which reveals that the recombination of photoelectrons and holes is efficiently suppressed resulting in the improved photoactivity.

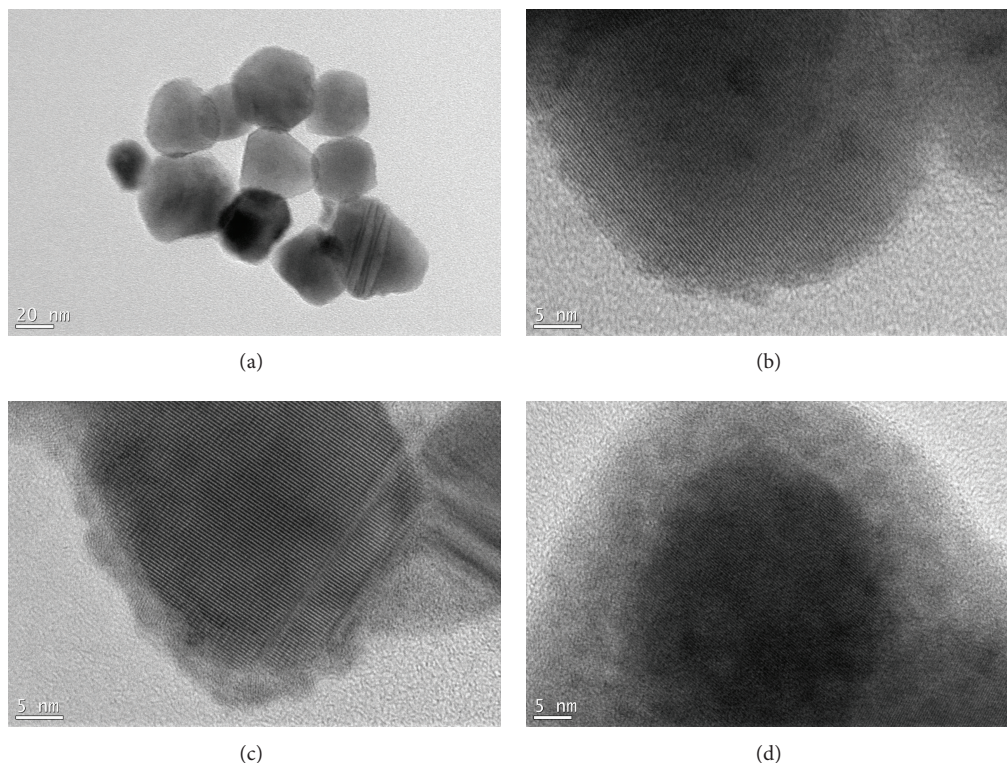


FIGURE 6: TEM image of (a and b) CdS, (c) PdS/CdS prepared by in situ coprecipitation, and (d) PdS/CdS prepared by hydrothermal method at 160°C.

However, the fluorescence intensities of PdS/CdS prepared by hydrothermal method are slightly enhanced as shown in Figure 3(b). This fact might be beneficial for the stability of photocatalysts. Then it can be concluded that the weaker the fluorescence intensity of the photocatalyst is, the higher the photoactivity is.

The UV-visible absorption spectra for PdS/CdS are shown in Figure 4. The pure CdS has an absorption edged at about 550 nm, with energy gap estimated to be 2.3 eV. The spectra of PdS/CdS show an enhanced absorption in visible light region. Such an enhancement can be assigned to the existence of PdS phase. It was reported that PdS could not absorb visible light [4]. Therefore, the fact suggests that the PdS phase can enhance the absorption of CdS phase. From Figure 4, it can be seen that the enhancement of the absorption in visible light region is different which is dependent on the preparation condition. It suggests that the higher the visible adsorption is, the higher the photoactivity is.

The XRD patterns of various samples displayed in Figure 5 can be readily indexed as the (100), (002), (101), (110), (103), and (112) planes of the hexagonal phase of the wurtzite CdS structure, which are well matched with the standard values (JCPDS Card No. 02-0549) according to the main diffraction peaks at 24.9°, 26.6°, 28.4°, 43.7°, 48.1°, and 52.0°. It is worth noting that there are no characteristic peaks associated with PdS in these XRD patterns, which may be

due to the low concentration of PdS and its relatively low crystallinity for the PdS/CdS samples prepared by the in situ coprecipitation and due to the high dispersion of PdS particles in the nanostructured CdS and the low concentration of PdS for the PdS/CdS samples prepared by hydrothermal method. By the way the diffraction peak would not shift when Pd²⁺ was doped into the lattice of CdS, considering that an ionic radius of Pd²⁺ (0.88 Å) is lower than that of Cd²⁺ (0.97 Å). The fact indicates that no significant lattice deformation occurred with different treatments of PdS/CdS samples.

Morphology of the as-prepared photocatalysts is shown in Figure 6. From Figure 6(a), it can be seen that the nanostructured CdS is mainly composed of nanospheres. As shown in Figure 6(b), for the higher magnification of CdS, these nanospheres are well crystallized. When PdS is loaded, there appears spherical nanoparticles on the surface of CdS which disperse more uniformly by comparing Figures 6(b) and 6(c). PdS by itself displays no photoactivity for H₂ production, but PdS can act as a cocatalyst together with CdS. Then it suggests that PdS exists on the surface of CdS which can enhance the photoactivity of CdS. However, there appears a nanoparticle layer for PdS/CdS prepared by hydrothermal method as shown in Figure 6(d). This indicates that the loading of PdS can improve the photoactivity of CdS, but the nanoparticle layer may decrease the

photoactivity in spite of the increase in the stability of CdS.

4. Conclusion

Nanostructured PdS/CdS photocatalysts were synthesized by an in situ coprecipitation and a hydrothermal method, respectively. With a concentration of PdS approximately 1.0%, PdS/CdS photocatalysts synthesized by the in situ coprecipitation displayed the highest photocatalytic activity for hydrogen evolution under visible light irradiation from an aqueous solution containing sulfide and sulfite. However, PdS/CdS photocatalysts synthesized by the hydrothermal method showed the highest stability for hydrogen evolution. This study indicates that it is an effective method for preparing a stable, efficient photocatalyst by using a suitable cocatalyst.

Acknowledgments

This work was financially supported by the National Basic Research Program of China (2009CB220000), Research Fund for the Doctoral Program of Higher Education of China (20110201120042), and Natural Science Foundation of China (21206133).

References

- [1] X. B. Chen, S. H. Shen, L. J. Guo, and S. S. Mao, "Semiconductor-based photocatalytic hydrogen generation," *Chemical Reviews*, vol. 11, pp. 6503–6570, 2010.
- [2] C. L. Li, J. Yuan, B. Y. Han, and W. F. Shangguan, "Synthesis and photochemical performance of morphology-controlled CdS photocatalysts for hydrogen evolution under visible light," *International Journal of Hydrogen Energy*, vol. 36, no. 7, pp. 4271–4279, 2011.
- [3] S. H. Shen, P. H. Guo, J. W. Shi, and L. J. Guo, "Visible-light-driven photocatalytic water splitting on nanostructured semiconducting materials," *International Journal of Nanotechnology*, vol. 8, no. 6-7, pp. 523–591, 2011.
- [4] S. Zhang, Q. Y. Chen, D. W. Jing, Y. H. Wang, and L. J. Guo, "Visible photoactivity and antiphotocorrosion performance of PdS-CdS photocatalysts modified by polyaniline," *International Journal of Hydrogen Energy*, vol. 37, pp. 791–796, 2012.
- [5] A. Fujishima and K. Honda, "Electrochemical photolysis of water at a semiconductor electrode," *Nature*, vol. 238, no. 5358, pp. 37–38, 1972.
- [6] E. Borgarello, N. Serpone, E. Pelizzetti, and M. Barbeni, "Efficient photochemical conversion of aqueous sulphides and sulphites to hydrogen using a rhodium-loaded CdS photocatalyst," *Journal of Photochemistry*, vol. 33, no. 1, pp. 35–48, 1986.
- [7] I. Tsuji and A. Kudo, "H₂ evolution from aqueous sulfite under visible-light irradiation over Pb and halogen-codoped ZnS photocatalysts," *Journal of Photochemistry and Photobiology A*, vol. 156, no. 1–3, pp. 249–252, 2003.
- [8] M. Matsumura, S. Furukawa, Y. Saho, and H. Tsubomura, "Cadmium sulfide photocatalyzed hydrogen production from aqueous solutions of sulfite: effect of crystal structure and preparation method of the catalyst," *Journal of Physical Chemistry*, vol. 89, no. 8, pp. 1327–1329, 1985.
- [9] K. G. Kanade, B. Jin-OoK, D. P. Amalnerkar, and B. B. Kale, "Nano-CdS by polymer-inorganic solid-state reaction: visible light pristine photocatalyst for hydrogen generation," *Materials Research Bulletin*, vol. 41, no. 12, pp. 2219–2225, 2006.
- [10] H. Zhang and Y. F. Zhu, "Significant visible photoactivity and antiphotocorrosion performance of CdS photocatalysts after monolayer polyaniline hybridization," *Journal of Physical Chemistry C*, vol. 114, no. 13, pp. 5822–5826, 2010.
- [11] J. S. Jang, S. M. Ji, S. W. Bae, H. C. Son, and J. S. Lee, "Optimization of CdS/TiO₂ nano-bulk composite photocatalysts for hydrogen production from Na₂S/Na₂SO₃ aqueous electrolyte solution under visible light ($\lambda \geq 420$ nm)," *Journal of Photochemistry and Photobiology A*, vol. 188, no. 1, pp. 112–119, 2007.
- [12] A. Eychmuller, "Structure and photophysics of semiconductor nanocrystals," *The Journal of Physical Chemistry B*, vol. 104, pp. 6514–6528, 2000.
- [13] J. S. Jang, D. J. Ham, N. Lakshminarasimhan, W. Y. Choi, and J. S. Lee, "Role of platinum-like tungsten carbide as cocatalyst of CdS photocatalyst for hydrogen production under visible light irradiation," *Applied Catalysis A*, vol. 346, no. 1-2, pp. 149–154, 2008.
- [14] I. B. Rufus, V. Ramakrishnan, B. Viswanathan, and J. C. Kuriacose, "Photoelectrochemical and photocatalytic studies on Pd/CdS," *Indian Journal of Technology*, vol. 27, pp. 171–173, 1989.
- [15] J. B. Zhong, Y. Lu, W. D. Jiang et al., "Characterization and photocatalytic property of Pd/TiO₂ with the oxidation of gaseous benzene," *Journal of Hazardous Materials*, vol. 168, no. 2-3, pp. 1632–1635, 2009.
- [16] A. Khalil, M. A. Gondal, and M. A. Dastageer, "Augmented photocatalytic activity of palladium incorporated ZnO nanoparticles in the disinfection of Escherichia coli microorganism from water," *Applied Catalysis A*, vol. 402, no. 1-2, pp. 162–167, 2011.
- [17] B. Neppolian, A. Bruno, C. L. Bianchi, and M. Ashokkumar, "Graphene oxide based Pt-TiO₂ photocatalyst: ultrasound assisted synthesis, characterization and catalytic efficiency," *Ultrasonics Sonochemistry*, vol. 19, pp. 9–15, 2011.
- [18] N. Sahu, S. N. Upadhyay, and A. S. K. Sinha, "Kinetics of reduction of water to hydrogen by visible light on alumina supported Pt-CdS photocatalysts," *International Journal of Hydrogen Energy*, vol. 34, no. 1, pp. 130–137, 2009.
- [19] J. G. Yu, W. G. Wang, and B. Cheng, "Synthesis and enhanced photocatalytic activity of a hierarchical porous flowerlike p-n junction NiO/TiO₂ photocatalyst," *Chemistry*, vol. 5, no. 12, pp. 2499–2506, 2010.
- [20] A. A. Ismail, L. Robben, and D. W. Bahnemann, "Study of the efficiency of UV and visible-light photocatalytic oxidation of methanol on mesoporous RuO₂-TiO₂ nanocomposites," *ChemPhysChem*, vol. 12, no. 5, pp. 982–991, 2011.
- [21] X. Zong, H. J. Yan, G. P. Wu et al., "Enhancement of photocatalytic H₂ evolution on CdS by loading MoS₂ as cocatalyst under visible light irradiation," *Journal of the American Chemical Society*, vol. 130, no. 23, pp. 7176–7177, 2008.
- [22] H. J. Yan, J. H. Yang, G. J. Ma et al., "Visible-light-driven hydrogen production with extremely high quantum efficiency on Pt-PdS/CdS photocatalyst," *Journal of Catalysis*, vol. 266, no. 2, pp. 165–168, 2009.
- [23] H. P. Liu, K. Zhang, D. W. Jing, G. J. Liu, and L. J. Guo, "SrS/CdS composite powder as a novel photocatalyst for hydrogen production under visible light irradiation," *International Journal of Hydrogen Energy*, vol. 35, no. 13, pp. 7080–7086, 2010.